Recombination and spin dynamics of excitons in indirect (In,Al)As/AlAs quantum dots

Dissertation

presented to the Faculty of Physics of the
TU Dortmund University, Germany,
in partial fulfillment of the requirements
for the degree of

Doktor rer. nat.

by
Daniel Dunker

technische universität
dortmund

Dortmund, September 2013

Examination board:
Prof. Dr. Dmitri R. Yakovlev
Prof. Dr. Heinz Hövel
Prof. Dr. Götz S. Uhrig
Dr. Bärbel Siegmann

Contents

Motivation

Since the very beginning of human culture, humanity has used solid states in various forms starting thousands of years ago by the production and application of bronze or by the use of silicate holding earth to build stable buildings. Over the centuries the techniques for the production of pure elements and alloys have been improved drastically, enabling further advanced applications. The discovery of electricity and the postulation of its origin by the transport of elementary charges led in the midst of the 18^{th} century among other things to the formulation of the Maxwell´s equations [1]. Metals with their low electrical resistivity were primary subject of fundamental research during that time. In contrast to metals, the interest in structures with moderate electrical resistivity was low at that time, as their features and advantages were less apparent. An alternative character for the separation between metal (conductor), insulator, and semiconductor, the band gap, described in chapter 1.1, was formulated much later with the emergence of quantum mechanics. With the invention of the first field-effect transistor by J. E. Lilienfeld in 1925 [2] and its later advent in the late 1940^{th}, semiconductor materials firstly became the center of scientific research, while the production of highly pure elementary semiconductors like germanium and silicon still posed a great challenge at that time.
With an increased number of applications for semiconductors structures, the requirements for these material additionally expanded. The fixed band gap energies for elementary semiconductor crystals did no longer fulfil these, so that new materials like binary compound semiconductors were spotlighted. These could at least partially fill the breaks between the fixed band gaps of the elementary semiconductors. After intensive scientific work on these bulk semiconductors during the 20^{th} century and technical advances in the construction of artificial crystals, researchers began to explore possibilities to further manipulate the materials of interest. With the observation and description of superlattices by Esaki and Tsu in the 1970^{th} [3], the focus in scientific research was changed towards the development of nanostructures. First realizations were made by growing crystal structures with alternating material compositions. With layer thicknesses smaller than the free electron wavelength, new electronic features could be observed which had not been present in their bulk material counterparts. Essential changes in the electronic properties caused by the reduction of the dimensionality are described in chapter 1.2. These changed properties manifested in the lower-dimensional semiconductor by the evolution of new effects. Examples for these effects are step-like

absorption and gain based on the changed density of states [4], exciton cyclotron resonances [5] and the electric field induced Stark effect [6].
The success in the research on these structures of reduced symmetry inspired scientists to investigate possibilities to further reduce the structure dimensionalities. As a result of this research, quantum wires (one dimensional) and quantum dots (zero dimensional) were fabricated. The first structure for fundamental research of transport phenomena, and the second as artificial atoms with predictable and assignable characteristics such as the band gap energy, which can be tailored to conform many requirements. The quantum dots offered here the possibility to tailor the band gap energies very precisely, not only by a change of their material composition, but also by the control of the confinement potential influencing the band gaps. In the last decades quantum dots were ascribed an increased attention for their possible application in the field of quantum information processing and information storage on a quantum state basis. Here, especially the electronic spin states ($\uparrow/\downarrow$) are of interest as they pose a unit similar to the classical bit with its values of 0 and 1, but following the quantum mechanics.
Although the effects of electron spin states have been observed already in 1897 in measurements of the splitting of the sodium emission lines in presence of external magnetic fields by P. Zeeman [7], an exact explanation for this effect was not achieved. Almost 30 years later in 1926, the origin of the Zeeman effect was finally attributed to the electronic spin state [8]. Applications using this new electron characteristics have not been seriously considered since the 1950$^{\text{th}}$ with the development of modern computers. In expansion to classical computers, modern concepts predicted additionally the possibility to perform calculations with the help of quantum states, requiring a new definition for the classical smallest information unit. A quantum mechanical bit, the so-called qubit, is in contrast to the classical system a linear combination of a two-level system, like the electron spin $\pm 1/2$ system leading to $|\Psi\rangle = c_0|\uparrow\rangle + c_1|\downarrow\rangle$ [9]. Quantum dots have here the advantage of a fast initialization (hundreds of picoseconds by optical means) and their ability to preserve their electronic spin states for longer times compared to bulk materials. Furthermore, the quantum dots as a confining system for the spin states are typically well protected by a surrounding matrix of different material.
In this thesis one of these zero-dimensional structures will be investigated. The QD material at hand is indium arsenide (InAs), a well-known and often used direct semiconductor alloy. The zero-dimensional structure was grown by molecular beam epitaxy surrounded by the indirect semiconductor aluminium arsenide (AlAs), which serves as a matrix for the QD. Aim of this construction is the combination of advantages of indirect semiconductors, described in chapter 1.3 (long carrier lifetime) with the advantages of QDs (long spin relaxation times), which have been depicted in the chapters 1.2 and 1.4.
The embedment of low-dimensional structures into a matrix of an indirect semiconductor has already been performed at the beginning of the 1990$^{\text{th}}$ by Dawson et al. [10]. They observed that the Γ-point conduction band states in GaAs quantum wells were greatly shifted when layers of AlAs were surrounding the quantum well material. They could finally observe, that this led to the transformation from a

type I structure, with lowest-energy transitions in the GaAs solely, to a type II structure, with the lowest-energy transitions between valence band states in the GaAs Γ-point and the indirect X-valley conduction band states in the AlAs. In the following years this concept of the confinement driven band state shift was assigned to InAs structures which proved to have smaller conduction band effective masses and being consequently more sensitive to this effect. Furthermore, the quantum well structures were replaced by the stronger confined quantum dots. In these it was able to demonstrate exciton recombination times on the microsecond timescale [11], which was later initially explained as type II transition similar to the situation of the GaAs/AlAs quantum wells [12].
About at the same time, Shamirzaev et al. also started to investigate InAs quantum dots and quantum wells in AlAs, showing in 2003 that exciton lifetime even in the millisecond time regime are possible to realize in InAs/AlAs quantum dots [13]. Using the quantum wells as a role model to show the exact influence of the confinement on different conduction band symmetry points, Shamirzaev proved by both calculation and experiment, that InAs quantum wells possess indirect transition in the momentum space, while having a type I band alignment [14]. In the following, attempts were made to assign the results gathered for quantum wells on ensembles of quantum dots of the same material [15]. In ensembles of quantum dots it could further be shown that these consisted of either direct and indirect dots [16], dividable by the choice of the excitation energy, quantum dot size, respectively. With the development of the fundamental understanding of the electronic states in InAs/AlAs quantum dots, these could be used for more applied research [17] (coupling of indirect QDs) and detailed analysis for the finding of the limiting factors of the exciton lifetimes [18]. Finally, the carrier spin states became the center of attention also in indirect InAs/AlAs quantum dots, as on the one hand the repopulation of the spin states can be observed by the prolonged exciton lifetimes and on the other hand indirect excitons show reduced spin-orbit interactions decreasing the perturbation of the spin states and prolonging the spin dynamics [19, 20].
An overview about the used experimental details including specific setups is given in chapter 2. The main parts of this thesis, presenting the experimental results are given in the chapters 3-6 starting with the description of basic optical properties of the studied structures. In the following the excitonic and spin properties are examined under different conditions, allowing an insight into these fundamental aspects. The thesis is finalized by a summary in chapter 7 and an outlook about planned activities concerning indirect semiconductor structures with reduced dimensionality in chapter 8.

Chapter 1

Theoretical background

For the understanding of the fundamental properties, that will be seen in the scope of this work, a solid theoretical background is required. To ensure the consistency of this background, this chapter will examine the fundamental characteristics seen in semiconductor structures. In the first section, the general properties of bulk semiconductors and of the bound electron-hole states, called excitons, appearing in these structures will be discussed. The second section of the theoretical background will give an overview about the changes taking place with the reduction of the crystal dimensions. As will be seen, the energies and densities of states in these structures change significantly under the influence of confinement potentials. The indirect semiconductor structures analyzed in this thesis require furthermore the clarification of any deviations caused by indirect transitions. For this purpose, the third section gives attention to different realizations of semiconductor structures being indirect, both in real or momentum space. With the consideration of carrier and exciton spin states, the temporal evolution of single spin states becomes important. The corresponding relaxation mechanisms, limiting the spin lifetimes are consequently discussed in the fourth section.

1.1 Excitons in semiconductor crystals

A large part of the spectroscopic studies on semiconductor structures today is attributed to the excitation and corresponding emission of exciton complexes. These bound states allow one to obtain information about the electronic and optical properties of the semiconductor from which they originate from.
To understand this connectivity, the fundamental energy emissions from single atoms offer a good starting point. The emission spectra of atoms is discrete, meaning that their spectrum is dominated by specific lines which accord with the transitions between their orbital energy states.*

*The first observation of these lines was performed by Joseph von Fraunhofer, who measured dark lines in the solar spectrum. The origin of these lines was not determined at that time (1814),

Electrons forming the atomic shell perform these transitions and emit photons with energies equal to these orbital transitions. Fig. 1-1 depicts a schematic transition between the orbital energies E_1 and E_2, consistent with an emission of a photon with the energy of $E_{\mathrm{em}} = E_2 - E_1$. Apart from emissions caused by the orbital transitions, also absorptions can be observed, which correlate with these transitions. They represent energies necessary for an electronic transition into higher energy states. This process is additionally depicted in the lower half of Fig. 1-1 with the absorption energy $E_{\mathrm{ab}} = E_1 - E_2$.
The simplest atom in nature is the hydrogen atom, which enables a consequent formalization of these transition energies. As the atomic nucleus can be considered as nearly resting and massive compared to the single electron in the atomic shell, the electron transition energies can be calculated in the Born-Oppenheimer approximation. This approximation allows one to describes multi-particle systems under simplification of mostly stationary particles and only one additional particle in motion [22]. Prior to any calculation, Johannes Rydberg found that the emission wavelength λ coming from hydrogen orbitals can be described by the simple relation:

$$\frac{1}{\lambda} = R_{\mathrm{Ryd}} \left(\frac{1}{n_1^2} - \frac{1}{n_2^2} \right). \tag{1.1}$$

It reflects the quantized nature of the orbital energies of the hydrogen atom. The constant R_{Ryd}, which has a value of 13.6 eV in hydrogen and represents the vacuum energy for the electron, is called the Rydberg energy. The numbers n_1 and n_2 denote the orbital numbers taking part in the transition and have integer values, where $n = 1$ is the lowest-energy orbital.
If many atoms of the same or similar kind are arranged in an ordered and static manner, a solid state is formed, which is often ordered in crystal symmetries. Due to the large amount of atoms with associated carriers the interaction between atoms and carriers becomes increasingly important. As a consequence, the energy levels are no longer discrete but become continuous. These effects result in the formation of bands summarizing all energy levels into broad energy regimes, which can be populated by electrons. An intrinsic population of one of these bands is dependent on its absolute energy position and the value of the Fermi energy E_{F} describing the average population energy of carriers in solid states. If this energy coincides with one of the bands, it can be assumed that without any additional excitation the band is filled with carriers up to the Fermi energy. The lowest energy band in semiconductors intrinsically and completely populated by carriers is called the valence band (VB), while higher energy band not populated by carriers is called the conduction band (CB).
With the help of these bands a characterization of solid states into conductors, semiconductors and insulators can be made. Conductors have free carriers also in

but it could later be explained by G. R. Kirchhoff and R. Bunsen to arise from the absorptions of light in the photosphere of the sun itself [21].

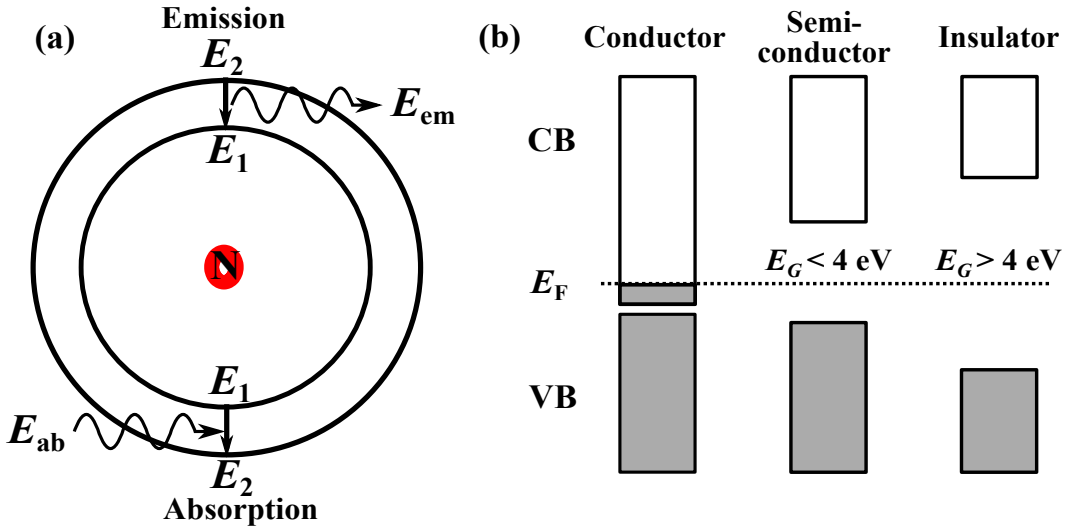

Figure 1-1: (a) Schematically depicted orbital transition for a model atom. The atomic nucleus (N) is marked by the red central disc. The atomic shell is pictured by the two orbitals with energy levels of E_1 and E_2. Absorption and emissions with corresponding energies E_{ab} and E_{em} of photons in the shell are illustrated by the waved arrows. Solid arrows depict electron transitions between the orbitals. (b) Characterization of three solid state types, referred to as conductor, semiconductor and insulator. The conduction (CB) and valence bands (VB) represent the energy states, which are allowed to be populated by carriers. The Fermi energy E_{F} describes the accessable energy of electrons without additional excitation and determines the intrinsic band population at low temperatures.

their lowest occupied band. They allow an exchange between free states and electrons in the conductor and consequently a transport of carriers with, for example, an externally applied electric field. Insulators, on the contrary, have completely filled valence bands and empty conduction bands. The bands are separated by a rather large energy difference, the band gap (E_{G}). In these structures the energy difference is sometimes also referred to as the forbidden zone, in which no electronic states are allowed. Typical insulators have band gaps exceeding 4 eV.
Semiconductors, have a composition similar to insulators, but have significantly smaller band gap energies lower than 4 eV. A description of the three solid state classifications is given in Fig. 1-1(b). The Fermi energy is located within the band gap, so that at low temperatures the CB is not populated by carriers and has the character of an insulator. With the application of external excitations such as optical illumination, electric potential or even with increased temperatures, electrons can be elevated from the VB to the CB. The typical band gap energy in semiconductors is equal to the energy of electromagnetic waves in the visible spectral range. This makes semiconductors useful for optical excitation studies.
The excitation of one electron from the VB into the CB causes at the former location of the electron the appearance of a discontinuity. Previous to the excitation, the VB was neutrally charged corresponding to the equal negative charge of the electrons and the positive charge of the nuclei. With one electron excited, this equilibrium is disturbed resulting in a locally positive charge excess, which can be

treated as a quasi-particle, the so-called hole. The hole is in many aspects comparable to an electron with positive charge. For instance, it can be responsible for current phenomena with the application of electric fields and its spin states can be split by magnetic fields.
To determine the energy levels which can be occupied by electrons and holes, an operator has to be constructed, which is able to describe the energy dependencies in the crystal following the eigenvalue equation: $\hat{H}\Psi = \tilde{E}\Psi$. The operator $\hat{H}$ applied to the wave function Ψ is called the Hamilton operator or short Hamiltonian, and results in an energy eigenvalue of $\tilde{E}$.
To create a Hamiltonian for the carrier energies in the band states following the second quantization, the number of states can be reduced for simplicity to two. Corresponding to the conduction and valence band, these states are indicated in the following by the indices $j = \mathrm{c}, \mathrm{v}$ [23]. The Hamiltonian under these conditions can be separated into two parts

$$\hat{H} = \hat{H}_0 + \hat{H}_1,$$

with the first one including all non-interacting terms:

$$\hat{H}_0 = \sum_{\vec{k}} \left(E_{\mathrm{v}}(\vec{k}) c^{\dagger}_{\mathrm{v}\vec{k}} c_{\mathrm{v}\vec{k}} + E_{\mathrm{c}}(\vec{k}) c^{\dagger}_{\mathrm{c}\vec{k}} c_{\mathrm{c}\vec{k}} \right). \tag{1.2}$$

The electron generator and annihilator operators are here represented by $c_j^{\dagger}$ and c_j and the valence and conduction band dispersions by $E_j(\vec{k})$. The second term $\hat{H}_1$ describes the interaction between electrons in the CB with those in the VB, but neglects the interaction of carriers within the same bands, as it can be assumed that the band dispersions $E_j(\vec{k})$ already include these interactions. The interaction term then takes the form:

$$\hat{H}_1 = \sum_{\vec{k}_1,\vec{k}_2,\vec{k}_3,\vec{k}_4} u_{\vec{k}_1,\vec{k}_2,\vec{k}_3,\vec{k}_4} c^{\dagger}_{\mathrm{v}\vec{k}_1} c^{\dagger}_{\mathrm{c}\vec{k}_2} c_{\mathrm{c}\vec{k}_3} c_{\mathrm{v}\vec{k}_4}. \tag{1.3}$$

With the interaction matrix elements $u_{\vec{k}_1,\vec{k}_2,\vec{k}_3,\vec{k}_4}$, which include the direct Coulomb interaction and disregard the exchange interaction. As a further simplification it is assumed, that the semiconductor is direct with its band gap at the Γ-symmetry point, so that the band dispersion follows the effective mass approach, resulting in:

$$E_{\mathrm{v}}(\vec{k}) = -\frac{\hbar^2 k^2}{2m_{\mathrm{v}}} \quad \text{and} \quad E_{\mathrm{c}}(\vec{k}) = E_{\mathrm{G}} + \frac{\hbar^2 k^2}{2m_{\mathrm{c}}}, \tag{1.4}$$

with the effective masses of the valence and conduction band m_{v} and m_{c}, respectively. With the assembly of the band states the minimal energy, necessary to excite electrons from the valence into the conduction band, should therefore be determined. However, the electrons and holes interact with each other by the Coulomb force, consisting of an attractive and a repulsive part. This interaction

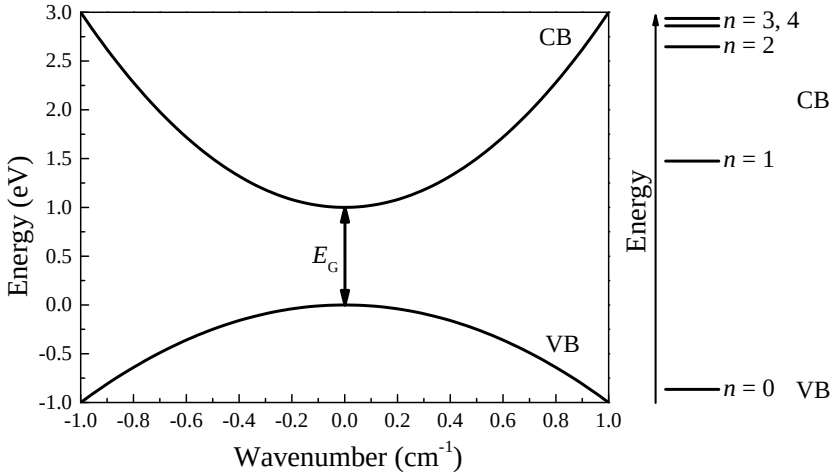

Figure 1-2: Energy dispersion of CB and VB in a bulk semiconductor crystal. The parabolic shape of the bands is attributed to the energy dispersions, see Eq. (1.4). The energy states for the excitons have been exemplarily calculated using Eq. (1.7) and are attached as a scheme at the right hand side of the figure. The energy scalings between the diagram and scheme are not in relation to each other. The style of the figure is adapted from [23].

leads to the formation of a bound state, the exciton. This state can be treated in analogy to the hydrogen atom, since both constructs consist of one positively and one negatively charged particle. In contrast to the hydrogen atom, the exciton has no quasi-static particle, so that the Born-Oppenheimer approximation is not valid, making necessary the introduction of relative coordinates and a description for the center of mass:

$$\vec{\mathrm{R}} = \frac{m_\mathrm{c}\vec{r}_1 + m_\mathrm{v}\vec{r}_2}{m_\mathrm{c} + m_\mathrm{v}} \quad \text{and} \quad \vec{r} = \vec{r}_1 - \vec{r}_2.$$

The vectors $\vec{r}_1$ and $\vec{r}_2$ therein describe the positions of the electron and hole, respectively. The use of this formalism together with a definition for the exciton effective mass $\mu = \frac{m_\mathrm{c} m_\mathrm{v}}{m_\mathrm{c}+m_\mathrm{v}}$ and the exciton wave function Ψ allows the establishment of the Schrödinger equation:

$$\left(-\frac{\hbar^2}{2(m_\mathrm{c}+m_\mathrm{v})}\nabla^2_{\vec{\mathrm{R}}} - \frac{\hbar^2}{2\mu}\nabla^2_{\vec{r}} - \frac{e^2}{\epsilon r} \right) \Psi = \tilde{E}\Psi. \tag{1.5}$$

The reduced Planck constant is here described by $\hbar$, the elementary charge is e and the permittivity is specified by ϵ. For solving of this equation, one can make use of the hydrogen atom solution, which results in the following eigenvalues:

$$\tilde{E}_{\vec{k},n} = \frac{\hbar^2 k^2}{2(m_\mathrm{c}+m_\mathrm{v})} - \frac{E_\mathrm{B}}{n^2}. \tag{1.6}$$

The energy E_B is here the binding energy of the exciton complex with $E_\mathrm{B} = \frac{\mu e^4}{2\epsilon^2\hbar^2}$ and an analog to the Rydberg energy for the hydrogen atom, which can also

describe excited states by use of integer numbers for n. With the eigenvalues of the Schrödinger equation, the energy dispersion of the exciton states can be calculated by:

$$E_{\mathrm{X}} = E_{\mathrm{G}} + \frac{\hbar^2 k^2}{2(m_{\mathrm{c}} + m_{\mathrm{v}})} - \frac{E_{\mathrm{B}}}{n^2}. \tag{1.7}$$

The band dispersions are depicted in Fig. 1-2 on the left hand side, while on the right hand side typical exciton energy states are depicted with the typical $1/n^2$-dependence. The state number $n = 0$ corresponds here to the absence of an exciton corresponding to an electron non-excited in the VB. In contrast to the hydrogen, the exciton is surrounded by a crystal which causes a static shielding, so that the effective charge is reduced by a factor of $1/\sqrt{\epsilon}$. Additionally, the size of the exciton can be significantly larger than the hydrogen atom and is larger than the Bohr radius by a factor of $\epsilon\frac{m}{\mu}$. The effective size of excitons can differ drastically and allows the organization of excitons into two subcategories, the Mott-Wannier and Frenkel excitons. The Mott-Wannier excitons depict here the case of excitons with large spatial gaps and small binding energies. These excitons are found in semiconductors with small band gaps, which have a large dielectric constant reducing the Coulomb interaction between the electrons and holes [25]. Frenkel excitons on the other hand have large binding energies of up to 1 eV and tend to be strongly located in their host materials. The typical size of these excitons is comparable to crystal unit cells. Frenkel excitons are mostly seen in materials with small dielectric constants [24].

1.2 Semiconductors of reduced dimensionality: Fabrication and characteristics

With an increasing understanding of semiconductor crystals and progress in the fabrication of highly-pure materials, the idea of artificial structures, engineered on a nanometer-scale, was the logical step. Unfortunately, the small size of the systems prohibits a mechanical construction, so that the desired arrangement of atoms can only be achieved with the aid of natural mechanisms. One of the fabrication processes using these mechanisms is the molecular-beam epitaxy (MBE), which enables one to control the growing process with an accuracy of single monolayers.

In this technique, a highly pure semiconductor substrate is placed in an ultrahigh vacuum chamber. Attached to the vacuum chamber are several evaporation cells with source materials, which can be evaporated using a heater plate. The shape of these cells and their direction allows to produce beams with homogeneous material densities to be emitted towards the substrate. The growth of a single monolayer typically takes between 1-5 s, depending on the materials used and their temperature as well as the temperature of the substrate. A simple shutter construction

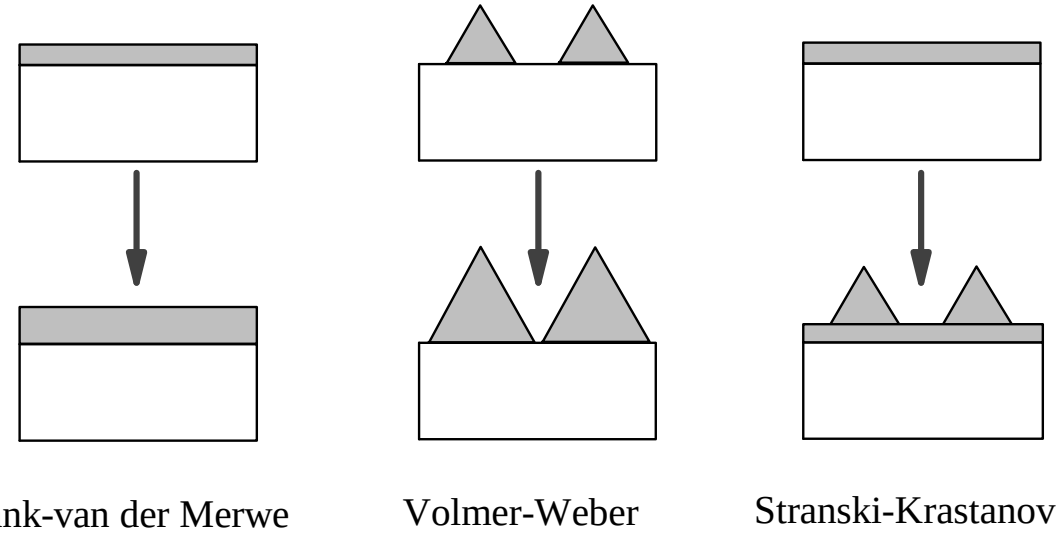

Figure 1-3: The three basic growth mode features of the MBE growth method. Evaporated materials attach to substrates differently, depending on the surface energies of the materials, the substrate and their common heterointerface. The Frank-van der Merwe mode represents the layer-by-layer growth, requiring the substrates surface energy (γ_1) to be higher than the deposited material's (γ_2) and heterointerfaces surface energies ($\gamma_{1,2}$), ($\gamma_1 > \gamma_2 + \gamma_{1,2}$). The Volmer-Weber mode on the contrary, depicts the situation, that the material's surface energy is higher than the substrate's one ($\gamma_1 < \gamma_2$). Finally, the Stranski-Krastanov growth mode describes the situation of an initial layer growth, followed by the formation of islands. This behavior is based on the increased heterointerfaces surface energies appearing with the growth of the first layers ($\gamma_1 < \gamma_2 + \gamma_{1,2}$). Figure according to [26].

with tenth of seconds operation time in front of the evaporation cells guarantees a control with single monolayer growth accuracy [26]. The heating temperatures during the growth process differ corresponding to the used material, but typically exceed 400°C. In contrast to this elevated temperatures are the cryogenic conditions of the screening surrounding the substrate, serving as a cold trap for scattered or evaporated atoms from the walls of the chamber.
The evaporated materials attach to the substrates surface forming thin films on a nanometer scale. Alternation of the evaporated materials consequently allows the construction of hetero-structures following three basic growth modes, named Frank-van der Merwe (FM), Volmer-Weber (VW) and Stranski-Krastanov (SK) growth mode [26]. The growth modes are governed by the surface energies and the lattice mismatch. Here, especially comparative studies of the surface energies of the materials γ_1/γ_2, and their interface $\gamma_{1,2}$ allow a prognosis of the dominating growth mode. The FM mode, which corresponds to a layer-by-layer growth, appears under the condition that the substrates surface energy is higher than the summation of the interface and deposited material surface energies $\gamma_1 > \gamma_2 + \gamma_{1,2}$. Figuratively, this means that the deposited material is attracted stronger to the substrate than to itself. In the opposite case, with $\gamma_1 < \gamma_2 + \gamma_{1,2}$, the material is attracted stronger to itself and consequently reduces the common surface with the

substrate, as seen in the VW mode [27]. The SK mode represents an intermediate case, in which initially a highly strained layer is formed and followed by the formation of islands. To explain this behavior it can be considered, that in the initial condition the surface energy of the substrate is larger than that of the other material resulting in the formation of a layer. With increasing layer thickness the interface surface energy increases, respectively. In case of the formation of islands on the surface, the combined material and interface surface energies finally exceed the substrates attraction.
A structure such as this, which is confined in all three dimensions and possesses a two-dimensional layer on which it has been formed on, is called a self-assembled quantum dot (QD) and drastically shows the influence of the confinement potential. QDs already depict the extreme case in the fabrication of semiconductor structures with reduced dimensionality, which can be classified by the number of dimensions not being confined. Consequently, QDs have a notation of zero-dimension (0D). Semiconductors without any confinement are accordingly called bulk semiconductors (3D), followed by quantum wells (QW/2D) and quantum wires (1D), whose confined dimensions are hence increased by one. In Fig. 1-4(b)-(e) the systems of reduced dimensionality in real space are schematically illustrated. Electron movements are strongly influenced in such structures, so that the electron energy is quantized and the distribution of free states is varied.
For the description of the changes induced by the confinement potential, one initially has to characterize the non-disturbed conditions observable in bulk semiconductors. The effective mass approximation allows an elementary description of energy and density of states characteristics, as has already been described in section 1.1. As in the previous case, a parabolic band dispersion can be assumed, equal to the situation in Fig. 1-2. The simplified Schrödinger equation then corresponds to [28]:

$$\left[-\frac{\hbar^2}{2m^*}\nabla^2 + V(\mathbf{r})\right] F_\mathrm{k}(\mathbf{r}) = \tilde{E} F_\mathrm{k}(\mathbf{r}). \tag{1.8}$$

The effective mass m^* is here supposed to be a general, isotropic electron effective mass without a link to any band, $V(\mathbf{r})$ is the confinement potential and $\tilde{E}$ is the energy eigenvalue. Instead of the previously used wave function $\Psi(\mathbf{r})$, the envelope wave function $F_\mathrm{k}(\mathbf{r})$ is used. The two wave functions are related to each other by the unit cell volume V_0 and the unit cell normalized Bloch function $u_0(\mathbf{r})$, following:

$$\Psi(\mathbf{r}) = \sqrt{V_0} F_\mathrm{k}(\mathbf{r}) u_0(\mathbf{r}). \tag{1.9}$$

Solving of the Schrödinger equation (1.8) for specific structures of reduced dimensionality, requires an adaption of the confinement potential. In the easiest case, the confinement potential of the three-dimensional bulk semiconductor is $V(\mathbf{r}) = 0$, that is (i.e.) equal to zero as the movement of electrons is not limited in any direction. Consequently, the energy eigenvalue corresponds to the parabolic energy dispersion as seen in Eq. (1.4). In addition to the energy eigenvalue, the density

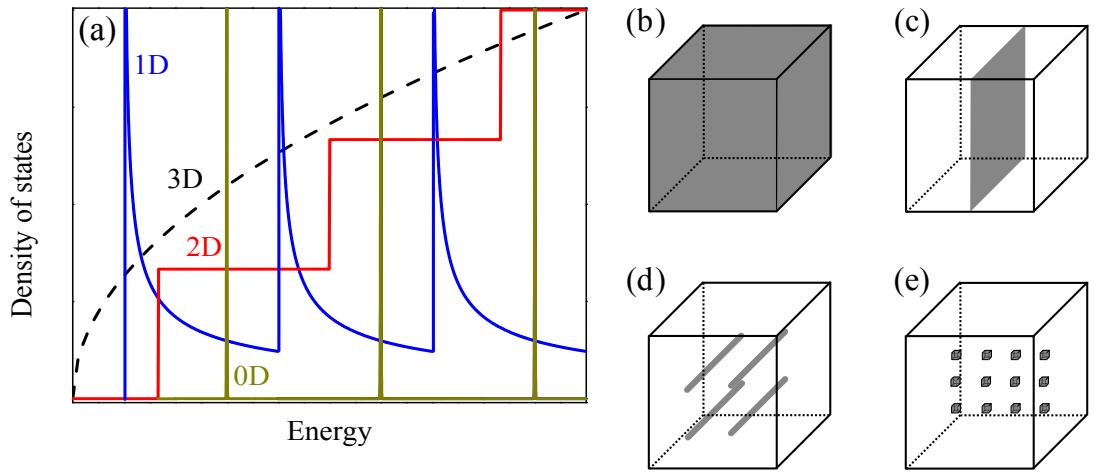

Figure 1-4: (a) Density of states for bulk crystals (3D) as well as systems of reduced dimensionality, such as QWs (2D), quantum wires (1D), and QDs (0D). While the density of states in bulk crystals follow a $\sqrt{E}$-dependence, illustrated by the black dashed line. A confinement already along one direction, as in case of QWs, causes a quantization of the states. The red line, following a Heavyside step function, illustrates the QW density of states. The situation presented by the blue graph, is attributed to quantum wires. These one-dimensional structures follow a $1/\sqrt{E}$-dependence, with singularities signifying the coincidence with the exact quantum wire eigen energies. The QDs finally, have only discretely allowed energy states, where their density of states is different to zero, shown by the green lines. (b)-(e) Illustration of the spatial elongation of bulk semiconductors (b), QWs (c), quantum wires (d), and QDs (e). Figures have been drawn after [28].

of states $D(E)$ is of key importance. It is defined as the number of states between two consecutive energies E and $E+dE$ of infinitesimal small distance. In the case of bulk semiconductors the calculation produces:

$$\begin{aligned} D(E) &= \frac{2}{V_0}\sum_k \delta[E(\mathbf{k})-E] \\ &= \frac{1}{2\pi^2}\left(\frac{2m^*}{\hbar^2}\right)^{3/2}\sqrt{E}. \end{aligned} \tag{1.10}$$

Therefore, the density of states follows a square root dependence with increasing energies. In Fig. 1-4 the density of state dependence, marked by 3D, is depicted by the black, dashed graph. In addition to the bulk semiconductor, the structures of reduced dimensionality are shown in the figure.
In the case of ideal quantum wells, the confinement potential is infinite in one direction (here z-direction) and zero in the other two directions. In contrast to this, real quantum wells possess a finite width L_z, so that the potential has to be described sequentially with $V(z) = \infty$ for $|z| \geq L_z/2$ and $V(z) = 0$ for $|z| < L_z/2$. These drastic changes of the confinement potential at the boundaries of the quantum well cause the wave function to vanish in the high confinement potential regime. Thus, the energy eigenvalue contains a quantized term in addition

to the parabolic energy dispersion along the unperturbed direction:

$$E(\mathbf{k}) = \frac{\hbar^2}{2m^*}\left[k^{\parallel 2} + \left(\frac{n_z\pi}{L_z}\right)^2\right], \tag{1.11}$$

where $k^{\parallel} = (k_x, k_y)$ is the wave vector parallel to the quantum well. In the quantized term the quantization number is $n_z = 1, 2, 3, ...$ describing the states of rising energy, where $n_z = 1$ is the ground state. The distance between the distinct energy levels increases with decreasing width of the quantum well, consequently reducing the number of energy levels present in the structure. The density of states is also changed by this quantization effect, as the maximum number of carriers that can occupy one energy state is limited and the energy levels itself are separated from each other. The corresponding density of state function is therefore dominated by a Heaviside step function consistently increasing the density of states by one when a threshold energy is exceeded [28]:

$$D(E) = \frac{m^*}{\pi\hbar^2 L_z}\sum_{n_z}\Theta(E - E_{n_z}). \tag{1.12}$$

For visualization, the energy dependence of the density of states in a quantum well is depicted as a red graph in Fig. 1-4(a) and additionally designated by 2D.
The one-dimensional confinement, taking place in so-called quantum wires, will only be briefly mentioned here, as these structures have their primary role in the research of transport phenomena, which will not be treated in this thesis. In these semiconductor structures one additional confinement direction appears, which becomes noticeable by one additional quantization number n_y. The density of states is implied in the figure by the blue graph and marked by 1D. It follows a $1/\sqrt{E}$-dependence with singularities at the energy positions, which are equal to the quantized states.
The zero-dimensional structures, finally, limit the carrier movement in all three dimensions. Electrons and holes trapped in ideal QDs are strongly localized because of the high potential barriers outside the QDs. Comparably to the QW situation, the description of the QD energy levels requires the definition of the boundaries in all three directions. The corresponding size values L_x, L_y and L_z then play a key role in the energy state separation. A continuous and parabolic energy dispersion as in the case of bulk semiconductors and in the dispersion parallel to quantum well interfaces is absent. Instead, the energy levels in QDs are completely quantized, resulting in:

$$E(\mathbf{k}) = \frac{\hbar^2}{2m^*}\left[\left(\frac{n_x\pi}{L_x}\right)^2 + \left(\frac{n_y\pi}{L_y}\right)^2 + \left(\frac{n_z\pi}{L_z}\right)^2\right]. \tag{1.13}$$

With $n_x, n_y, n_z = 1, 2, 3...$ being interger values and wave vectors, which are determined by the QD dimension: $\mathbf{k} = (n_x\pi/L_x, n_y\pi/L_y, n_z\pi/L_z)$. The density of states is accordingly a sequence of δ-functions and further depends on the volumes

density of QDs, N_{D}:

$$D(E) = 2N_{\mathrm{D}} \sum_{n_x n_y n_z} \delta(E - E_{n_x} - E_{n_y} - E_{n_z}). \tag{1.14}$$

Free carrier states therefore only arise with an exact compliance with the quantized energies. This can be schematically seen in Fig. 1-4 by the olive spikes representing the allowed states, which can be populated at specific energies. For a single, realistic QD this signifies, that only light with a very sharp energy distribution is emitted from the ground and excited states. Due to the quantized emission energies and other similarities such as orbital behavior, QDs are referred to as artificial atoms [29, 30].

Moreover, the size quantization has an additional effect on the valence band, i.e. on the holes states. In bulk semiconductors, a separation of hole states into light- (lh) and heavy-holes (hh) has been observed, which typically can be described by significantly different effective masses. Although possessing non-equal parabolic bands, both hole-states are degenerated in the center of the Brillouin-zone (Γ-point). These degenerated states are split by an energy of $\Delta E_{\text{hh-lh}}$ in the case of QDs causing the heavy-hole with its angular momentum projection of $J_z = \pm\frac{3}{2}$ to be the ground-state and the light-holes with a projection of $J_z = \pm\frac{1}{2}$ correspondingly to be higher energy states.

In comparison to the idealistically calculated QD in Eq. (1.13), an authentic self-assembled semiconductor QD is non-equally confined along the different dimensions. Perpendicular to the growth direction, i.e. in the xy-plane, the confinement is small compared to the high confinement along the growth- or z-direction. With this configuration, the crystal symmetry is reduced to D_{2d} [32], which is the same as predominating in QW structures. Even these considerations are idealistic, as uniaxial deformations can cause a further decrease of the symmetry to C_{2v}.[†]

For an exact elucidation of the optical and electronic properties in self-assembled QDs, the exchange interaction between the carriers inside the QDs has to be taken into account. The carrier confining nature of QDs causes an enhancement of interactions between carriers among themselves and between the carriers and the nuclear system. Disregarding the light-hole states, excitons consisting of one electron with spin states $\pm\frac{1}{2}$ and one heavy-hole with $J_z = \pm\frac{3}{2}$ angular momentum projection, allow four combination contingencies. The four exciton states can be distinguished by their angular momentum projection $M = \pm 1, \pm 2$. Excitons with a projection of ± 2 are optically inactive and are accordingly called dark states. In contrast to these, bright excitons have a projection of ± 1, can be directly excited using a single photon, and can ultimately recombine under the emission of a single photon. A comprising Hamiltonian including both bright and dark states and

[†]A detailed description of the theoretical background on crystal symmetries and their reduction is given in [34].

describing the exchange interaction then has to take the form [35]:

$$\hat{H}_{\text{exch}} = -\sum_{i=x,y,z} \left(a_i j_i s_i + b_i j_i^3 s_i \right). \tag{1.15}$$

The operators s_i and j_i ($i = x, y, z$) in the Hamiltonian represent the electron and heavy-hole spin operators. The values a_i and b_i stand for the dimensions of the quantum dots and can give rise to a decrease of the crystal symmetry.[‡] The first term describes here the isotropic exchange being responsible for energy differences between bright and dark exciton states. These are split from each other by the electron-hole exchange energy δ_0. In self-assembled QDs like (In,Ga)As/GaAs QDs this value has been estimated to be in the range of 100 μeV [35, 36], as will also be adopted for the (In,Al)As QDs, which are in the focus of this work.
In case of symmetrical QDs, with $b_x = b_y$ corresponding to the D_{2d} symmetry, the bright exciton states are still degenerated under consideration of the short-range exchange interaction solely, while the dark exciton states are split by an energy of δ_2. Only under the inclusion of the second term in the Hamiltonian, describing the long-range exchange interaction, and under the condition of a strained QD (C_{2v}-symmetry) a splitting of the bright exciton states is observed [37]. Without the additional application of magnetic fields these states are mixed and form linearly combined states with $|L_{1/2}\rangle = \frac{1}{\sqrt{2}}(|+1\rangle \pm |-1\rangle)$. These superpositioned states have a strong linear polarization and are the origin of the so-called optical alignment effect [38]. The long-range exchange interaction on the one hand additionally increases the splitting between the bright and dark states, while it has on the other hand no influence on the dark state splitting.
With the application of external magnetic fields, the consideration of the Zeeman splitting becomes necessary. The Zeeman effect describes the splitting of exciton as well as single particle spin states in dependence of the magnetic field strength in regard of the corresponding exciton or single particle Landé g-factor. With the application of a magnetic field with random orientation $\mathbf{B} = (B_x, B_y, B_z)$ the Zeeman Hamiltonian is described by:

$$\hat{H}_{\text{Z}}(B) = -\mu_B \sum_{i=x,y,z} (g_{\text{el},i} s_i - 2\kappa_{\text{KL},i} j_i - 2q_{\text{KL},i} j_i^3) B_i. \tag{1.16}$$

Included in the Hamilton operator are the electron g-factor $g_{\text{el},i}$ and the Luttinger-Kohn parameter $\kappa_{\text{KL},i}$ and $q_{\text{KL},i}$ ($\kappa_{\text{KL}} \gg q_{\text{KL}}$). The use of these parameters instead of a constant hole g-factor describes the strong non-linear hole-splitting based on

[‡]The relevance of the parameters becomes obvious with the assembly of the exchange interaction matrix:

$$\hat{H}_{\text{exch}} = \begin{pmatrix} +\delta_0 & +\delta_1 & 0 & 0 \\ +\delta_1 & +\delta_0 & 0 & 0 \\ 0 & 0 & -\delta_0 & +\delta_2 \\ 0 & 0 & +\delta_2 & -\delta_0 \end{pmatrix}$$

And the formation of the abbreviations: $\delta_0 = 1.5(a_z + 2.25b_z)$, $\delta_1 = 0.75(b_x - b_y)$, and $\delta_2 = 0.75(b_x + b_y)$, which are taken from [35] as examples.

band mixings with magnetic field, which dominantly influence the Zeeman effect. Therefore, the corresponding hole g-factor would change with magnetic fields. In QD systems with high symmetry on the other hand, a linear Zeeman splitting of the exciton states, consequently including the holes, has been observed, so that at least in an approach for a fixed magnetic field direction as in the case of the Faraday geometry ($\mathbf{B} = (0, 0, B_z)$), a linear relation as $g_{\mathrm{hh},z} = c_1\kappa_{\mathrm{KL},z} + c_2 q_{\mathrm{KL},z}$ may be used [35]. The exact values of c_1 and c_2 depend on the structure geometry and material. In case of high symmetries like D_{2d} the parameter $q_{\mathrm{KL},i}$ can even be considered to be equal to zero. Following this relation a definition of bright (g_1) and dark exciton state g-factors (g_2) is achieved as a linear combination of their electron and heavy-hole properties: $g_1 = g_{\mathrm{hh}} - g_{\mathrm{el}}$ and $g_2 = g_{\mathrm{hh}} + g_{\mathrm{el}}$. A reduced Zeeman Hamiltonian in Faraday geometry together with the exchange interaction contribution based on $\hat{H}_{\mathrm{exch}}$ allows a full description of the exciton fine structure splitting resulting in the energy states of [32]:

$$E^1_{\pm} = \frac{1}{2}\left(\delta_0 \pm \sqrt{\delta_1^2 + (\mu_{\mathrm{B}} g_1 B)^2}\right) \tag{1.17}$$

$$E^2_{\pm} = \frac{1}{2}\left(-\delta_0 \pm \sqrt{\delta_2^2 + (\mu_{\mathrm{B}} g_2 B)^2}\right), \tag{1.18}$$

with E^1 regarding the bright and E^2 the dark exciton states. With increasing magnetic field strength, the intrinsic splitting mechanisms become recessive in comparison to the increasing Zeeman splitting.
The dark states often pose the exciton ground states in QDs, while bright states are slightly higher in energy. At discrete magnetic field strengths, a sudden increase of the radiative emission from the bright excitons can often be detected. This effect is caused by a crossing of dark and bright states, shifted independently by their respective g-factors.
Moreover, the anisotropic exchange interaction can be responsible for the spin-flip processes as it induces mutual flip-flop transitions between the carriers. Such processes can even become dominant, as has recently been shown for CdTe/(Cd,Mg)Te QWs with D_{2d} symmetry [39].

1.3 Indirect semiconductor structures

With the introduction of semiconductor nanostructures in section 1.2, the term indirect semiconductor needs further specification. Accordingly, indirect semiconductor nanostructures can exist in two different versions, one favoring band transitions indirect in real space and the other favoring indirect band transitions in the momentum space. The structures, which are indirect in real space, acquired attention with the advent of heterostructures like QWs. These will be used as a role model for indirect transitions in real space in the following. The possibility to grow semiconductors with a monolayer precision allowed to combine materials with very different conduction and valence band offsets. This engineering of

heterostructures enabled more complex band characteristics than the simple construction of potential wells, which could be used as carrier traps. A type I QW here refers to a band structure, in which both conduction and valence band are lower in energy compared to the surrounding semiconductor bands. As a result, electrons and holes excited in both the QW material or in the surrounding matrix material relax down to the lowest energy states of the QW until their recombination occurs.
In contrast to that, a type II QW structure with two random material compositions A and B causes a separation of excited carriers. For that purpose, the conduction band energy of one material has to pose the lowest energy state for electrons, while the valence band energies of the second material has to be lower than for the first one. Under these conditions, excited electrons are accumulated in the conduction band of one material while the corresponding holes do the same in the valence band of the second material. The two types of QW structures are described in Fig. 1-5 to illustrate especially the role of band offsets.
With electrons and holes excited into the conduction and valence band, respectively, the Coulomb interaction emerges, resulting in a strong attraction between both carrier types. In the QW materials this interaction becomes noticeable by an accumulation of carriers especially at the heterointerfaces, as the carriers are dragged towards each other. With an increased number of oppositely charged carriers at the heterointerface an electric field is formed, bending the effective band states to lower energies. This band bending effect is known as the so-called optical Stark effect shifting the emission caused by the carrier recombination to lower energies.
The spatial separation of the carriers reduces the overlap of their wave functions. Consequently, the coupling strength is significantly reduced, drastically influencing the recombination dynamics. With the strongly increased lifetime of the carriers, the emission, resulting from radiative recombination processes, is prolonged by several orders of magnitude.
The second and more thoroughly investigated indirect semiconductor type is indirect in the momentum space, which correspond to the reciprocal lattice. Semiconductors with indirect transitions in the momentum space, do not require reduced symmetries. In fact, the most frequently used semiconductors in modern technology are based on the indirect bulk semiconductors Silicon (Si) and Germanium (Ge). The indirect transitions in these materials can be observed in band diagrams, which pose an extension of the energy dispersion seen in Fig. 1-2. In these, the energy levels are plotted against the wave vector $\vec{k}$ in all three dimensions ending at points of special symmetry.
For the understanding of these points of symmetry, the investigation of the first Brillouin zone is necessary. The Brillouin zone is defined as the primitive crystal cell in the reciprocal space, so that the characteristics seen in the first zone are correspondingly repeated, but not changed in neighboring cells; thus, they follow the translation symmetries and can be expressed using a set of reciprocal lattice vectors a_1, a_2 and a_3 [40]. The Brillouin zone of the face centerd cubic (fcc) lattice, which is one of the most frequent lattice structures in semiconductors, is depicted

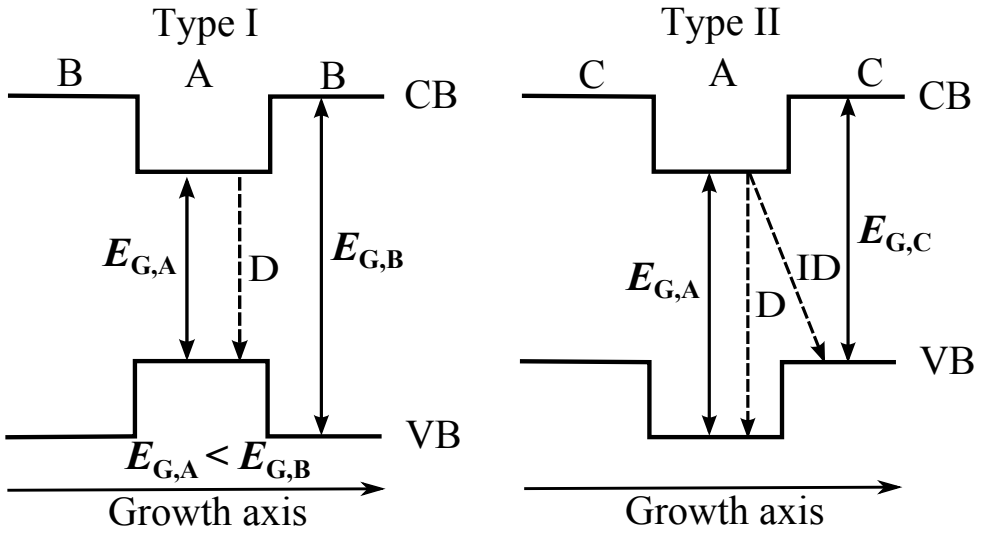

Figure 1-5: Representative band schemes of two QWs with type I and type II band alignments; all illustrated band edges refer to Γ-point energies. The two material compositions A and B in a QW structure with type I band alignment possess different large band gaps $E_{\mathrm{G,A/B}}$, with the material A having a smaller band gap following $E_{\mathrm{G,A}} < E_{\mathrm{G,B}}$ and negative offsets for both the conduction band (CB) as well as the valence band (VB) in respect to material B. Consequently, carriers relax down to the band edges of material A, where they radiatively recombine efficiently due to the overlapping wave functions. In a type II band alignment the conduction and valence band offsets have different signs, meaning that each material (in the right hand case, A and C) provides one band edge with the lowest energy level. In the case depicted, the lowest conduction band states can be found in material A, while C has a higher lying valence band state. Accordingly, the PL emission from a type II structure has its origin in the recombination of spatially separated carriers, representing an indirect transition (ID) in real space. Additionally, direct transitions coming solely from material A or C could also be identified, illustrated for material A by the transition D.

in Fig. 1-6(a) [27].

As shown in the schematic, the center of the Brillouin zone is marked by the Γ-point, which corresponds to a wave vector value equal to zero in band dispersions. In most direct semiconductors, optical transitions take place in or in the vicinity of this point due to the momentum conservation, which could otherwise not be provided by an optical excitation. Beside the center of the Brillouin zone, the X- and L-symmetry points are of high importance in the (fcc) lattices. The X-valleys, as seen in the Fig. 1-6(a) are aligned along the (100), (010), and (001) crystal axis and its antiparallel directions $(\bar{1}00)$,$(0\bar{1}0)$, and $(00\bar{1})$. As a consequence, indirect semiconductors with their lowest conduction band states in the X-valleys, have six degenerate X-valleys, which can be populated by carriers. For example, Silicon, in contrast to the depicted structure in Fig. 1-6, is arranged in the diamond crystal

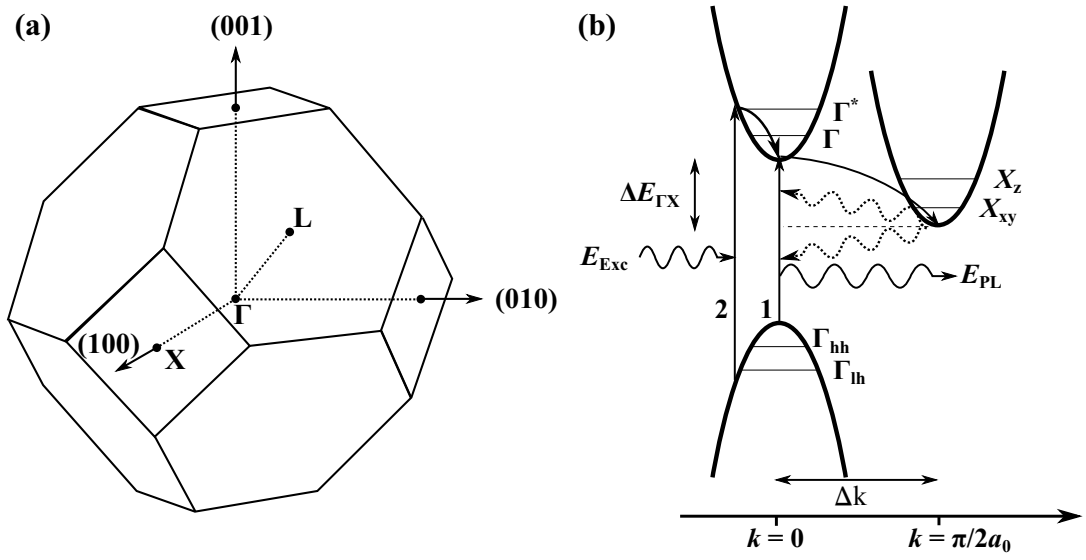

Figure 1-6: (a) First Brillouin zone of the fcc lattice. The scheme represents the primitive cell of the reziprocal lattice and illustrates points of high symmetry, like the center of the first Brillouin zone, the Γ-point. Additional points of interest marked in the scheme, are the 6-folded degenerated X-valleys and the 8-folded degenerated L-valleys. In resemblance to [27]. (b) Scheme of an indirect semiconductor band dispersion with optical allowed transitions in the Γ-valley and lowest energy level in the X-valleys. Photons with an energy of E_{Exc} cause the vertical excitation transition at the exact center of the Brillouin zone at $k = 0$ (**1**) or in their close proximity followed by a relaxation to the exciton ground state (**2**). By emission of an acoustic phonon, an electron can further relax from the lowest energy state in the Γ-point to the lower lying X-valley state (shifted by $\Delta E_{\Gamma-X}$). The momentum mismatch Δk between electrons in the X-valleys and holes left in the Γ-point prohibit an efficient recombination of corresponding electron-hole pairs. To overcome the momentum mismatch, a second phonon emission/absorption has to take place (illustrated by dotted, waved arrows), slightly changing the corresponding emission energy E_{PL}. Included in the scheme, are additional discrete energy levels, signifying the condition present in indirect QD structures.

lattice and has its lowest conduction band state in the vicinity of the X-valleys.[§] With additionally applied strain along specific axes or by a reduction of the structure dimensionality, as in case of self-assembled QDs, these previously degenerated X-valley states can be split. In Fig. 1-6(b), the energy scheme of an indirect semiconductor is drafted to indicate optically allowed and forbidden transitions. In the case depicted, the lowest optically allowed transition can be found between heavy-holes and electrons, both situated in the Γ-point. A photon interacting with the semiconductor crystal has nearly zero momentum, so that only vertical transitions can occur in the scheme. These include not only transitions at the exact center of the Brillouin zone (transition 1), but also those with the same momentum value (transition 2). Based on the scheme, this would require an increased amount of

[§]The exact lowest conduction band state can be found on 85 % of the way of a straight line between the Γ- and X-symmetry point [41].

energy due to the parabolic nature of bulk valence and conduction band states. This process is subsequently followed by non-radiative relaxation processes to the lowest Γ-state.¶ In both transitions, an allowed relaxation process is accompanied by a scattering with the lattice, leading to an absorption or emission of a phonon. In such a case, the carriers gain sufficient momentum to reach valleys on the Brillouin-zone edge. In the scheme, this is one of the X-valleys with a momentum of $k = \frac{\pi}{2a_0}$, in which a_0 stands for the primitive crystal cell length.
The electron occupying one of the X-valley states has an increased lifetime in the following, especially at low temperatures. This effect is explained by the condition, that the electron can only radiatively recombine with the hole left in the Γ-state. The mismatch of the wave vector Δk between these two carriers in contrast prohibits an annihilation back to the vacuum state.
As shown by the scheme in Fig. 1-6(b), a recombination from this indirect state mainly occurs phonon-assisted, absorbing or emitting a phonon in the process. As the absorption/emission of a phonon increases/decreases the energy of the indirect electron-hole pair, the waved arrows are not drawn horizontally but with some angle to describe this effect. Therefore, this effect results in a relatively broad emission energy spectrum of indirect transitions compared to direct ones. Another possibility, especially becoming important at low temperature, when the phonon population is drastically reduced, is a carrier scattering event on the surface or a heterointerface of the semiconductor [18]. This event enables a sufficient transfer of momentum allowing a recombination process to take place. Recent attempts to combine the features of indirect semiconductors with those of zero-dimensional nanostructures for applications in spintronics led to the construction of the (In,Al)As/AlAs QDs, which have a type I band alignment and are indirect in the phase space. The analysis of their electronic and additionally their spin properties are the main theme of this thesis.
Beside indirect transitions, including the indirect X-valley, other symmetry points may hold the lowest conduction or valence band states instead. For example, Germanium (Ge) has its lowest conduction band state in the L-valleys. As illustrated in Fig. 1-6(a), the L-valleys are aligned along the (111) direction and consequently form 8 degenerate L-valleys. Attempts to build nanostructures similar to those, who represent the center of this thesis, the indirect (In,Al)As/AlAs QDs, have succeeded by the growth of indium antimonide (InSb) QDs. Results concerning these structures will be presented as an outlook at the end of this thesis.

1.4 Spin dynamics in semiconductor nanostructures

As the spin of single carriers or complexes in semiconductor is considered a promising candidate to replace the carrier charge as the dominating unit in electronics,

¶With quantized energy levels, as in case of indirect QDs, any non-resonant excitation like seen in the transition 2 could not take place, as the energy dispersion is not continuous.

the dynamical behavior of its states is of great importance. The spin relaxation describes in this sense the repopulation of an initially non-equilibrium populated spin state ensemble back to a condition closer to its equilibrium. Some text books describe the phenomenon of spin relaxation as the interaction between the spin states with a fluctuation of a magnetic field in time [42], resulting in the reorganization of the spin state population.
The two main parameters characterizing such a fluctuating magnetic field are the root mean square (rms) value, representing the temporal adjusted amplitude and its correlation time τ_c. The correlation time represents the time in which changes in the amplitude of the magnetic field are negligible. With a magnetic field aligned randomly, the spin state starts to precess around the axis of the magnetic field with a precession frequency of ω, dependent on the amplitude of the magnetic field. After a time τ_c, the direction of the magnetic field changes, so that additionally the spin state has to change its precession direction following the fluctuating magnetic field. As a final outcome of this precession, the initially defined spin direction is lost. The origins of the fluctuation field responsible for the spin relaxation are manifold and cover spin-orbit, exchange, and even hyperfine interaction. In this context it should be pointed out, that the holes show a significantly stronger spin-orbit interaction, so that their relaxation times are several orders of magnitude shorter than for electrons. Electrons on the other hand have a much stronger coupling to the nuclear spin system, which manifests itself as the dominant spin relaxation especially for low-dimensional structures, where the spatial confinement of electrons is very strong.
To start with bulk semiconductors without the additional application of external magnetic fields, three major spin relaxation mechanisms have been categorized, the D'yakonov-Perel, Elliott-Yafet and the Bir-Aronov-Pikus mechanism.
From those, the last mentioned spin relaxation mechanism is dominant in heavily p-doped structures. This mechanism is based on the exchange scattering of electrons in the conduction band with electrons in the valence band. Therefore, this mechanism is highly dependent on the density of holes in the semiconductor. This scattering mechanism, leading to the spin-flip of electrons, is calculated via Fermi's golden rule under the assumption that in most bulk semiconductors heavy-hole states dominate the scattering process. In literature like [43], the elastic scattering and consequently the spin relaxation rate for electrons scattering with unbound holes is approximated by:

$$\frac{1}{\tau_\mathrm{s}} = \frac{2}{\tau_0} n_\mathrm{h} a_\mathrm{B}^3 \frac{\langle v_k \rangle}{v_\mathrm{B}}. \tag{1.19}$$

This approach only takes into account the short-range interaction and is solely valid for a non-degenerate hole system [44]. The equation includes the exciton Bohr radius a_B, the hole density n_h, and the average electron velocity $\langle v_k \rangle$. The factor $1/\tau_0$ is defined as $1/\tau_0 = (3\pi/64\hbar)\Delta E_\mathrm{SR}^2/E_\mathrm{Bo}$ with the short-range interaction splitting E_SR and the exciton Bohr energy E_Bo. Furthermore, the parameter v_B is defined by the reduced mass of the interacting electron-hole pair m_R by

$v_B = \hbar/a_B m_R$. The strength of this relaxation mechanism is heavily depending on the formulation of the hole concentration and condition. Thus, the scattering rate in Eq. (1.19) changes drastically under different degenerate/non-degenerate hole conditions and changes from free to bound hole conditions. Further corrections have to be included, when the short-range interaction is not sufficient to describe the complete situation in the semiconductor, so that the long-range interaction has to be considered.

The Elliot-Yafet mechanism [45, 46] is based on the coupling of electronic states of opposite spin. This coupling is mediated by the spin-orbit interaction, mixing the spin-up and spin-down electron eigenstates,

$$\begin{aligned} \Psi_\uparrow &= a|\uparrow\rangle + b|\downarrow\rangle, \\ \Psi_\downarrow &= a^*|\downarrow\rangle + b^*|\uparrow\rangle. \end{aligned}$$

The parameters a and b are used here as coupling parameters. The typical spin mixing is very small, which can be expressed by $|b| \ll 1$ and $|a| \approx 1$. For small spin-orbit interactions, the exact value of b can be calculated, using the perturbation theory, which leads to $|b|\ \max\{L_{SO}/\Delta E\}$ [47]. The spin-orbit interaction with other bands is described by L_{SO}, while the energetical distance to neighboring bands is ΔE. This implies, that the Elliott-Yafet relaxation mechanism especially takes place in semiconductors with small band gaps [48]. With these mixing conditions, any spin-independent scattering can induce a spin-flip process with a consequent spin relaxation. A special case of this mechanism is introduced by a phonon modulation of the spin-orbit interaction, since the spin-orbit interaction is related to the periodic arrangement of ions in the lattice. A lattice vibration (phonon) can directly couple to the electron spins leading to a spin-flip and, as a consequece, to a relaxation of the spin.
While the original mixing, without consideration of phonons, is called the Elliott process, the later process is named after Yafet [45]. As both mechanisms are closely related and complement to each other, they are often in conjunction referred to as the Elliott-Yafet mechanism. Next to the modulation caused by phonons, the momentum scatterings on impurities can result in the same effect, so that even at low temperatures, when the phonon population is small, the Elliott-Yafet mechanism can occur.
Both, Elliott and Yafet, developed expressions for the spin relaxation time in relation to changes of the electron g-factor in the first case and in dependence on the resistivity in the second case. In the Elliott relation, the inverse spin relaxation time is $1/\tau_s \approx (\Delta g)^2/\tau_p$, with $\Delta g = g - g_0$, as the deviation of the electron g-factor from the free electron one and the average momentum scattering time τ_p. Yafet on the contrary, used the resistivity ρ and the square of the average coupling parameter $\langle b^2 \rangle$: $1/\tau_s \sim \langle b^2 \rangle \rho$. In experimental studies, both relations have been confirmed, except for their coefficients and the agreements between theory and measurement have been validated in publications [49, 50].

The D'yakonov-Perel mechanism finally, is a spin relaxation process, which is mainly appearing in III-V and II-VI semiconductors. These structures lack any inversion symmetry in their lattice, so that the spin-orbit coupling can easily arise in the conduction band.
In contrast to the two mechanisms mentioned previously, the influence of the D'yakonov-Perel mechanism can even be increased, when the crystal dimensionalities are reduced, since they contribute to the spin-orbit interaction by their additional interface inversion asymmetry. The spin-orbit interaction manifests itself as a **k**-dependent effective magnetic field, forcing the electron spin to precess around its direction. An effective Hamiltonian describing this situation, is written in the form $\hat{H}_{\mathrm{SO}} = \frac{1}{2}\,\Omega(\mathbf{k}) \cdot \sigma$, where $\Omega(\mathbf{k})$ is the spin precession or Larmor frequency and σ the electron spin operator. With each momentum scattering event the direction of the effective magnetic field changes, because the momentum **k** of the electrons, on which the magnetic field depends, is changed. The spin precession varies randomly between scattering events, finally leading to a spin relaxation [51, 52].
The properties of the D'yakonov-Perel mechanism can be defined for two different regimes: One with strong (i) and the other with weak scattering conditions (ii). In the strong scattering regime (i), with $\langle\Omega\rangle\tau_{\mathrm{p}} \ll 1$, the spin relaxation time can be estimated by $1/\tau_{\mathrm{s}} = \langle\Omega^2\rangle\tau_{\mathrm{p}}$. As in the D'yakonov-Perel mechanism the spin relaxation mostly takes place between scattering events, the spin relaxation time is prolonged for stronger momentum scattering. In the weak scattering regime (ii), with $\langle\Omega\rangle\tau_{\mathrm{p}} \gtrsim 1$, the spin relaxation is not so drastically hindered by scattering events. On the contrary, momentum scatterings provide an efficient relaxation channel in interaction with the spin-orbit coupling here, so that the momentum scattering causes shorter spin relaxation times. Calculations based on electron scattering solely have predicted the spin relaxation time to $\tau_{\mathrm{s}} = 2\tau_{\mathrm{p}}$ [53]. The D'yakonov-Perel mechanism is known to dominate the spin relaxation especially in two-dimensional structures like QWs [54, 55].

As has been observed, the spin relaxation in bulk semiconductors (as well as in two-dimensional structures) is dominated by spin-orbit mechanisms, mostly induced by scattering processes between carriers or with phonons and impurities. Typical relaxation times are in the range of several hundreds of picoseconds [56]. In contrast to the three-dimensional problem, the spin relaxation in QDs follow different fundamental conditions. As the conduction and valence band states are highly quantized in QDs, the dissipation of energy during spin-flip events is more complicated. Furthermore, electron-electron scatterings can mostly be excluded, as the number of electrons is extremely limited (two electrons in the conduction band ground state S=1), due to large energy differences between conduction band levels and the Pauli-blocking. With the most effective spin relaxation mechanisms canceled out, the spin lifetimes in QDs are significantly prolonged and can range into the microsecond and even millisecond regime.
In the case of low temperatures and under the application of strong external magnetic fields, single-phonon emission processes are dominating [57]. Here, the

acoustic phonons cause the energy dissipation, which arises between spin levels in high magnetic fields. The strong coupling between the electron spin states and their bosonic environment is enabled via the piezoelectric interaction with acoustic phonons [58]. While these phonons are responsible for the dissipation of energy, they cannot change the carrier spin on their own, which is compensated by a coupling with the spin-orbit regime. The exact scattering rate, and the spin relaxation time, respectively, strongly depend on the exact QD geometry, so that it will be renounced to elucidate all single phonon based spin relaxation dependencies here. Detailed descriptions for the various dependencies are given in [57, 58, 59]. With increasing magnetic fields and correspondingly with increased Zeeman splitting, the single phonon coupled spin relaxation times decrease. The reason for this phenomenon can be found in the phonon energy distribution, as the population of phonons with higher energies is higher than for those with low energy. The single phonon spin relaxation mechanisms all together show consequently a typical magnetic field or Zeeman energy dependence of $\tau_\mathrm{s} \sim (g\mu_\mathrm{B}B)^{-5}$.
In the absence of strong external magnetic fields, the nuclear spin system also needs to be considered as an origin of carrier spin relaxations. Disordered nuclear spins give rise to an effective fluctuating magnetic field, which causes the carrier spins to precess around its variable direction with time. While in case of free carriers this mechanism is ineffective, the spatial confinement of carriers, as in the case of QDs or donor bound electrons, greatly increases the effectiveness of this mechanism due to increased nuclear fields up to several tenth of mT [60].
With the relaxation of one electron spin state to the equivalent opposite spin state, both the momentum and the energy need to be dissipated. In case of the nuclear spin system, as the coupling partner for the electrons, the momentum component can be easily absorbed while the energy transfer requires some specific conditions. The Zeeman energy of the nuclear spin system, with single nuclear spins $\mathbf{I}_n$, is equal to [61]:

$$\hat{H}_\mathrm{ZN} = -\mu_\mathrm{N} \sum_n g_n(\mathbf{B}\mathbf{I}_n). \tag{1.20}$$

Thus, the Hamilton operator summarizes over all single spins, and additionally includes the g-factor of the n-th nucleus. The nuclear magneton with
$\mu_n = 3.15 \cdot 10^{-8}$ eV/T is approximately 2000 times smaller than the corresponding Bohr magneton with $\mu_\mathrm{B} = 5.79 \cdot 10^{-5}$ eV/T associated to electrons. The corresponding Zeeman energies are equally different, so that the electron spin states shift significantly stronger in external magnetic fields B_ext. The fast diverging Zeeman energies with increasing external magnetic fields prevent an efficient coupling between the electron and nuclear spin systems exceeding a regime of only tenth of mT. Finally, the nuclear spin system can be taken as completely polarized in high magnetic field regimes, exceeding one Tesla. Their contribution to an effective magnetic field, consisting of external magnetic fields and the nuclear magnetic field B_N, following $B_\mathrm{eff} = B_\mathrm{ext} + B_\mathrm{N}$, can be neglected.

Chapter 2

Experimental details

The experimental setups used for the studies described are based on the optical excitation of exciton complexes and the measurement of their optical response. The process of optical excitation on the one hand and optical information readout on the other hand is called the photoluminescence (PL). As the experimental conditions concerning the sample mounting, their temperature control and the application of magnetic fields along specific axes are equal for several setups, these common conditions will be treated firstly and separated from specific methods. Despite their similarities, the measuring techniques can be categorized into the steady-state PL measurement, the time-resolved PL decay measurement, PL measurements under selective excitation with and without the use of polarization optics and finally the spin-flip Raman scattering spectroscopy, which is based on the elastic scattering of photons with the semiconductor nanostructures.
As long as not mentioned otherwise, the samples have been placed in a variable temperature inset (VTI) of an optical bath cryostat. The samples have been inserted in an envelope of black paper, allowing to fix them stress-free on the metallic sample holder. For constant temperatures above the liquid helium temperature of $T_{\mathrm{He}} = 4.2$ K, the samples were either cooled by a helium gas flow and heated by an electrical resistor, whose heating efficiency can be controlled by the electric current. The exact temperature was continuously measured by a temperature sensitive resistor, called Cernox, becoming increasingly sensitive at low temperatures. For the realization of temperatures below the critical temperature of $T_\lambda < 2.18$ K the VTI is flooded with liquid helium. The vapor of the liquid helium is in the following pumped away until a pressure below 50 mbar is reached. Under these conditions the λ-point is reached, resulting in the aggregate state of superfluid helium. With the control over the pressure, temperatures between 1.6 K $< T <$ 2.1 K can be achieved in the cryostats. The bath cryostats, as well as their VTI, are optical accessible via four windows along the two main axes. The windows are made of a special glass type, called Supersil, known to be completely optical inactive. For the application of high magnetic fields a superconducting split-coil magnet is implemented to the cryostat system. This magnet is cooled by the cryostats own liquid helium reservoir and reach typically magnetic field strengths of up to 10 T.

One drawback of these high magnetic field cryostats is the permanent magnetization of the magnet coils. Even without the application of current into the coils, a persistent magnetic field can be measured in these systems in the range of 50 to 70 mT. Measurement requiring the absence of magnetic fields or the presence of very small fields in the mT range, are consequently performed in an alternative cryostat system without a superconducting magnet implemented into the system. Instead, two pairs of electromagnets are attached to the exterior of the cryostat compensating the earth magnetic field and any rest magnetization. Furthermore, they provide well directed weak magnetic fields for measurements in the mT range.

2.1 Steady-state photoluminescence

A large portion of the acquired results has been gathered by the technique of photoluminescence. In this work, one has to divide between above-barrier excited and selectively/resonantly excited PL. The first mentioned case has no special requirements for the excitation source except larger excitation energies than the band gap energies of the structures under analysis. The latter excitation condition on the contrary, requires excitation energies resonant to the PL emission and therefore the ability to tune the excitation energy following the PL distribution. In the present case these requirements are fulfilled by the use of an optically pumped Ti:Sapphire laser (Tekhnoscan, T&D-scan), which emits at a wavelength range between 700 to 1050 nm. The linewidth of about 1 μeV for the excitation beam is at the same time very sharp, so that the appearance of stray light in the PL observation in vicinity to the laser energy is ab initio reduced. The basic setup used for the steady-state photoluminescence measurements is comparable to the setup shown in Fig. 2-1.* After exiting the laser, the beam of light is directed by mirrors through power reducing optical elements. These can be realized by an attenuating gradient neutral filter or as shown in the figure by the combination of a half-wave retardation plate followed by a Glan-Thompson prism. In the latter combination, the laser power density is reduced by the mismatch between the laser linear polarization vector and the one of the prism. The component perpendicular to the transmitting polarization direction of the prism is reflected and consecutively blocked, while the retardation plate allows to turn the laser polarization towards or further away from the transmission direction, respectively increasing or decreasing the excitation power in the process. The excitation beam, exemplarily illustrated by a Nd:YVO_4-laser, illuminates the sample with a small angle in respect to the optical axis, initiating the PL. The non-directional emitted PL is in the following gathered by a lens collecting the conic section of the signal, defined by the lens focal length f and its size in diameter D. The ratio between these two parameters is called the numerical aperture $N = f/D$, describing firstly the resolving power of

*The additional temporal synchronization between excitation source and detecting device can be disregarded for the steady-state technique.

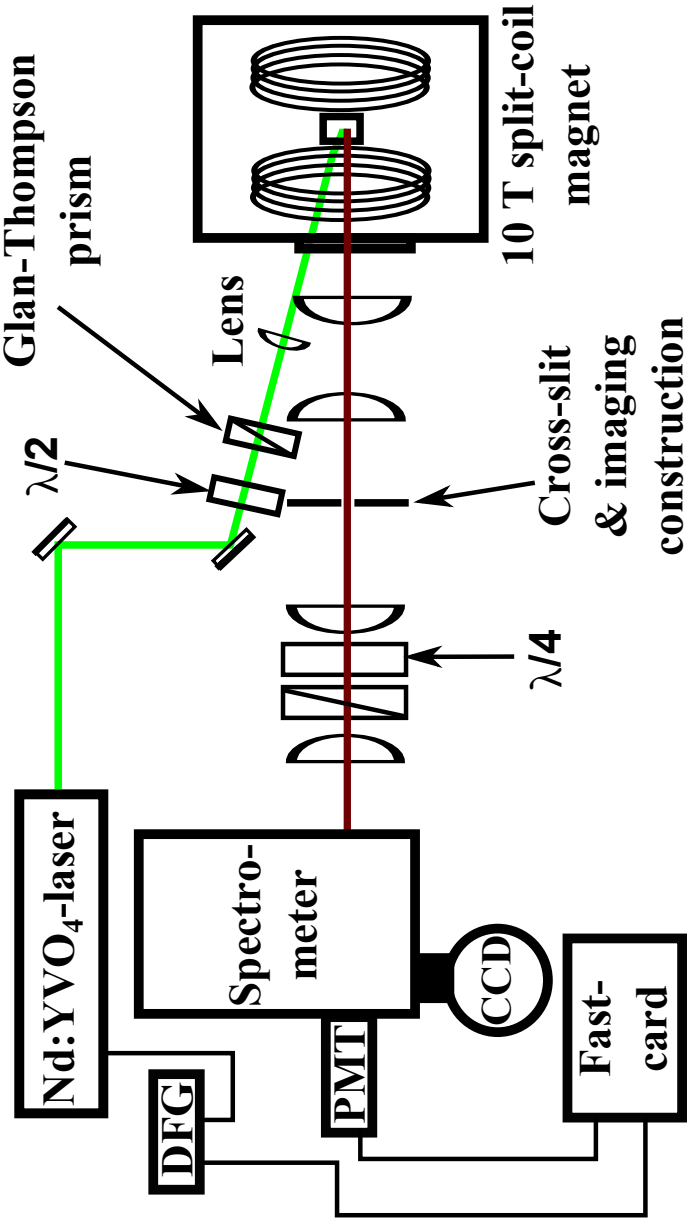

Figure 2-1: Experimental setup for time-integrated and time-resolved PL measurements. The sample is place in a 10 T split coil magnet cryostat regulating temperature and applied magnetic fields. The optical excitation source is represented by a pulsed Nd:YVO_4 laser, but can be exchanged with an optically pumped Ti:Sapphire laser, especially for resonant excitation measurements. Further optical elements: $\lambda/2$ - half-wave retardation plate, $\lambda/4$ - quater-wave retardation plate, Lens - achromatic glass lense with anti-reflection coating, Glan-Thompson prism - illustrated by diagonal crossed rectangle. Electronic devices: PMT - photomultiplier, CCD - charge-coupled device camera, DFG - digital function generator, Fast-card - Single pulse counting device. The spectrometer in the scheme has not been further specified, as both double- and triple-spectrometer have been used. The latter furthermore in different modes and under application of different number of stages.

a lens and the light collecting efficiency. As the lens was placed in its focal length to the sample, its emitted light is in the following transmitted as a parallel beam to a second identical lens in front of the spectrometer.
For the surveillance of the excitation area and the stability of the sample position, an imaging construction has been placed in the region between the collecting and focusing lens. The construction consisted of a lens focusing the beam on a two-dimensional cross-slit. By the use of a tilted mirror, the now sharp image of the sample can be observed through a microscope. Moreover, the cross-slit allowed to spatially resolve the signals coming from the sample, e.g. to choose from the parts of the samples position to emit its luminescence. With a removed tilted mirror and a second lens either in its focal length to the cross-slit, the beam can be transmitted further in the direction of the spectrometer. In the regime of parallel light propagation, a second combination of polarization optics is installed. This consists mainly of an additional Glan-Thompson prism with linear polarization direction perpendicular to the first prism, found in the excitation part of the setup. For unpolarized PL measurements, this prism is used to suppress any stray light coming from the laser. In polarization-resolved PL measurements, it allows the separation of right- and left-circularly polarized light, together with a quarter-wave retardation plate. The retardation plate in this combination transforms the circularly polarized light, depending on the direction of its fast-axis into horizontally or vertically polarized light, which is either transmitted or blocked by the Glan-Thompson prism.
The spectrometers used in the course of the measurements were either a triple-spectrometer (Princeton Instruments, TriVista 555) or a double-spectrometer (Jobin-Yvon, U1000). The triple-spectrometer can be driven both in an additive mode, where its focal length is three times longer (1.5 m) than in case of a single-monochromator (0.5 m) for measurements requiring high resolutions or in a subtractive mode. In the latter mode, the first two stages are used as an optical filter. The first two monochromator gratings are then tuned oppositely to each other, leading to a light dispersion in the first monochromator which is canceled in the second. The dispersive light coming from the first stage initially has to pass a slit before it is further proceeded in the second stage. By reducing the slit size, the spectral range, which is further transmitted through the spectrometer, can be controlled. In this way undesired spectral regimes, consisting for example laser stray-light, can be suppressed. The three gratings causing the dispersion of light in the spectrometer are mounted on a three-sided rotating stage, granting an easy exchange between gratings. The triple-spectrometer, which is built corresponding to the Czerny-Turner design, has further the advantage, that it offers the possibility to address its monochromator stages separately with fibers. This results in lower resolutions, but increases the signal-to-noise ratio [62].
The second spectrometer used, is a double-spectrometer in an asymmetric Czerny-Turner design. This device offers a two orders of magnitude higher stray-light suppression in comparison to the triple-spectrometer, so that a PL observations even closer to the excitation energy is provided. The holographic 1800 g/mm grating without blaze wavelength and the long focal length of 2 m enable an average reso-

lution of 10 μeV for slit sizes of 100 μm. The slit sizes can be increased/decreased further for an according decrease/increase of the spectral resolution. Such high resolutions, as provided by the double-spectrometer, have the disadvantage of low signal intensities and principally lower signal-to-noise ratios [63].
The conversion from light into electronic signals can be achieved by two detection devices, a GaAs-photomultiplier tube (PMT) or a charge-coupled device (CCD) camera composed of arrays of Si-photodiodes. The PMT is a single-channel detector with small noise levels, ideal for the observation of low-intensive signals. Furthermore, it allows, depending on the slit sizes of the used spectrometers, a detection of signals shifted by not more than 0.3 cm^{-1} (less than 40 μeV, value corresponds to usage of double-spectrometer U1000). The CCD-camera on the other hand, as a multi-channel detector, allows the immediate detection of complete spectra, drastically decreasing the measuring time.

2.2 Time-resolved photoluminescence

Time-resolved photoluminescence measurements are performed to determine carrier lifetimes or spin relaxation times. These require excitation sources significantly shorter than the corresponding decay curves [65]. In the setup shown in Fig. 2-1, this short excitation source is realized by a Neodym-doped yttriumorthovanadate (Nd:YVO_4) laser driven in its second (532 nm, 2.33 eV) or third harmonic (355 nm, 3.49 eV). The fundamental emission in the Nd^{3+}-ion is dominated by the ${}^4F_{\frac{3}{2}} \rightarrow {}^4I_{\frac{11}{2}}$ transition providing a wavelength of 1064 nm (1.165 eV). With ${}^4F_{\frac{3}{2}}$ being the upper energy level accumulating the majority of the pump energy and ${}^4I_{\frac{11}{2}}$ being the lower level. From this lower energy level a fast non-radiative relaxation occurs to the ${}^4I_{\frac{9}{2}}$ ground state [64]. The semiconductor laser is equipped with a Q-switch, enabling an intensive emission in the nanosecond timescale (5 ns) with repetition frequencies ranging from several tens of Hz to hundreds of kHz.
An alternative to the use of the Nd:YVO_4 laser, which has been built as a pulsing laser source producing short-time excitation pulses, is the chopping of continuous-wave laser emissions by optical or even mechanical devices. In the present case, the spectrally tunable Ti:Sapphire laser with continuous-wave emission has been modified by an acousto-optical modulator (AOM), not shown in Fig. 2-1. The excitation beam is transmitted through the modulator crystal, which needs to be transparent for the used wavelength. With the application of radio frequencies in the modulator crystal, periodic expansions and compressions are induced into the crystal, which locally change the diffractive index of the crystal. As a result, the excitation beam is scattered on the periodic modulation, which becomes noticeable as interferences behind the AOM following the Bragg reflection. The Bragg reflection cause the scattered beam to emerge out of the AOM under the angle Θ_n:

$$\sin(\Theta_n) = \frac{n\lambda}{2\Lambda}. \tag{2.1}$$

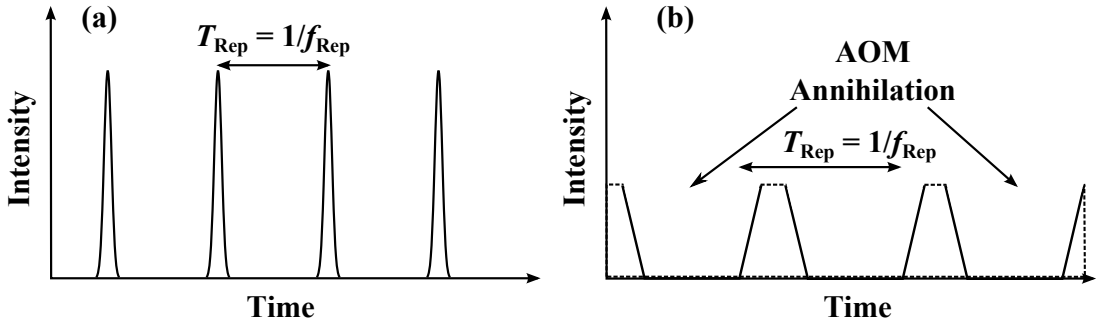

Figure 2-2: (a) Idealistic intensity propagation and shape scheme of a Q-switched Nd:YVO_4 laser. The pulses emitted from the pulsed laser source follow a Gaussian function. The pulse width of the used laser has approximately 5 ns, while the repetition frequency is $f_{\mathrm{Rep}} = 1$ kHz corresponding to a measuring period of $T_{\mathrm{Rep}} = 1$ ms. (b) Intensity modulation of a continuous-wave Ti:Sapphire laser controlled by an AOM. Noteworthy, is the significantly longer pulse width of 100 ns compared to case (a) with 5 ns. The reduced overall intensity is indicated by a reduced average intensity level.

Relevant for the emerging angle Θ_{n} are therein the wavelength of light λ and the wavelength of the radio frequency modulation Λ. The index n is here an integer number describing the number of the diffraction order. The higher orders of diffraction beginning with $n = 1$ can further be controlled by the temporal modulation of the radio frequency signal. This is achieved by the use of a digital function generator modulating the radio wave excitation in the crystal, effectively switching it on and off. The corresponding response-time of the AOM is about 100 ns with a rise times of 5 ns. This is at least one order of magnitude worse than the Q-switched Nd:YVO_4 laser. Moreover, the excitation power of the modulated light is significantly reduced, as the power is not intensified in the illuminating time domain. Instead, the continuously emitting wave is cut into small transmitting regimes and long dark regimes. Based on repetition frequencies of 1 kHz and transmitting regimes between 100 ns and 1 μs, the power of the modulated laser is reduced by factors between 10^{-4} to 10^{-3}.

The principle differences between the pulsed laser sources are depicted in Fig. 2-2. In the time-resolved measurements, the excitation powers are kept at extremely low levels in the range of μW/cm^2 and even nW/cm^2, so that low intensities are to be expected. To increase the number of events being observed, only the last stage of the triple-spectrometer has been used with completely opened entrance and exit slits. These proceedings on the one hand reduce the spectral resolution of the spectrometer noteworthy, but on the other hand drastically increase the signal intensity.

As a detection device the PMT has been used providing high signal-to-noise ratios with a temporal resolution of about 1 ns. In the photomultiplier, photons reaching the photocathode cause a corresponding number of electrons to be emitted. These are multiplied in the tube by cascading dynodes of increasing voltage causing secondary electron emission events. The exit signal of the PMT consists of a charge

proportional to the original number of photons collected at the photocathode. With a connected electronic device at the exit, the charges can be taken as a pulsed gain. By the use of a pre-amplifier and pulse-shaper with included analog-to-digital converter, these signals can be translated to voltage pulses and, after an amplification and pulse shaping also taking place in this device, are equal to TTL-signals. The pre-amplification system used (Scientific Instruments, F-100T) had the drawback, that it had a lower time-resolution than the PMT of only 3-4 ns, which can be seen as the temporal bottleneck of this setup.
Finally a counting system, the so-called fast-card (FAST, ComTec, P7889) orders the arriving signals into temporal bins. A single time-bin corresponds to a temporal width of 100 ps. By the coupling of a binary number of bins ($n = 2, 4, 8, 16, 32, ...$) into segments, the binwidth can be increased and the time-resolution be reduced. The synchronization between excitation and detection electronics is provided by a digital function generator (Tektronix, AFG3102). This device sends out start pulses to both, the laser source as well as the fast-card. The laser source starts, with some internal delay in the ns range, to emit laser pulses. The fast-card, initiated by the function generator by a START-signal, starts to count, increasing the corresponding bin-value in the process until the next start pulse re-starts this procedure. Any occurring STOP-signal at the second entrance to the fast-card will then be ordered into the according time bin and increase its associated integer number by 1. The same repetition frequency, which determines the number of emitted laser pulses also defines the number of internal cycles in the fast-card. Within one internal cycle initiated by a START-signal, several STOP-signals can be detected and be analyzed, although this condition is not advised for a single-photon counting technique. To prevent any overlap between incoming STOP-signals, the number of counts detected is kept below the number of cycles.
The delay between the START-signals and the first STOP-signals associated to PL event are governed firstly by the internal delay of the laser electronics and secondly by the time of flight of the photons, including the distance between the excitation source and the sample and the distance between the sample and the detector (3 m distance cause approximately 10 ns time delay).

2.3 Spin-flip Raman scattering spectroscopy

The spin-flip Raman scattering (SFRS) technique is based on the elastic scattering of incident light with carriers or complexes in the semiconductor crystal. The full scattering mechanism depends on the probability of separate processes including the excitation of carriers by the incident laser beam, a consequent spin relaxation process induced by an acoustic phonon scattering and finally the emission of a second photon with reduced energy. In conclusion the observation probability is relatively small. For that reason the corresponding setup has been optimized to increase the signal strength, depicted in Fig. 2-3. Two necessary conditions for the possible observation of SFRS signals can already be found in the excitation

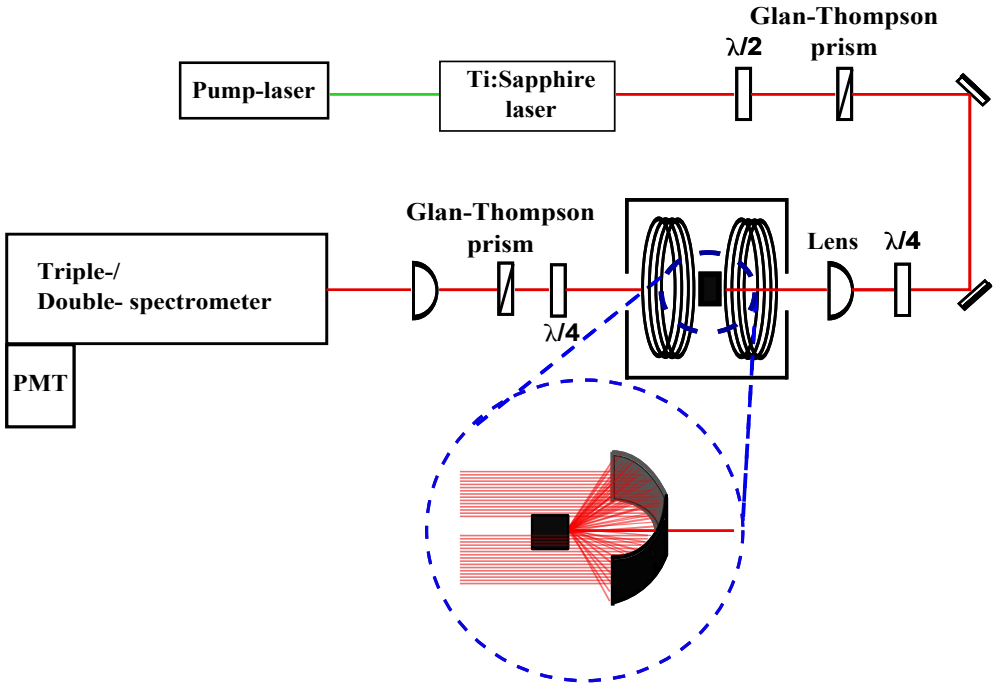

Figure 2-3: Intensity-optimized experimental setup, used for SFRS and optical orientation measurements. The enlargement, marked by the blue dashed area, shows the signal collection by the spherical mirror. The signal is transmitted as a parallel beam towards the spectrometer in the following. For efficient laser stray light suppression double- or triple-spectrometers are used.

source. This has to be able to tune the energies of the emitted photons, so that a resonance conditions with the band gap energies of the semiconductor nanostructures is fulfilled. Based on the structure of interest, this band gap energies can vary significantly. The second requirement necessary for the observation of SFRS signals is a small bandwidth of the excitation energies. As the SFRS signals will later be seen as an addition to the resonant PL in the form of a small replica of the laser line, the measurements greatly benefit from a sharp excitation laser, that is not causing any broadening of the SFRS signals.
Furthermore, the small intensities of the SFRS signals require an intensity-optimized experimental setup. Instead of a telescopic imaging system, seen before in Fig. 2-1, a setup is used following Fig. 2-3. As shown by the enlarged image of the interior of the cryostat, marked by the blue dashed lines, a spherical mirror collects all optical signals coming from the sample and sends them as a parallel beam out of the cryostat. A small hole in the midth of the mirror enables the previous excitation by optical means. As depicted in the figure, the transmitted signals are partially blocked by the sample, as the propagation of the parallel beam is hindered, depending on the size of the sample. Additionally, the sample can be mounted on sample holders with different angles between their surface normal and the magnetic field direction. Based of the plane installation of the sample on the holders surface, measurements of the angle dependencies between the sample

growth direction and the magnetic field are rendered possible.
The parallel beam containing PL and SFRS signals is in the following focused on the entrance slits of a double- or triple-spectrometer and detected by a GaAs PMT. The use of these special kinds of spectrometers is necessary, as the SFRS signals are in very close proximity to the laserline (hundreds of μeV), which requires to be efficiently suppressed for the observation.
Additionally depicted in the experimental setup are polarization optics, especially including quarter wave retardation plates ($\lambda/4$). As has been explained above, the combination of a $\lambda/4$ and a Glan-Thompson prism placed in the parallel regime of the detection part allows the separate detection of circularly polarized spectra. The quarter wave retardation plate placed in the excitation beam on the other hand, enables in fullfillment of the optical selection rules to optically excite single exciton spin states. These are in presence of external magnetic fields already split, and can be directly addressed by the exact excitation energies. The additionally circularly polarized light on the other hand allows in the SRFS experiments to excite single spin states more efficiently.
Even without the application of external magnetic fields, necessary for the SFRS measurements, the excitation of single spin states by circularly polarized light is profitably. The population differences caused by optically induced spin states are described by the optical orientation degree, which requires the detection of circularly polarized PL in co- and cross-polarized situations for both circular polarization directions.

Chapter 3

Optical properties of (In,Al)As quantum dots

In recent years semiconductor QDs have succeeded to perform the step from sample structures in fundamental research, with the aim to implement the spin state as a controllable size, to real device related applications, especially in the role of efficient light emitters. As the original aim has been proven to be difficult to fulfill and control reliably, new concepts for the further development of these structures had to be introduced. In the scope of the last years, the idea of a combining concept has been developed. QDs on the one hand have naturally an increased exciton recombination time, and further to that significantly longer spin relaxation times. On the other hand, classical indirect semiconductors show additionally increased exciton lifetimes, while their spin-orbit interaction is greatly reduced, making spin states more stable and longer-living. The combining concept therefore aims toward an indirect semiconductor with the additional limitations of a zero-dimensional structure. Based on this concept, the indirect (In,Al)As/AlAs QDs have been constructed, possessing a type I band alignment but having an indirect band gap in the momentum space.
To give an introduction and overview about the electronic and optical properties of (In,Al)As self-assembled QD, the first chapter of the experimental results give an insight into the bright exciton ground states. The dependencies influencing the emission energies will be analyzed in detail to develop a fundamental understanding as a basis for the later chapters, which present more sophisticated techniques and properties of the indirect QDs. Exciton ground states correlated to the QDs will be analyzed by comparison of four individual samples, denoted as S1-S4, whose growth and size characteristics are given within the text. For the visualization of the ground state energy dispersion, selective excitation measurements will be performed, leading to the additional display of higher energy states. The exact analysis and interpretation of its possible origins is proceeded in the second subsection. In these measurements a sample, denoted #2890, is used, as it has proven to be one of the most efficient light emitting samples. The sample consists of self-assembled (In,Al)As QDs in an AlAs matrix grown by MBE on a

(001)-orientated GaAs substrate. The sample has 20 layers of intentionally undoped (In,Al)As QDs with a fraction of 30 % In, sandwiched between 50-nm-thick layers of AlAs. The density of QDs is about $3 \cdot 10^{10}$ cm^{-2}. The dots have a lens shape with a ratio between height and in-plane diameter ranging from 3:1 to 5:1. In Table 3-1, the fundamental sample characteristics are listed for the comparison with alternative sample structures. As the first two sections mostly concentrate on photoluminescence (PL) features in the time-integrated regime, the third one is devoted to the time-resolved characteristics, being the prominent feature of indirect semiconductors and QDs, respectively. In this context, the exciton lifetimes will be determined and a theoretical approach for the descriptions of the extended and non-exponential decays will be developed.

3.1 Basic optical properties

In order to give an overview about the complex electronic structure being present in self-assembled QDs, a photoluminescence (PL) spectrum has been proven to be useful. Its signals represent the most radiative exciton ground state transitions observable in semiconductors. For that purpose, in Fig. 3-1 the PL of the undoped sample #2890 under above-barrier excitation with photon energies of 3.49 eV at low temperature of $T = 5$ K is shown in a wide spectral range. The PL spectrum consists of four characteristic signals. The highest-energy signal at 2.02 eV stems from the so-called (In,Al)As wetting-layer, which is basically a narrow layer of two to three monolayer thickness [66]. On this layer the QDs are formed under great stress based on the Stranski-Krastanov growth method. The PL emission energy of the QDs is centered around 1.75 eV with a full width at half maximum (FWHM) of 173 meV. The origin of this PL is attributed to the radiative recombination of electron-hole pairs trapped in the same QDs, which emit photons of characteristic energy in the process of their annihilation. The PL line of the QDs in Fig. 3-1 is shown in red and represents the large distribution of QDs with different characteristics influencing the emission energy of excitonic transitions.
The most prominent characteristics responsible for the exact emission energy are:

- **Composition of QD material**. The emission energy of binary compound semiconductors can be easily varied, if a fraction of one material component is replaced by another material. In QDs, the replacing material typically stems from the surrounding matrix, leading to a notation similar to $(In_x,Al_{x-1})As/AlAs$ where x is the fraction of InAs.

- **QD size**. The confinement potential of self-assembled QDs can range several hundreds of milli-electronvolts, thus shifting the emission energy.

- **Shape of QDs**. The shape of the QDs can reduce the symmetry of the carrier potentials with regard to the different directions of the crystal. It has an impact on the electronic properties.

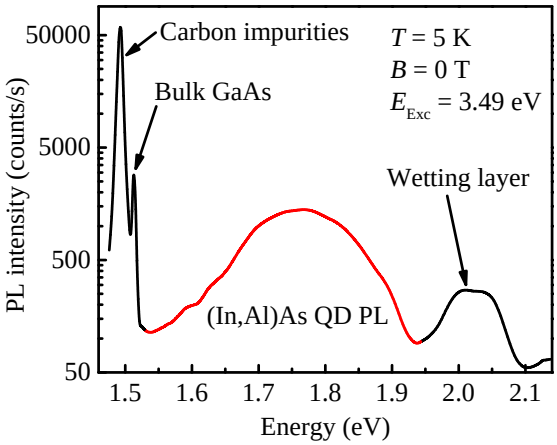

Figure 3-1: PL spectrum of sample #2890 in half-logarithmic representation. The above-barrier excited ($E_{\mathrm{Exc}} = 3.49$ eV) PL signals from the self-assembled (In,Al)As/AlAs QD ensemble taken at $T = 5$ K in absence of external magnetic field have been measured. In the presented spetrum, the signals stemming directly from the QD PL are demonstrated in red, while the black parts of the graph represent all other signals not directly correlated to electron-hole pairs trapped in QDs.

Additionally, in the spectra two signals can be seen, which are not related to the QD layers. The first one is detected at 1.51 eV and corresponds to the GaAs bulk exciton PL. It is attributed to a 200-μm-thick GaAs substrate on which the structures have been grown. The second feature at 1.49 eV stems from impurities mostly based on carbon in GaAs, which have been brought into the system during the growing process of the buffer layer likewise grown by MBE [67, 68].
The use of high excitation energies for PL measurements is typically accompanied by a high absorption in the overall structure and correspondingly followed by the creation of a large amount of carriers in the system already at moderate excitation powers. Shortly after the excitation, the hot carriers relax by various non-radiative relaxation processes into matrix and QD states, where they thermalize to the lowest-energy states. Therefore, this method is especially useful for the observation of exciton ground states in all possible nanostructures. By use of high excitation powers, state filling occurs, which allows to determine excited exciton states separately from the ground states [69].

First evaluation for the influencing strength of the three above-mentioned characteristics is achieved by a comparative study of four samples with slightly different properties. They are denoted as S1-S4 [18]. In Table 3-1 relevant growth and sample characteristics are listed. The samples have been grown by the Stranski-Krastanov growth method causing sharp interface borders. The first parameter T_{g} describes the temperature of the substrate during the growth process with the interruption time t_{gi}. The samples S3 and S4 have been additionally annealed at the temperature T_{an} after the growth of the QDs. Under these growing and annealing conditions, each ensemble of QDs develops the characteristic values $D_{\mathrm{S}}, D_{\mathrm{AV}}$ and D_{L} describing the lateral QD size distribution. Here, D_{AV} is the average diameter of the QDs and D_{S} as well as D_{L} the smaller and larger half-width values of

Sample	T_g/t_{gi} °C/s	T_{an} °C	D_S nm	D_{AV} nm	D_L nm	QDs density 10^{10} cm^{-2}	S_D %	Average fraction of InAs in QDs
S1	450/10	-	4.3	5.50 ± 0.21	7	10	40	0.99
S2	460/60	-	9.0	13.8 ± 0.22	17	8.5	60	0.80
S3	510/60	700	15	18.3 ± 0.15	22	4.2	52	0.47
S4	460/60	800	12	19.6 ± 0.16	28	8.5	75	0.35
#2890	525/30	-		≈ 12.0		3.0		0.30
#2104	515/40	-		≈ 12.0		3.7		0.25

Table 3-1: Growth and sample characteristics for the samples S1-S4. Temperature and interruption times used within the growth procedure are included in the second column denoted by T_g/t_{gi}. For the samples S3 and S4 an additional post-growth annealing has been performed at temperatures of 700 and 800°C, respectively. Under these conditions the four ensembles of QDs form typical size distributions, which are described by the size values of D_S, D_{AV} and D_L. In Fig. 3-2(S3), these parameters are described as the small, average and large size distribution values referring to a Gaussian distribution function. The QD density is a direct consequence of the previous growing conditions and the low value allows one to neglect any coupling or transfer of carriers between the QDs [70]. The size dispersion, which has been calculated by $S_D = 100\% \times (D_L - D_S)/D_{AV}$ describes the width of the size distribution. The last column includes information about the QD composition, which is highly related to the exciton emission energy. The sample #2890 and #2104 are additionally described in the introduction of each chapter, they are used in. The sample #2104 differs further by a doping procedure filling each QD averagely with one resident electron.

the size distribution. This provides a definition for the size dispersion following $S_D = 100\ \% \times (D_L - D_S)/D_{AV}$, which represents a more relevant value for characterizing the size distribution than the half-width values alone.
By using the transmission electron microscopy (TEM) system JEM-4000EX at acceleration voltages of 250 keV, these values have been determined for the samples S1 to S4 in terms of a statistical investigation, shown in Fig. 3-2. These measurements have been performed in the department of semiconductor physics in Novosibirsk. For the non-annealed structure S1 the most slender size dispersion has been identified with $S_D = 40\ \%$ around an average QD diameter of 5.5 nm. The other three samples have QDs with larger diameters and a stronger size dispersion. The samples S2 and S4 have been grown under identical conditions besides the post-grown annealing in the case of sample S4. The annealing in the case of sample S4 has been performed at 800°C, thus leading to increases in the average size diameter from 13.8 to 19.6 nm and in the size dispersion from 60 to 75 %. The changes caused by the annealing are a result of interdiffusion of material between the InAs QDs and the surrounding AlAs matrix. This is also evidenced by the different InAs fraction in the QDs after the annealing process, which is decreased from 80 to 35 %. In the transition area between the QDs and matrix, the heterointerface, the annealing therefore causes the development of an $In_xAl_{x-1}As$ layer. The

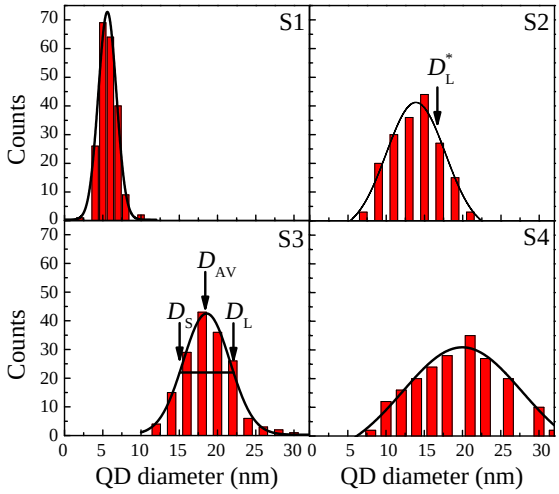

Figure 3-2: QD size distribution in the samples S1-S4 determined by TEM analysis. In the panel dedicated to sample S3, the characteristic size values D_S, D_{AV} and D_L are exemplarily integrated. They are used for the description of the QD size distribution in the ensemble of QDs.

expansion of this layer is controlled by both the temperature and duration of the annealing process. This allows one to define a qualitative, but nevertheless important feature: The sharpness of the heterointerface between QDs and matrix. It can be defined by the distance between the areas of pure InAs in the QDs and pure AlAs in the matrix or by the size of the mixed $In_xAl_{x-1}As$ layer, respectively. A sharp heterointerface corresponds to an immediate succession from QDs to matrix, while a smooth heterointerface is accompanied by an $In_xAl_{x-1}As$ layer with an increasing AlAs fraction in the direction of the matrix. The samples S1-S4 therefore provide a wide variety of QDs with different sizes and heterointerface sharpnesses. In addition to the information taken from the TEM measurements, granting an insight into geometrical features, PL measurements are used to study the excitonic ground states of the QDs. A combined analysis allows one to make statements about the impact of geometrical changes on the electronic structure. In Fig. 3-3 the above-barrier excited PL of all four samples is depicted. The measurements have been performed at a temperature of 5 K, and a continuous-wave excitation energy $E_{\mathrm{Exc}} = 3.81$ eV with a power density of 10 W/cm^2, provided by a HeCd laser, has been used. The spectra show two separate PL features stemming from direct (low-energy emission) as well as indirect QDs (high-energy emission). The emission, in turn, originates from direct exciton ground states in the Γ-point solely or indirect ones with an electron in one of the X-valleys and one heavy-hole in the Γ-point. In presumption, the shaded area in the graph represents the area of intermixing between electronic Γ- and X-states, where both conduction band levels have equal or almost equal energies. The average value of the transition energy from direct to indirect QDs will be given later in this chapter. The PL emissions of all four samples differ significantly, with indirect PL maxima ranging from 1.705 eV for S2 to 1.854 eV for S4. Also the shape of the PL lines varies strongly. Here, especially the samples S2 and S3 show additional features on the

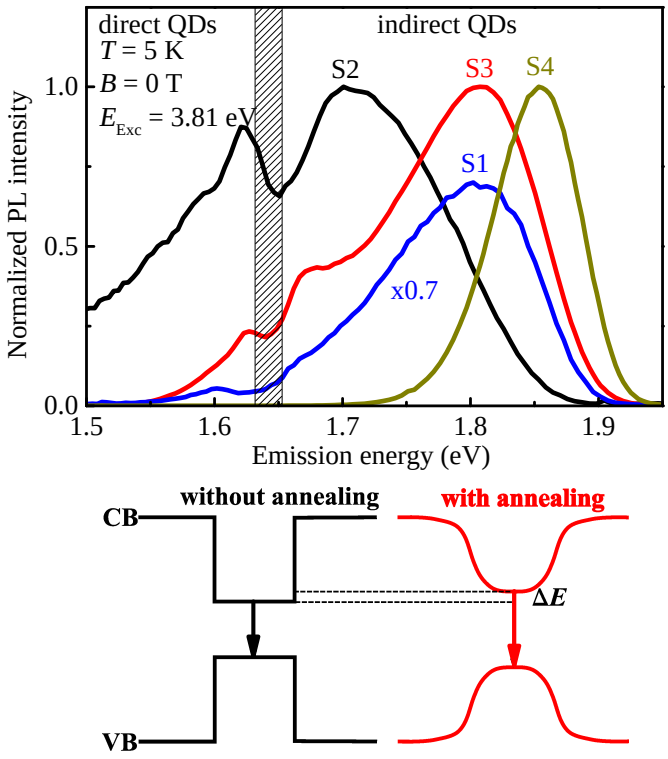

Figure 3-3: Above-barrier excited PL spectra for the samples S1-S4; $E_{\mathrm{Exc}} = 3.81$ eV, $T = 5$ K. The shaded region roughly separates the regimes of indirect and direct band gap QDs. For a clear arrangement the normalized PL spectrum of sample S1 has been multiplied with a factor of 0.7. The schematic below the diagram describes the influence of the post-grown annealing procedure on the conduction (CB) and valence band (VB) edges. Noteworthy, are the smoothed QD potential interfaces and the blue-shift of the band-gap energy marked by ΔE for the CB edge.

low-energy side. They hint at transitions not representing the size distribution of the QDs.

In relation to the information gathered from the TEM measurements, the comparison of the PL spectra of all four samples allows some statements on the dependencies dominating the QD structures. The samples S1 and S2, which have not undergone any post-growth annealing, have a high fraction of InAs in their QDs. They show a significant shift of their PL maxima in respect to each other. The emission from sample S1 is centered around 1.805 eV, while for S2 the PL maximum is red-shifted by more than one hundred meV, centering at 1.704 eV. This behavior can be explained by the different size distributions presented in Fig. 3-2. It can be seen in the figure that the difference in the average diameter of the QDs leads to the red-shifted emission. Additionally, the differences in the full width at half maximum (FWHM) of the QDs size distributions are in good agreement with the FWHM values for the PL emissions. Giving specific values, the size dispersions of S1 and S2 are 40 and 60 % causing a PL FWHM of 115 and 195 meV, respectively. The emission of sample S1 reaches into the direct recombination region, thus explaining the second PL feature at 1.622 eV; it is caused by direct excitons in momentum space. They have a relative low density of states at this energy, but

recombine more efficiently than the indirect ones, resulting in the comparatively high intensity.
The changes caused by the post-growth annealing can be also seen in the comparison of sample S2 with sample S4. The latter actually has the same structure as S2, except that S4 has been annealed under a high annealing temperature of 800°C. Due to the annealing, the PL emission shifts drastically to higher energies from 1.704 eV in case of sample S2 to 1.855 eV for S4. This difference cannot be explained by the simultaneous increase of the size distribution. As mentioned before, the changes in the emission can be caused by three major aspects; QD size, its composition and their shape. In case of the S1-S2 comparison, the differences in the size are sufficient to explain the red-shift, while the slight changes in composition inside the QDs are negligible. Therefore, the blue-shift between the samples S2 and S4 cannot be described by a weaker confinement potential, but has to be taken as the result of the significant changes in the fraction of InAs in the QDs. Prior calculations by T. S. Shamirzaev et al. evidence this assumption [15]. In their work they calculated the transition energies of confined excitons in (In,Al)As QDs as a function of the InAs fraction. With the knowledge of both the emission maximum as well as the QD size, one can approximate the fraction of InAs in the QDs, as it has been presented in Table 3-1.
The scheme in the lower part of Fig. 3-3 describes the effect of strong annealing on the energies of the valence and conduction band edges. A renormalization of the bands takes place, i.e., the energy levels of the QD conduction and valence bands become equal to the AlAs matrix bands based on the interdiffusion of material from the matrix into the QDs and vice versa. This process on the one hand results in a blue-shift of the QD emission energies, and on the other hand smoothes the sharp transition energies between matrix and QD. The blue-shift observed in the PL spectra is depicted by the energy shift ΔE shown in the scheme only for the conduction band, but influences the valence band additionally forming different energy shifts. In [15], the influence of QD size and composition on the energy levels of Γ-point electrons and holes, as well as L- and X-valley electrons separated into those confined in the plane of the QDs (X_{xy}-valleys) and along the QDs height (X_z-valleys) is demonstrated.* In Fig. 3-4, the calculated energy levels of all relevant carrier states are depicted as a function of the QD size using the effective mass approach. In the calculation, a constant QD composition of 70 % InAs and lens-shaped QDs with an aspect ratio of 4:1 (in-plane diameter:height) is assumed. The band offsets for the X- and Γ-electrons and holes can be found in Ref. [15], which are partially taken from [71] and [72]. The six degenerated X-valleys for a bulk (In,Al)As semiconductor are transformed to the QD case by considering non-equal strain and confinement potential along the main axis, as a result of the reduced symmetry. Four of the X-valleys, which are aligned along the in-plane axes (100) and (010) of the QDs are degenerated. While the additional valleys along (001) or growth axis are influenced stronger by the high confinement

*The calculations have been performed by the simulation tool NEXTNANO³.

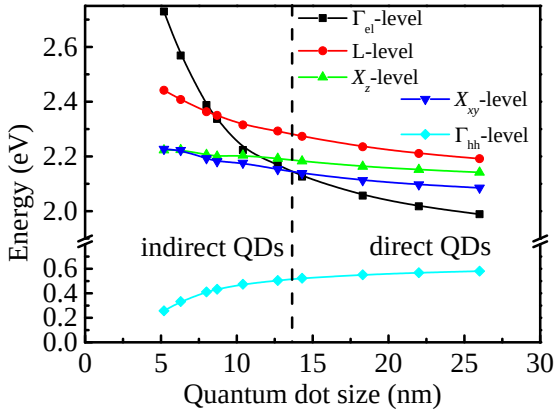

Figure 3-4: Calculated electron and heavy-hole energies in dependence on the QD size. The energy shifts of electron and hole states at significant symmetry points are described. Lens-shaped QDs with an aspect ratio of 4:1 and an average fraction of InAs of 30 % are considered. Strong shifts of the Γ-valley electrons (Γ_{el}) in comparison to the X-valley states result in the crossing of direct and indirect levels for QDs of approximately 13.5 nm in diameter. The non-uniform confinement of the lens-shaped QDs requires a separated approach for the in-plane (xy-plane) X-valleys and those aligned along the z-direction. In case of the eight-folded L-valleys, this separation is more complex, as the L-valleys do not correspond to the geometrical dimensions of the QDs. Light-hole states, which are shifted from the heavy-hole states (Γ_{hh}) by at least 30 meV for all QD sizes, are not shown.

in this direction and require an isolated approach. The energy levels are presented in absolute values. Transition values can be taken as the difference between electronic levels with the Γ-heavy-hole levels. Not shown in the graph are light-hole values which are situated approximately 30 meV below the heavy-hole levels. For InAs QDs exceeding a size of 13.5 nm, the lowest electronic energy state can be found at the Γ-point, as in the case of its bulk counterpart. But, it can be shifted drastically due to the confinement potential by several hundreds of meV. This strong shift is elevated by the low effective mass for electrons at the Γ-point of about $m_{\mathrm{eff},\Gamma} = 0.023 m_0$ [72, 73]. In contrast to this, the X-valley electron states are characterized by a significantly higher effective mass value $m_{\mathrm{eff,l}} = 0.16 m_0$ for the longitudinal and even $m_{\mathrm{eff,t}} = 1.13 m_0$ for the transversal (in-plane) direction resulting in a lower blue-shift with decreasing QD size. As can be easily seen for quantum dot sizes below 13.5 nm, the Γ-valley energy level (black squares and solid black line) is raised above the X-valley levels making the QDs to indirect band gap semiconductor structures. The lowest energy states in the conduction band are associated to the in-plane X_{xy}-valleys and in the valence band they belong to the heavy-holes in the Γ-valley. Hence, the exciton ground state becomes optically forbidden.

When photons selectively excite carriers in the regime of the indirect QDs, they initially elevate electrons into the short-living Γ-state. It is an excited state, accordingly, electrons can either recombine with heavy-holes or relax within the lifetime of the direct exciton into the lower-lying X_{xy}-states. A recombination from this state is accompanied by an energy shift in comparison to the excitation energy and

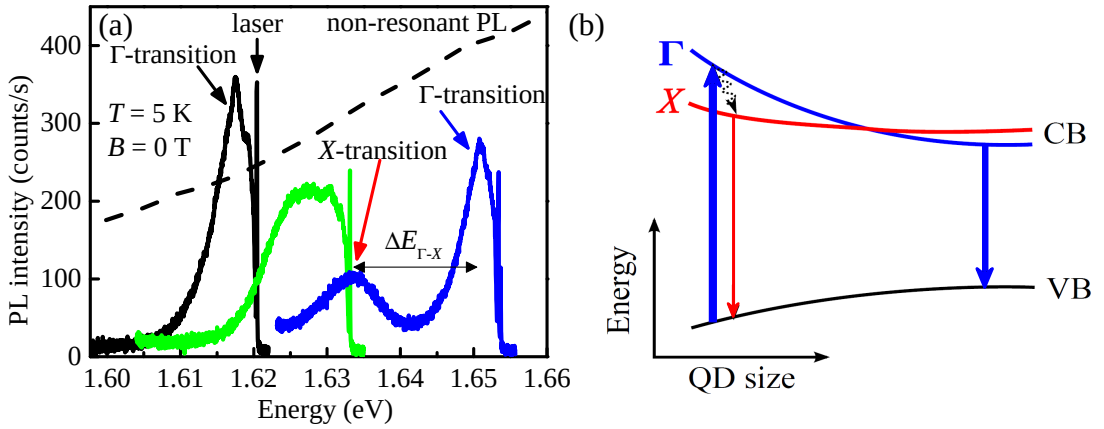

Figure 3-5: (a) Selectively excited PL spectra at three excitation energies. At a low excitation energy, $E_{\mathrm{Exc}} = 1.620$ eV, as shown by the black line, solely direct QDs are excited, emitting light at a constant offset from the excitation energy. With increasing excitation energies starting approximately at $E_{\mathrm{Exc}} = 1.633$ eV (green graph), additionally to the direct emission, the indirect QDs start to give rise to a broader PL feature. The blue graph finally presents the separated PL emissions excited at an elevated excitation energy of 1.653 eV. (b) Band scheme distinguishing direct (right-side) and indirect transitions. As absorptions are only allowed between Γ-states (blue arrows), a relaxation takes place (waved arrow) transferring electrons to the X-valley states followed by a recombination (red arrow). The horizontal differences of blue and red arrows are conditioned by graphical limitations and have no physical origin.

the direct recombination energy, respectively. A selective and accordingly resonant excitation of the QDs allows, in contrast to the above-barrier excited PL, the visualization of single exciton energy levels, as can be seen in Fig. 3-5(a). For the selective excitation measurements the undoped sample #2890 is used; its PL over a broad spectral range is shown in Fig. 3-1. To prevent temperature broadening of either emission or absorption lines the sample was cooled down to a temperature of 5 K. The resonant excitation had a narrow energy width of < 1 μeV (~ 100 MHz) stemming from a Ti:Sapphire laser; it solely affects QDs whose size and composition cause an absorption equal to the excitation. For low excitation energies equal or below to $E_{\mathrm{Exc}} = 1.62$ eV (see black line), a resonant PL feature close to the excitation laser line becomes visible stemming from the direct Γ-transition. The width of this line exceeds 6 meV signifying the excitation of several QDs at the same time instead of a single QD, which would emit light with a linewidth of only 0.1 meV, typically for QDs grown by the Stranski-Krastanov growth method [74]. With increasing excitation energy above 1.63 eV, a second PL feature becomes visible, see green and blue colored lines in Fig. 3-5(a). It is attributed to the indirect transition of X_{xy}-valley electrons and Γ-valley heavy-holes. The indirect PL feature is red-shifted with increasing excitation energy, representing the energy difference $\Delta E_{\Gamma-X}$ between the Γ- and X-states. In contrast to the indirect PL, the direct resonant transition follows the excitation energy with a nearly constant offset of 3-4 meV. For a better overview, the non-resonant PL is included into the figure as a dashed line. It shows the position of the Γ-X-transition being at the

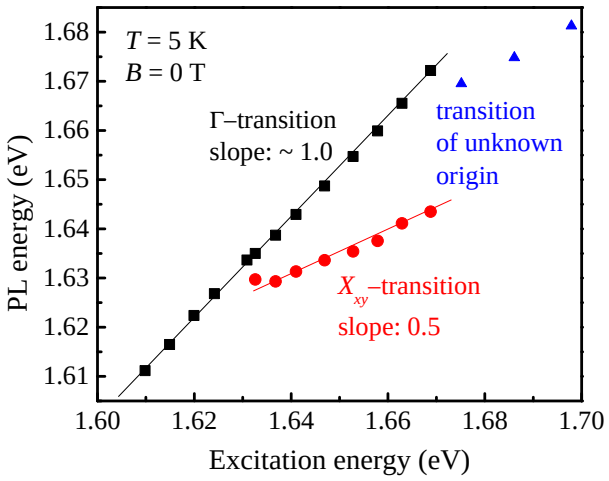

Figure 3-6: Transition energies of direct and indirect excitons observed under selective excitation. Direct excitons with Γ-valley electrons and heavy-holes are illustrated by black squares. The solid black line represents the linear fit, demonstrating the linear increase of the direct exciton transition with increasing excitation energies. Indirect exciton transitions, marked by red points, originate from eletrons in the X_{xy}-valleys and heavy-holes left in the Γ-point. They emit lower in energy compared to the direct transitions and shift linearly with excitation energies with a slope of 0.52. Additional signals, which are represented by blue triangles, appear with high excitation energies blue-shifted to the indirect X_{xy}-valley transitions.

low-energy side of the PL for this sample where the PL intensity is still in the rising regime.

The scheme in Fig. 3-5(b) visualizes the energy level differences for the direct and indirect QDs. The determination of the distinct features in the spectra in dependence on the excitation energy results in a scheme of transition energies following Fig. 3-6. Illustrated by black squares are the PL peak energies of the completely direct Γ-transitions succeeding the excitation with a small, constant offset, having consequently a slope of approximately one. On the contrary to this direct transition branch, the signals stemming from Γ-valley heavy-holes and X_{xy}-valley electrons are shown by red points. They start to appear at an excitation energy of about 1.63 eV. At that points, simultaneously the Γ-transitions intensity is reduced. In this representation the slope of the indirect branch can be calculated to 0.52 and is consistent with the calculations performed for Fig. 3-4: Taking the calculated Γ-transitions as the quasi-resonant excitation energy to determine the shift of the corresponding X_{xy}-valley energies, a slope of 0.54 for the theoretical indirect branch is evaluated. The shift of the indirect transition, which seems to have a linear slope for decreasing QD size, suggests that a change in the QD composition can be neglected in comparison to the changes caused by the confinement. This assumption is enforced by the comparison with the calculations, which also demonstrate a linear slope for a wide range in the QD size dependence.

Additionally, similar results have been gathered by Dawson et al., who have analyzed InAs/AlAs quantum dots and observed linearly shifted PL features with a slope of 0.55 with regard to the excitation energy [12]. In contrast to our assump-

tions, they have interpreted their results as the indirect transitions in both real- and momentum-space. The consequent separation of carriers would be accompanied by a blue-shift for higher excitation powers in the PL maxima according to the optical Stark effect. Shamirzaev et al. studied this possibility and were able to exclude it, proving for the (In,Al)As QDs to have a type I band structure and being indirect only in the momentum-space [14].
Additionally to the signals stemming from indirect X_{xy}-valley transitions, highly intensive PL features start to appear at excitation energies exceeding 1.675 eV. These features are blue-shifted to the indirect signals by 26 meV and seem to have the same slope with the excitation energy dependence. The determination of the origin of this PL feature is ab-initio unclear and will be the aim of the following section.

3.2 Identification of additional PL spectrum features under resonant excitation

This section is devoted to the identification of the additional PL feature, seen in the resonant excitation measurements. As has been shown in Fig. 3-6 in the previous section, an additional PL feature starts to appear at higher excitation energies, starting at $E_{\mathrm{Exc}} = 1.675$ eV being approximately 26 meV blue-shifted to the signals which have been identified as the indirect X_{xy}-valley transitions.
In order to determine the origin of the higher-energy shifted PL feature, which has been shown in Fig. 3-6 by the blue triangles, series of measurements have been performed. As the (In,Al)As QD structure consists of an ensemble of QDs with a large size distribution, the distinct PL feature can only be addressed by selective excitations. For that purpose, the sample structure has been excited by spectrally sharp laser light with energies ranging from 1.625 to 1.937 eV.[†] Instead of the previously illustrated absolute transition energies, the energy shifts in respect to the excitation energies are illustrated in Fig. 3-7, calculated by $\Delta E = E_{\mathrm{Exc}} - E_{\mathrm{Det}}$.
As seen before, the resonant emission (shown by black squares) stemming from the direct exciton is shifted by 3-4 meV for low-energy excitations. This Stokes shift is known for small QDs, excited by a resonant excitation source [75], and is occasionally taken as the difference between bright and dark exciton states δ_0. The value observed, on the contrary, exceeds δ_0-values known for InAs QDs by one order of magnitude [36, 35], so that some additional process (like interface scattering) seems to be responsible. For higher excitation energies coinciding with the emergence of the second PL feature, the direct Γ-valley exciton blue-shifts until it becomes completely resonant with the excitation line, enabling only the

[†]Additional to the range of excitation used before, provided by a Ti:Sapphire laser, a second range of excitation was used coming from a dye laser with DCM as a lasing material. The gap ranging from 1.720 to 1.797 eV represents the absent overlap in the emission energies of both excitation sources.

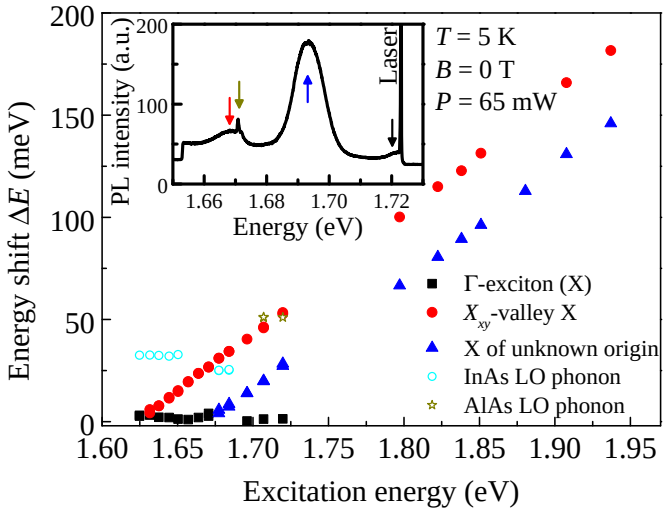

Figure 3-7: Energy shifts of all observed transitions in dependence on the excitation energy. In accordance to Fig. 3-6, the transitions of direct Γ-excitons (black squares), indirect X_{xy}-excitons (red points) and those of formally unknown origin (blue triangles) are included. Additionally, the observation of Raman lines, denoted to InAs (cyan circles) and AlAs LO phonons (olive stars), has been achieved. In the inset a typical selectively excited PL spectrum is shown, marking the distinct PL and Raman features with corresponding colored arrows. Not seen in the spectrum is the InAs LO phonon line.

observation of the low-energy PL shoulder. In this region, the direct PL intensity is strongly reduced and requires high-power excitation for its observation.
At elevated excitation energies, beginning at $E_{\mathrm{Exc}} = 1.675$ eV, the second PL feature, shown in the figure as blue triangles, appears close to the laser line. Its energy shifts increase linearly with increasing excitation energies equal to the X_{xy}-valley exciton, represented as red points. The slope of this additional branch is similar to the X_{xy}-valley transition one and can be calculated to 0.55. As an example spectrum, the inset in Fig 3-7(a) shows the PL emission at an excitation energy of 1.722 eV. The colored arrows represent the distinct features, whose energy shifts, in respect to the excitation, are depicted in the main part of Fig. 3-7. Under this excitation condition, the intensity of the PL feature of unknown origin (blue arrow) is comparatively high in comparison to the exciton ground state (red arrow). In addition to the PL features, a sharp line can be observed, marked by the olive arrow, which appears at an energy shift of 50 meV and only in resonance with the X_{xy}-valley PL. This signal corresponds to a Raman line of the longitudinal optical (LO) phonon typical for an AlAs bulk crystal [79]. The incident photons scatter inelastically in this process with the crystal and cause the emission of a LO phonon, reducing the scattered lights energy by $E_{\mathrm{Det}} = E_{\mathrm{Exc}} - \hbar\Omega_{\mathrm{LO}}$. Not seen in the exemplary spectrum, presented in the inset of Fig. 3-7, is the appearance of the InAs related LO phonon Raman line, shifted by 32 meV to the excitation line and represented by cyan circles in the main part of the figure. With the increasing shift of the higher intensive X_{xy}-exciton PL into the range of the low intensity Raman line, the PL completely covers the Raman line, making the ob-

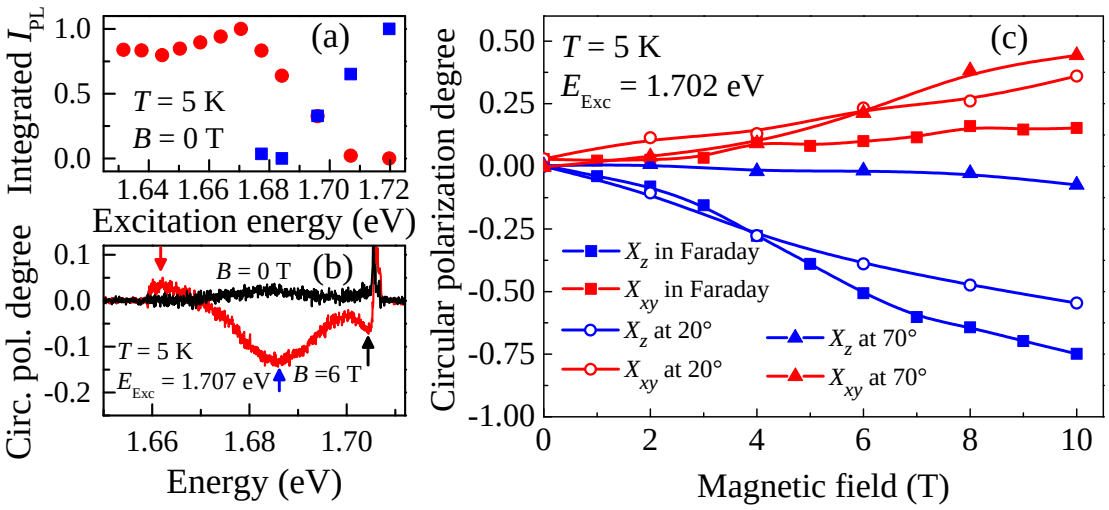

Figure 3-8: (a) Normalized, integrated intensities of the two indirect PL features with increasing excitation energies. At low excitation energies, the X_{xy}-valley exciton has a relatively constant intensity. With the emergence of the second PL feature, the X_{xy}-valley exciton intensity decreases as fast as the second feature´s intensity rises. (b) Magnetic field induced circular polarization degree of the selectively excited PL at an applied magnetic field of $B = 6$ T. Opposite polarization directions are observed for the two distinct features, speaking for exciton g-factors with opposite sign. For comparison, the same measurement without an applied field is included by the black graph, proving the magnetic field as the origin of the polarization. (c) Magnetic field dependence of the circular polarization degree for both PL features. With the modification of the geometry angle Θ, describing the orientation of the sample growth axis in relation to the external magnetic field, the possible inhomogeneity of exciton g-factors can be observed. The magnetic field dependence is examined at three angles ranging from zero (Faraday geometry) over $\Theta = 20°$ up to $\Theta = 70°$ which is close to the Voigt geometry.

servation in this range impossible. Subsequent to the overlapping, the Raman line re-emerges with a different energy shift of 25.5 meV in comparison to the previous 32 meV. The change of the InAs LO phonon energies speaks for a stretching of the (In,Al)As crystal, reducing the corresponding phonon energies. With the emergence of the second large PL feature at $E_{\mathrm{Exc}} = 1.677$ eV, the intensities of both the X_{xy}-valley exciton and that of the Γ-transition are rapidly reduced. Moreover, the Γ-transition is shifted to a complete resonant condition with the excitation laser, so that the correct intensity value becomes difficult to determine.

A comparison between the intensities caused by the X_{xy}-valley excitons and the signal of unknown origin is presented in Fig. 3-8(a). The intensities can be seen as nearly constant in the low-energy part of the indirect regime, but are dropping fast as soon as the blue-shifted signals appear. The new signals intensity increases as fast as the first one decreases. With the limited number of carriers excited in the semiconductor, the distribution of these is changed in the course of the excitation energy dependence. With the optical absorption taking place in the Γ-transition, the excited carriers relax down to the lowest excited state under dissipation of energy and in case of indirect excitons even under the change of their momentum. Indirect excitons are populated under the emission of an optical or

acoustic phonon. As the density of states is significantly higher at longitudinal optical phonon energies, the intensity behavior should present a maximum under the resonant condition of $\Delta E_{\Gamma-X} = \hbar\Omega_{\mathrm{LO}}$, with Ω_{LO} being the LO phonon frequency. The measured results, as they are depicted in Fig. 3-8(a), do not confirm this assumption. In fact the appearance of the second feature acts as a reservoir, hindering the further population of the lower lying X_{xy}-exciton state. The increased intensity of the second feature speaks for a significant faster recombination rate being present for excitons trapped in this state. Additionally, with increased excitation energies the density of excited QDs is also increased, as the maximum of the QD size distribution is achieved.
Under the application of high magnetic fields along the growth direction of the QD structure (Faraday geometry), the previously degenerated spin states are split by the Zeeman energy $E_{\mathrm{Z}} = g\mu_{\mathrm{B}}B$. Excitons populating the Zeeman split states recombine under the emission of right- (σ^-) or left- (σ^+) circularly polarized light corresponding to the bright exciton angular momentum from $|-1\rangle$ to the vacuum state $|0\rangle$, and $|1\rangle$ to $|0\rangle$, respectively. Apart from the constant Bohr magneton μ_{B} and the magnetic field strength B, with its direction parallel or anti-parallel to the optical axis, the sign of the magnetic field induced circular polarization is determined by the sign of the exciton g-factor. For Fig. 3-8(b), the selectively excited PL has been measured circular-polarization resolved at a magnetic field strength of $B = 6$ T in Faraday geometry. The corresponding circular polarization degree ρ_c is consequently calculated by

$$\rho_{\mathrm{c}} = \frac{I^+ - I^-}{I^+ + I^-}. \tag{3.1}$$

The intensities I^- and I^+ represent herein the sum of photons with σ^-- and σ^+-polarization. The circular polarization degree is illustrated in Fig. 3-8(b) by the red line, and the PL feature energies are marked by colored arrows. The spectrum shown in Fig. 3-8(b) still includes a high background, meaning that the real polarization degree of the distinct PL features is significantly higher, as the PL intensities are small compared to the background luminescence. In contrast to the ground state exciton emission, marked by the red arrow, the blue-shifted feature (blue arrow) shows an opposite polarization with considerably higher values. Although the value of the circular polarization degree also depends on the relation between the spin relaxation and recombination time $\frac{\tau}{\tau+\tau_s}$, known as the dynamical factor [76], a change of the polarization sign can only be achieved by an exciton g-factor of opposite sign. Close to the excitation line at 1.707 eV, some direct Γ-valley exciton contribution can be detected, showing a polarization sign in the same direction as the PL feature of unknown origin. For comparison, the same circular polarization degree spectrum measured at a zero magnetic field is included, shown by the black line. The absence of any polarization under this condition proves that the previously seen circular polarizations are indeed magnetic field induced and do not originate from the optical excitation.
Furthermore, the magnetic field induced circular polarization degree has been mea-

sured in dependence on magnetic field strength for three different angles Θ between the field direction and the sample growth axis, ranging from 0° to 70° in Fig. 3-8(c). As in the previous measurement, exemplarily seen in Fig. 3-8(b), a linear polarization has been used for the excitation, assuring that circular polarizations are solely caused by magnetic field split states. For the exact evaluation of the circularly polarized PL intensities I^- and I^+ of the distinct features, the spectra have been subtracted by the background and non-resonant PL contributions. An integration over the specific spectral regions holding the features results in the exact determination of these intensities. In exact Faraday geometry with an angle of $\Theta = 0°$, the polarization degrees for both signals, marked by square symbols, behave like seen before in Fig. 3-8(b). The X_{xy}-exciton, presented by red symbols, shows a positive polarization of up to 15 % at 10 T in contrast to the unknown signal, which has a negative polarization of -75 % at the same field strength, shown by blue symbols. A saturation of the maximal polarization degree cannot be seen for neither of the signals and seems to require an even stronger magnetic field strength than provided. At smaller tilting angle of $\Theta = 20°$ (circle symbols) the polarization degree of both signals is shifted to positive values increasing the maximal polarization degree of the X_{xy}-exciton to 36 % and decreasing the second one to -55 % at 10 T. The increased polarization in case of the X_{xy}-exciton can be explained by the inhomogeneity of the heavy-hole g-factor, which is maximal in Faraday geometry and decreases, best described by a cosine-function, to a minimal value in Voigt geometry.[‡] This is at least approximately seen by the third set of data representing the circular polarization degrees at $\Theta = 70°$, shown by triangle symbols, close to the Voigt geometry. In this configuration the X_{xy}-valley exciton has the largest circular polarization degree value due to a decreased heavy-hole g-factor in contrast to an unaltered electron g-factor. The consequence of that is an increased bright exciton g-factor, calculated by $g_{\mathrm{X}} = g_{\mathrm{hh}} - g_{\mathrm{el}}$, giving rise to the large polarization degrees. On the opposite, the PL feature of unknown origin has a drastically reduced polarization degree close to zero in this configuration. The anisotropy of the exciton g-factors can therefore be seen for both excitons, but with opposite results for their polarization degrees.

Apart from the determination of energetic and spin properties, the PL decay of the discrete feature could allow some conclusions about its origin. The implementation of an acousto-optical modulator into the optical excitation beam grants the possibility to analyze this feature in the time-resolved regime. Based on the settings of the modulator, the excitation is modulated to pulses of 100 ns length, which are repeated every 100 μs ($f_{\mathrm{Rep}} = 10$ kHz). In Fig. 3-9 the PL decay of the high-intensity feature, excited at $E_{\mathrm{Exc}} = 1.722$ eV is depicted, in which the black vertical line signifies the end of the excitation. As can be immediately seen, the PL decay exceeds several hundreds of nanoseconds indicating an indirect nature of this PL feature. A two-folded exponential decay function best describes the dynamical behavior of this recombination process with the two PL lifetimes

[‡]This behavior will be further described in chapter 4.

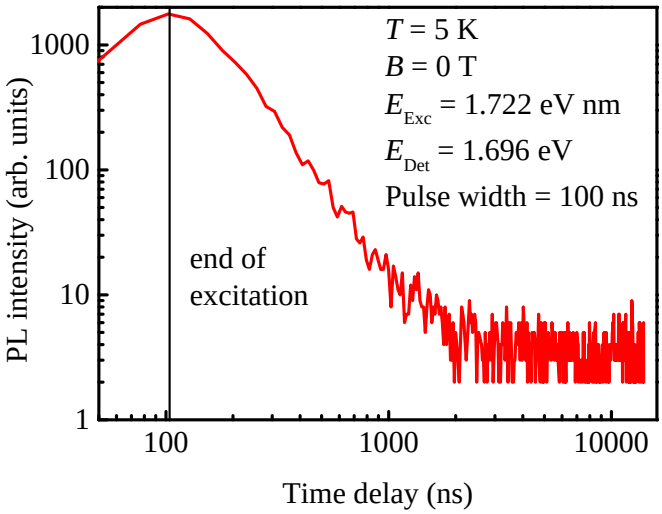

Figure 3-9: PL decay of the high-energy PL feature under resonant and pulsed excitation. With the end of the excitation pulse at a time delay of $t \approx 100$ ns the excitons radiatively recombine in the time range of several hundreds of nanoseconds. A two-folded exponential decay function is used to fit the recombination, giving the lifetimes of $\tau_1 = 82$ ns and $\tau_2 = 320$ ns, which both exceed direct recombination times.

$\tau_1 = 82$ ns and $\tau_2 = 320$ ns. Unfortunately, under these conditions the X_{xy}-valley exciton intensity is too small to be properly detected, so that non-resonant PL intensities dominate the spectral region of its appearance.

Based on the gathered results, the blue-shifted PL feature can have several possible origins all representing elevated energy states. The constant energy shift of 26 meV to the exciton ground state with X_{xy}-valley electrons and Γ-valley heavy-holes poses here a limiting factor. The following possible explanations can be thought of, which will be sequentially discussed:

(i) Indirect excitons with electrons trapped in the high energy X_z-state and corresponding heavy-holes in the Γ-point (X_z-valley exciton).

(ii) Indirect excitons with electrons in the X_{xy}-valleys and light-holes in the Γ-point (lh-exciton).

(iii) Indirect ground state exciton with X_{xy}-valley electron and Γ-valley heavy-hole coupled to an InAs LO phonon.

(iv) Excitation of an higher energy lying direct Γ-valley exciton with a consequent population of a second sub-ensemble of indirect X_{xy}-valley excitons.

(v) Indirect exciton state with its origin in the wetting layer.

(vi) X-valley conduction band state in the AlAs matrix inducing transitions together with heavy-holes left in the QDs Γ-point.

Let us discuss these possibilities in detail:
(i) As a typical feature of self-assembled QDs, these structures are lens or island shaped. Hence, the corresponding confinements perpendicular and along the growth direction (z-axis) are different, with the z-direction possessing the higher confinement. Exciton complexes, with electrons trapped in the X_z-valleys and heavy-holes in the Γ-points, can quite well explain the observed energy shifts of 26 meV from the exciton ground state to this excited state. The calculations performed for Fig. 3-4 confirm that. Additionally, the parallel energy shifts of the two distinct PL features with increasing excitation energies, seen in Fig. 3-7, reinforce this assumption. These shifts are the result of the increased confinement with decreasing QD sizes. The magnitude of the shifts depends highly on the effective masses of the corresponding conduction and valence band [82]. As the bands involved in the X_{xy}- and X_z-valley excitons complexes are identical, but under the influence of different confinement potential values, the similar slopes in Fig. 3-7 well reproduce the equal effective masses and would even explain the energy offset of both transitions. Additionally, the blocking effect described in Fig. 3-8(a) is in agreement with the idea of an excited X_z-valley exciton. With the emergence of this second PL feature, the transition of electrons from the initially excited Γ-state into the X_{xy}-valleys is hindered, as the X_z-valley exciton is closer in energy improving single acoustic phonon induced transitions into these valleys.
For interpretation of the oppositely polarized PL in the Fig. 3-8(b) and (c) under the consideration of the X_z-valley exciton, some results from chapter 4 have to be taken in advance. As it will be shown there, the highly isotropic g-factor of the indirect electron in the X_{xy}-valley will be determined with $g^{\parallel}_{\mathrm{el},X} = g^{\perp}_{\mathrm{el},X} = 2.00$, equal to the free electron one, while the exciton g-factor will be shown to be firstly anisotropic and, secondly, highly dependent on the spectral position based on the changes caused by the heavy-hole properties. In conclusion, the X_{xy}-valley exciton has a negative g-factor in the spectral range observed in Fig. 3-8(b). For the heavy-hole g-factor, this allows at least an approach of its magnitude, following $g_{\mathrm{X}} = g_{\mathrm{hh}} - g_{\mathrm{el}}$ to $g_{\mathrm{hh}} < 1.9$. As the X_z-valley exciton should be composed of heavy-holes from the same spectral region and as the circular polarization is obviously opposite, meaning a positive exciton g-factor ($g_{\mathrm{X}} > 0$), the conclusion has to be made, that the X_z-valley electrons have g-factors lower than 1.9. As the free electron g-factor g_0 is already the highest possible value achievable for electrons as single particles, a deviation from this value always reduces its value and can even reach high negative values: $g_{\mathrm{el}} = g_0 - \Delta g$. Deviations from the g-factor Δg are mostly based on spin-orbit interaction and can be described by the Roth, Lax and Zwerdling approximation [78] which can be written in a simplified relation to

$$\Delta g \sim \frac{E_{\mathrm{p}} \Delta_{\mathrm{SO}}}{E_{\mathrm{G}}^2}, \tag{3.2}$$

with the spin-orbit splitting of the valence band ground state Δ_{SO}, the band gap energy E_{G} and the energy of the matrix element describing the coupling between conduction and valence bands E_{p}. With the large band gap energies at the X-

valley symmetry points of around 4 eV [77], the deviations at this point are small and both electron g-factors can therefore also be predicted to be equal to a value of 2.0. Under these considerations the X_z-valley exciton g-factor cannot be smaller than its counterpart in the X_{xy}-valleys. This aspect poses the largest disagreement in the assumption of an indirect X_z-valley exciton.

(ii) The second potential origin for the high-energy shifted PL feature is related to an exciton composed of an electron in the X_{xy}-valley and a light-hole in the Γ-valley. The most severe aspect speaking against the assumption in (i) is the discrepancy of approximated positive exciton g-factors in consideration of the constant electron g-factor being equal to the free electron one. The observed magnetic field induced circular polarization degrees cannot emerge from corresponding Zeeman splitting. Contrariwise, light-holes can easily exceed heavy-hole g-factors ($g_{\mathrm{lh}} > g_{\mathrm{hh}} \approx 1.9$), meaning that a positive exciton g-factor would still be approved under assumption of an electron g-factor of 2.0. Furthermore, the strong angle dependence, seen in Fig. 3-8(c), could be explained by the strong anisotropy typically seen for light-hole g-factors. Under assumption of a positive light-hole g-factor of $g_{\mathrm{lh}}^{\parallel} \geq 2.0$ parallel and $g_{\mathrm{lh}}^{\perp} \approx 2.0$ perpendicular to the magnetic field direction, both the large negative polarization degree in Faraday geometry and the nearly absent polarization in the direction of the Voigt geometry could be explained. Accordingly, the associated exciton g-factor are $g_{\mathrm{X}}^{\parallel} \geq 0$ and $g_{\mathrm{X}}^{\perp} \approx 0$. Based on the large polarization degree, seen in the Faraday geometry the light-hole g-factor can even be assumed to be significantly larger than 2.0. Unfortunately, the exact light-hole value could not be determined up to now by the use of SFRS spectroscopy, so that the assumption cannot be verified.
Although the indirect light-hole exciton allows the description of the opposite circular polarization degrees seen for the two PL features, as well as the dependence seen with the change of the angle Θ, it shows disagreements with energy dispersion in Fig. 3-7. In this figure the two PL features are parallel to each other with increasing excitation energies. Based on the different effective masses of light- and heavy-hole for both InAs and AlAs, respectively, the confinement-driven energy shift should differ as well [82]. In specific values, the light-holes in a bulk InAs crystal have an effective mass of $m_{\mathrm{lh}} = 0.03m_0$ [85], while the heavy-hole mass takes $m_{\mathrm{hh}} = 0.34m_0$ [86]. In the case of AlAs bulk crystals the differences are not largely pronounced with $m_{\mathrm{lh}} = 0.16m_0$ [87] and $m_{\mathrm{hh}} = 0.41m_0$ [86], but should influence the PL feature shift additionally.[§] The shifts seen in Fig. 3-7 should follow therefore the Γ-X mixing energy $\Delta E_{\Gamma-X}$ and at the same time the hh-lh energy difference $\Delta E_{\text{hh-lh}}$ [88]. As this has not been observed in the energy dispersion, the concept of an indirect lh-exciton can be rejected as well.

(iii) The two PL-feature related energy shifts presented in Fig. 3-7 are separated

[§]Although the effective masses of the $(In_{0.3}Al_{0.7})As$ tertiary material cannot be taken as a linear combination of the original two component material properties, the values for the mixed material should lie in their range.

by an energy of approximately 26 meV from each other, with the feature of unknown origin being the one with higher energy. Additionally, it can be seen in the figure by the InAs LO phonon Raman lines, that the energy of these phonons are in the range of the observed energy differences. Moreover, with the emergence of the second PL feature, the LO phonon energies suddenly change from 32 to 25.5 meV, being close to the expected energies of 26 meV. The indirect X_{xy}-valley exciton would in such a case absorb an optical phonon and receive its energy and momentum. The latter aspect could induce furthermore the increased emission intensities of this complex in comparison to the exciton ground state, as the momentum mismatch Δk between electrons and holes in different symmetry points could be overcome. Although the absorption in contrast to the emission of an optical phonon is rather unlikely at temperatures used within the measurements, the possibility is given.
The drawback of this explanation lies in the magnetic field induced circular polarization degree in Fig. 3-7(b) and (c). With the polarization of the exciton ground state having one specific sign, a coupling of this state with a phonon could hardly change the sign of the polarization degree. Furthermore, the opposite changes, seen between the ground and excited exciton state with the angle dependence, could not be described by the explanation (iii).

(iv) This explanation is based on the excitation of a higher energy Γ-valley conduction band state and the consequent population of its corresponding X_{xy}-valley conduction band states. In a possible case, the optically accessible Γ-state transition energy of one QD subensemble with fitting QD sizes and composition is equal to the excited and either optically allowed Γ*-state transition energy of a second QD subensemble with different QD sizes. As a result, two different indirect exciton regimes would be populated with equal effective masses, explaining the parallel shift of both PL features in Fig. 3-7. Unfortunately, the excitation of an excited Γ-state would coincide with the population of larger QDs, with exciton ground state energies lower than that of the first PL feature. Accordingly, the concluding second PL feature should be red-shifted to the first one, which is not the case. Also the assumption that the previously denoted indirect X_{xy}-valley exciton could be associated to the excited Γ*-state cannot be retained, as both calculations and additional SFRS-measurement, presented in the following chapter, positively define the emergence of the indirect X_{xy}-valley exciton at the observed energy.

(v) The wetting layer, on which the QDs have been grown, has the shape of a narrow QW structure. As QWs are known to have confinement driven exciton ground states in the indirect regime as well [14], the additional PL feature could stem from recombinations taking place in these layers. One aspect speaking for the PL contribution originating in the wetting layer is the previously mentioned change of the InAs LO phonon energy. With the emergence of the second PL feature, the LO phonon energy drops from 32 to 25.5 meV. This reduction of energy could be explained by the transition between differently stretched lattices associated to QDs, possessing highly strained lattices, and wetting layers with lower-strained

lattices. Additionally, the oppositely polarized PL, exemplary seen in Fig. 3-8(b), can be explained by a higher heavy-hole g-factor in the wetting layer with a simultaneous electron g-factor equal to 2.0, as well.
Speaking against the assumption of a contribution of wetting layer states, are SFRS measurements of the heavy-hole spin-flip.[¶] Thereby, the intensities of the heavy-hole spin-flip excited in a wide range are measured, revealing a Gaussian distribution for the intensities without any singularities, which would speak for a crossing between QD and wetting layer states.

(vi) The assumption of an equally indirect transition in real (type II) and momentum space [84], poses an expansion of the previously interpreted case (v). The drawback speaking against (v) is resolved in this concept, as heavy-hole states associated to the QDs are part of the transition, so that heavy-hole spin-flip intensities still could follow the Gaussian distribution of the QD sizes. The exact transition consequently takes place between the electrons in the wetting layer X_{xy}-valleys with heavy-holes in the QDs Γ-points.
Type II structures possessing spatially separated carriers are known to have a strong excitation density dependence of their emission energies. With increasing excitation power, the PL lines are blue-shifted with shifts proportional to the cubic root of the excitation power density [83], in contrast to structures with a type I band alignment, in which the dependence is significantly smaller. The high-energy feature under study, finally, shows no change of its emission energies with increasing excitation power densities, although it has been excited in the course of the measurements with varying power densities in a large range. This basically neglects the possibility of a type I to type II transition.

In conclusion, none of the discussed explanation concepts for the high-energy PL feature approve to all properties observed, so that the origin of this feature remains unknown.[‖] The two concepts mentioned first are the most promising explanations. Both, the indirect X_z-valley exciton and the indirect light-hole exciton are able to explain distinct aspects of the higher energy PL feature. As an intermediate evaluation and expressing the writer´s persuasion, the distinct PL feature will in the following be denoted as the X_z-valley exciton to abbreviate its notation in the upcoming chapters.

[¶]In chapter 4 the SFRS spectroscopy technique will be used, especially to determine the g-factors of the indirect exciton ground state. There, the heavy-hole spin-flip intensities will be presented in a wide excitation range.

[‖]For a finalizing theory, calculations on the exact band schemes accounting for the exact sample properties still need to be performed. This would allow to discuss possible origins more precisely. Up to now the exact offsets both for the X_z-valley conduction band and light-hole valence band states could not be determined in sufficient precision.

3.3 Time-resolved properties of indirect excitons

In the previous chapter, the excitonic properties of distinct PL features have been examined in detail. Corresponding calculations reveal, that these can be accounted for indirect X_{xy}-valley electrons forming an exciton complex with a Γ-valley heavy-hole. To proof the indirect character of the exciton complexes in the k-space, this chapter will concentrate on the temporal behavior of the radiative exciton recombinations.

As the QDs are predicted to have indirect band gaps and carriers trapped in those expected to have long lifetimes, the excitation conditions need to be chosen carefully. The biggest problem being the accumulation of long-living carriers forming multi-exciton complexes or even the population of upper band states in the conduction band. The repetition frequencies for the time-resolved measurements need to be chosen in respect to the recombination dynamics of the indirect excitons, which can be five orders of magnitude larger in (In,Al)As/AlAs QDs than in (In,Ga)As/GaAs QDs [16].

As a first and more preliminary measurement an ensemble of QDs has been analyzed under different excitation densities, as seen in Fig. 3-10. For the above-barrier excitation of the sample S4, the third harmonic of a Nd:YVO_4 laser ($E_{\mathrm{Exc}} = 3.49$ eV) with a repetition frequency of 1.5 kHz has been used. The low frequency guarantees a complete recombination of carriers trapped in the QDs as the corresponding repetition period of $T_{\mathrm{Rep}} \approx 666$ μs is significantly longer than the decay curve of the PL. The use of too short repetition periods would not assure a system in its equilibrium condition in the moment of repeated excitation. As a result, the system would find a new equilibrium situation over time, which would not coincide with its lowest energy state. In general, this condition would coincide with an over-excited system.

In the measurement, different excitation densities have been used ranging from 12 μJ/cm^2 to 40 nJ/cm^2 (detailed list of excitation densities in the caption of Fig. 3-10). The PL decay curves show a two-stage behavior with the first being a flat PL decay right after the excitation, covering the first microsecond after the excitation. The second stage shows a decay following a power-law function corresponding to $I(t) \sim (1/t)^{\alpha}$. This behavior has been previously reported by Shamirzaev et al. [13]. The two time regimes seem to be influenced differently by high excitation densities. While the long range component following the power-law is not significantly changed, the initial decay is noticeable accelerated. The acceleration is on the one hand induced by multi-exciton complexes [89], which recombine faster than ground state excitons. On the other hand, excited conduction band states might be responsible. For excitation densities lower than 120 nJ/cm^2 the normalized PL decays coincide. It implies, that multi-exciton complexes are not created in the QDs. For this specific excitation density the average exciton population can be calculated, taking into account the absorption in the AlAs matrix and the QD density, to an average value of 0.3 excitons per QD and excitation pulse. To be on the safe side for later measurements, the average exciton popula-

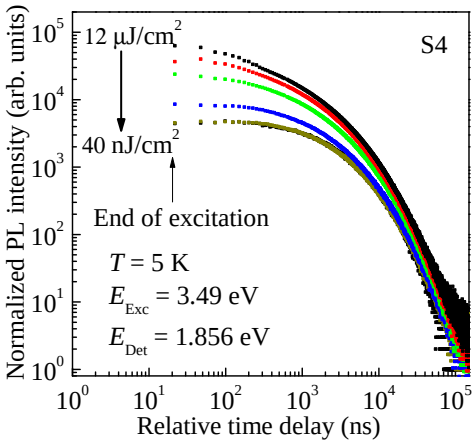

Figure 3-10: PL dynamics of sample S4 measured at $T = 5$ K at the maximum of the emission intensity ($E_{\mathrm{Det}} = 1.856$ eV) for a wide range of excitation densities. The double-logarithmically plotted PL decays have previously been excited by a 5 ns laser pulse with $E_{\mathrm{Exc}} = 3.49$ eV illuminating the sample with a repetition frequency of 1.5 kHz. To determine the influence of the excitation power, different power densities P [nJ/cm^2] have been used, starting from the top to the bottom with: 1.2×10^4, 4×10^3, 1.2×10^3, 400, 120, and 40. At excitation power densities of 120 nJ/cm^2 and below, the recombination dynamics are no longer accelerated.

tion has been reduced to 0.1 requiring the linear reduction of the excitation density down to 40 nJ/cm^2. Additionally, a repetition frequency of 1.5 kHz has proven to be adequate for the recombination processes to be fully completed in time.
Under these conditions the PL decays of the samples S1 to S4 have been measured, presented in Fig. 3-11. As the above-barrier excitation populates QDs of all sizes in the ensemble, the choice of the detection energy is made by a comparison of the continuous-wave excited PL spectra in Fig. 3-3. For each of the samples, three distinct energy values for the detection have been chosen which are related to a simulation of a Gaussian function for the four indirect PL spectra. The first detection energy (max) correlates to the the maximum of the intensity distribution. The two additional detection energies are shifted to the low- and high-energy side of the PL. The maximum of the PL and its low- and high-energy shifted FWHM-values, are related to the QD sizes D_{AV} (max), D_{S} (high) and D_{L} (low), respectively. By plotting the power-law function $I(t) \sim (1/t)^{\alpha}$ on the long range regime, the decay parameter α can be determined for all four samples and for every detection energy. The values for the parameter are inserted in Table 3-2. The variation of α shows that the value increases for all samples with increasing detection energies and therefore with decreasing QD sizes.
Additionally, the second regime obviously starts at different delays in respect to the end of the excitation. While for the samples S1 and S2 this change of the behavior starts several hundreds of nanoseconds after the excitation pulse, S3 and S4 decay characteristically on the single-digit microsecond scale. The perceivable

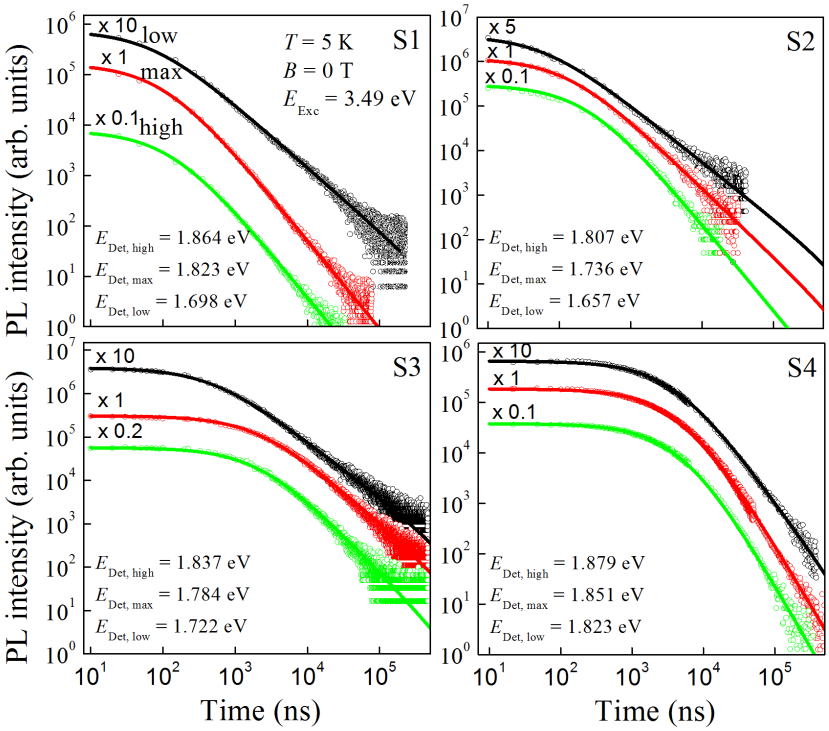

Figure 3-11: Low temperature PL dynamics of the four respective samples S1-S4. In resemblence to the excitation conditions in Fig. 3-10, 5 ns pulses from the third harmonic of the Nd:YVO_4 laser have been used at low excitation densities of $P = 40$ nJ/cm^2 and repetition frequencies of 1.5 kHz. The end of the excitation has been artificially shifted to 10 ns. The detection energies E_{Det} have been chosen to the maximum of the PL emission (max), as well as the low and high FWHM values of a Gaussian function used to describe the PL spectra in Fig. 3-3. In case of sample S2, the detection energy marked by low, deviates from this selection rule, as direct QD contributions would interfere at this spectral point. Instead a value corresponding to D^*_{L} in Fig. 3-3 has been chosen, closer to the emission maximum. To impove the visualization of the three graphs in one diagram, the intensities have been rescaled following the values written to the corresponding graph. The solid lines are calculated using the distribution function in Eq. (3.5) and the parameters included in Table 3-2.

non-exponential character of the recombination dynamics requires an alternative approach for a uniform analysis, including a distribution function $G(\tau)$ for the description of the lifetime distribution instead of a single lifetime. Although even single-QD PL decays rarely show pure mono-exponential behaviors [90], a stretched exponential function in the form of $I(t) \propto \exp[-(t/\tau)^{\beta}]$ often leads to a successful approximation of the decay. The function includes the recombination time τ and the factor β accounting for the dispersion [91, 92]. This factor already qualitatively delivers the same information as a distribution function $G(\tau)$ by taking values between $0 < \beta < 1$. Here, a value of 1 consequently describes a mono-exponential behavior and the absence of any dispersion, while a broad distribution function is described by values closer to zero [93]. A full description of the lifetime distribution

Sample	α			τ_0 ns		
	$I_{1/2}$ D_{S}	$I_{\max}$ D_{AV}	$I_{1/2}$ D_{L}	$I_{1/2}$ D_{S}	$I_{\max}$ D_{AV}	$I_{1/2}$ D_{L}
S1	1.75	1.75	1.30	130	100	70
S2	1.95	1.55	1.25*	240	130	60*
S3	1.75	1.50	1.35	2300	2100	700
S4	2.45	2.40	2.08	5400	5200	4000

Table 3-2: Characteristic decay parameters necessary for the simulation of the PL dynamics. The parameter α being the exponent of the power law function $I(t) \sim (1/t)^{\alpha}$, which describes the long-range decay regime, illustrates the slope of this decay regime and is closely related to the other decay parameter γ by $\gamma = \alpha + 1$. The second parameter included in the table is τ_0, characterizing the maximum of the lifetime-distibution function in Eq. (3.5). Values marked by * are related to the changed detection positions corresponding to D_{L}^{*} instead of D_{L}, as seen in Fig. 3-2 (S2).

is instead succeeded by an integral form for the intensity decay:

$$I(t) = \int_0^{\infty} G(\tau) \exp\left(-\frac{t}{\tau}\right) d\tau. \tag{3.3}$$

The distribution function can here be determined by a numerical solution [94, 95, 96] or by an analytical expression, as it has been assumed by Van Driel et al. [93] by use of a log-normal function:

$$G(\tau) = \frac{A}{\tau^2} \exp\left(-\frac{\ln^2(\tau_0/\tau)}{w^2}\right). \tag{3.4}$$

With a fitting constant A and the value τ_0 for the maximum of the exciton-lifetime distribution. The distribution width $\Delta_{1/\tau}$ for the inverse recombination times at a level of $1/e$ is described here by w. With the help of this expression the PL dynamics of many QD systems like CdSe/ZnSe colloidal QDs have been approximated [97]. In difference to the present (In,Al)As/AlAs QDs, these successfully simulated systems have PL decay times ranging between two orders of magnitude. The QD systems at hand covers decay times embracing more than five orders of magnitude in time. Accordingly, the expression (3.4) fails, as it can be seen in Fig. 3-12(a) and (b) for the samples S1 and S4, shown by red (1) and blue (2) curves. Instead, Shamirzaev et al. proposed a phenomenological expression for the distribution function taking into account the non-symmetric trend of the PL decay [18]:

$$G(\tau) = \frac{C}{\tau^{\gamma}} \exp\left[-\frac{\tau_0}{\tau}\right]. \tag{3.5}$$

As will be seen, this expression is able to describe PL dynamics which follow the power-law function $I(t) \sim (1/t)^{\alpha}$ and includes the parameter γ in correlation to

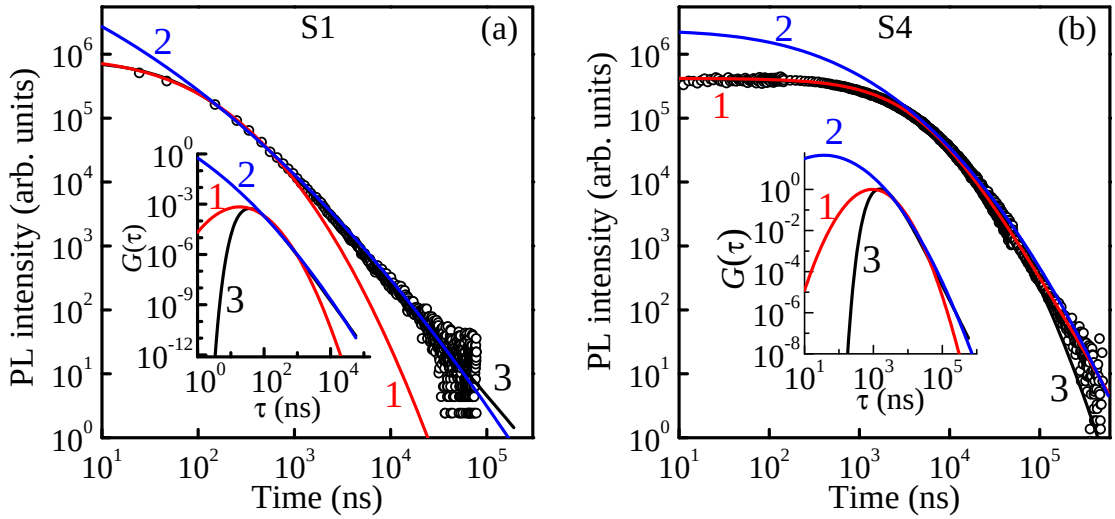

Figure 3-12: PL decay curves for the samples S1 (a) and S4 (b) measured at the emission maximum of the QD ensembles at low temperatures of $T = 5$ K. The measured PL decays are illustrated by open black circles, whereas simulated curves are represented by solid lines. The associated distribution functions $G(\tau)$ are in each case included in the insets. (a) The use of the log-normal distribution function (3.4) led to the graphs 1 and 2 with corresponding parameter sets of $\tau_0 = 0.2$ μs, $w = 1.55$ and $\tau_0 = 0.05$ μs, $w = 3.50$. By use of the distribution function (3.5) with distribution parameters $\tau_0 = 0.1$ μs and $\gamma = 2.75$, the PL decay has instead been successfully simulated over the complete time range, shown by graph 3. (b) Appropriate to the sample S1 in (a), the sample S4 has been attempted to simulate in case of the graphs 1 and 2 by using Eq. (3.4) with the parameters $\tau_0 = 5.8$ μs, $w = 1.35$ and $\tau_0 = 3.0$ μs, $w = 2.10$, respectively. The graph 3 again has been simulated with Eq. (3.5) with $\tau_0 = 5.2$ μs and $\gamma = 3.40$.

the known decay constant $\gamma = \alpha + 1$. Additionally, the expression uses τ_0 as lifetime-distribution maximum and an arbitrary constant C. As has been performed before, the constant α and consequently also γ can be derived from the long-time decay regime by plotting the power-law function on the data. With the help of this preliminary work, the complete shape can be fitted by the adaption of one fitting parameter τ_0. In Fig. 3-12(a) and (b) this fitting is additionally included, depicted by the black graph (3). In contrast to the previous attempts, this approximation is able to describe the complete PL dynamic over five orders of magnitude in time. The insets in the figures describe thereby the corresponding distribution function following Eq. (3.5). The fitting parameters τ_0 for all four samples have been evaluated, as illustrated in Fig. 3-13(a) and (b), and finally inserted in Table 3-2. As can be demonstrated by a comparison of the distribution functions with the PL decay, the influence of γ dominates the long-time regime, where the delays are longer than the characteristic lifetime τ_0. The initial stage of the PL decay has its origin in the radiative recombination of excitons with a lifetime equal to τ_0 or even less. An increase in the γ value consequently reduces the dispersion of the ensembles lifetime distribution based on its description in Eq. (3.5), from which the long-decay time regime benefits.

By comparison of the characteristic values τ_0 and γ of the four samples S1-S4 and

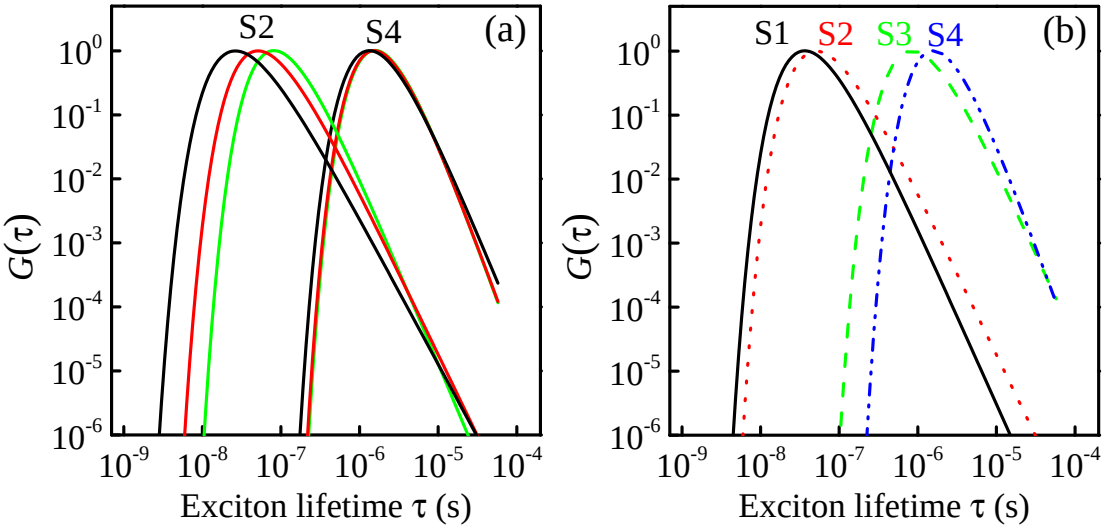

Figure 3-13: (a) Comparison of the lifetime distributions $G(\tau)$ for the samples S2 and S4. The size dependent distributions correspond to the QD sizes of $D_{\mathrm{L,S2}} = 17$ nm, $D_{\mathrm{AV,S2}} = 13.8$ nm, and $D_{\mathrm{S,S2}} = 9$ nm (from left to right) for sample S2 and $D_{\mathrm{S,S4}} = 28$ nm, $D_{\mathrm{AV,S4}} = 19.8$ nm, and $D_{\mathrm{L,S4}} = 12$ nm for sample S4. (b) Lifetime distributions of samples S1-S4 at their maximum size distributions related to $D_{\mathrm{AV,S1}} = 5.5$ nm, $D_{\mathrm{AV,S2}} = 13.8$ nm, $D_{\mathrm{AV,S3}} = 18.3$ nm, and $D_{\mathrm{AV,S4}} = 19.6$ nm.

its subsequent three emission energies, the influence of the QD sizes and the their heterointerface sharpness on the exciton recombination dynamics can be determined. A first insight to the effect of the QD size has already been given by the emission energy dependence.

With increasing QD size from D_{S} over D_{AV} to D_{L}, the values of τ_0 and γ decrease monotonically in all four samples. This effect of the QD size dependence is especially pronounced in the samples S1 and S2, which have not been affected by any post-grown annealing process.

The influence of the heterointerface sharpness on the PL dynamics can be observed by the comparison of $G(\tau)$ of the samples S2, S3 and S4 at emission energies corresponding to QD diameters of $D_{\mathrm{L,S2}} = 17$ nm, $D_{\mathrm{AV,S3}} = 18.3$ nm, and $D_{\mathrm{AV,S4}} = 19.6$ nm, respectively. The distribution functions evidence that with decreasing interface sharpness the exciton lifetimes are prolonged by two orders of magnitude. This indicates that the momentum scattering processes on the heterointerface influence the recombination of indirect-in-momentum space excitons significantly stronger than the influence of the QDs size.

Under theoretical considerations [18], the exciton lifetime is proportional to

$$\tau \propto \exp(d/a + d/h). \tag{3.6}$$

It considers the momentum scattering mechanism at the heterointerface in dependence of the lattice constant a, the QD height h and finally the thickness d of the (In,Al)As diffusion layer. As has been seen by the distribution functions shown in Fig. 3-13(b), the exciton lifetime is mainly determined by the heterointerface sharpness which corresponds here to the term $d/a \geq 1$, which only slightly changes

with the change in the QD size in one sample structure. For a single structure on the other hand, the lifetimes are then described by $d/h < 1$ resulting in a decrease of the lifetime with increasing QD size, exemplarily observable by the distribution functions of sample S2 in Fig. 3-13(a). The width of the distribution function, as it has previously been described by the parameter γ, is changed additionally by the heterointerface sharpness. In respect to the relation (3.6), variations of the argument $d/a + d/h$ can qualitatively characterize the width of the distribution function.
Mathematically, the broadening of a quantity is proportional to the square root of its average value [98], meaning that an increase in the argument $d/a + d/h$ also leads to a slow increase in the width of its distribution function. By use of the determined γ values, which are inversely proportional to the distribution function width, this assumption is confirmed, as the width of the distribution function increases with an increasing thickness of the interface layer.

3.4 Conclusion

In summary, the radiative recombination times in self-assembled (In,Al)As QDs can reach up to hundreds of microseconds depending on the exact growth and annealing conditions. Moreover, the resulting QD sizes, the InAs fractions inside the QDs, and the implementation of an interdiffused layer smoothing the QD-matrix heterointerface determine the maximal exciton lifetime; the latter is the dominating one. A mathematical solution for the description of the integral intensity dynamics is formulated by Eq. (3.3) using a distribution function for the exciton lifetimes. With the distribution function in Eq. (3.5), the PL decay of the (In,Al)As QDs, which ranges over five orders of magnitude in time, is successfully modeled. The corresponding lifetime-distribution functions allow additionally to improve the comparison of the sample specific recombination dynamics. By use of the approach in Eq. (3.6), the exciton-lifetime dependence can be further classified in geometrical QD features.

Chapter 4

Γ-X-valley mixed exciton

In the previous chapter it has been shown, that the indirect band gap of the (In,Al)As QDs results in very long exciton lifetimes and causes additional PL features with unusual characteristics compared to direct QDs. The present chapter is focused on the description of the mixing between the Γ- and X_{xy}-valley states. By use of spin-flip Raman scattering (SFRS) spectroscopy the exact g-factors of carriers and corresponding complexes are determined and the exact intermixing regime is exposed. As will be seen, the choice of correct excitation energies and geometrical angles between the sample growth axis and the applied magnetic field direction drastically influences the success in the observation of SFRS signals.* Key results of this chapter have been acquired in cooperation with J. Debus and are about to be published [20]. All SFRS studies presented in this chapter have been performed on the sample denoted by #2890, which has already been analyzed in chapter 3.2 by means of selectively excited PL measurements.

4.1 Determination of Γ-X mixed exciton g-factors

The SFRS spectroscopy is based on elastic light scattering, where the spin of a carrier or an exciton complex is reversed in the process. For example, an exciton spin state is resonantly addressed and the opposite spin-state emission is correspondingly detected. Typically, SFRS measurements are performed in presence of high magnetic fields, that split the spin states of the particle involved as well as the excitonic complex following the Zeeman splitting energy $E_{\mathrm{Z}} = g\mu_{\mathrm{B}}B$. In contrast to QDs with optically addressable exciton ground states, the indirect character of the (In,Al)As QDs allows no direct optical access to the X-valley states. A bypass constitutes here the mixing of electron Γ- and X-states, so that the total electron

*For further and deeper insight into the topic of spin-flip Raman scattering spectroscopy with emphasis on selection rules and theoretical background of SFRS, please review the dissertation of Jörg Debus [99].

wave function Ψ_{el} takes the form of a superposition:

$$\Psi_{\mathrm{el}} = C_{\Gamma}|\Gamma\rangle + C_X|X\rangle. \tag{4.1}$$

Here, $|\Gamma\rangle$ and $|X\rangle$ describe the Bloch functions, C_{Γ} and C_X the corresponding envelope function for the involved conduction band valleys. In order to receive information about the mixed state, the energy $\Delta E_{\Gamma-X}$, describing the energy difference between the Γ- and X-state, needs to be small, as with larger values a relaxation from the direct to the indirect band would not allow the exact addressing of single spin states. The energetic coincidence of both states becomes therefore important for the success of the measurements.
In chapter 3.1, the approximate energy regime for the Γ-X_{xy} mixing has been found by means of selectively excited PL at about 1.63 eV. At excitation energies below 1.63 eV the confinement-driven shift of the Γ-valley is not high enough, keeping the lowest state of the conduction band at the Γ-point. For higher energy values, the X_{xy}-state becomes equal or slightly lower in energy and allows a mixing of the conduction band states. Next to the choice of the excitation energy, the angle Θ between the sample growth axis and the magnetic field direction is important.
In Fig. 4-1(a), a SFRS spectrum is shown for sample #2890 excited at $E_{\mathrm{Exc}} = 1.636$ eV at $B = 5$ T and $T = 1.8$ K. Based on the principles described before, this should evoke a spin-flip signal in close proximity to the excitation line on top of the resonant PL. However, as the spectrum has been taken in exact Faraday and backscattering geometry with $\Theta = 0°$ the differential scattering cross section for a spin flip of a single carrier induced by acoustic phonons

$$\frac{d^2\zeta}{d\Upsilon d\omega_s} \propto |(\mathbf{e}_i \times \mathbf{e}_s^*) \times \mathbf{B}|^2 \tag{4.2}$$

is zero and no signal except resonantly excited PL can be seen [39]. The differential scattering cross section describes the probability of light to scatter with matter and is defined by the cross product of the incident light ($\mathbf{e}_i$) and scattered light polarization vectors ($\mathbf{e}_s$) and the magnetic field vector $\mathbf{B}$. In backscattering geometry, the cross section is only non-zero, if the magnetic field vector $\mathbf{B}$ has a non-zero component perpendicular to the propagation of the incident or scattered light vector. In Faraday geometry, this condition is not fulfilled and requires therefore the implementation of tilting angles $\Theta \neq 0$ in the xz-plane. The magnetic field vector is then described by $\mathbf{B} = B(\sin\Theta, 0, \cos\Theta)$.
In Fig. 4-1(b), the same measuring conditions as for (a) have been chosen with the exception of the angle $\Theta = 75°$. For the observation of the Raman shifts, the laser line has been recalculated to the zero-energy position (red line), presented by the red curve on top of the resonantly excited PL. Spin-flip signals stemming from the single particles heavy-hole (hh) and electron (el) and their exciton complex (X) are observed. With the application of high magnetic fields, their spin states are split following the Zeeman splitting energy. Consequently, the shifts depend on the magnetic field strength and the different g-factor values for the three signals. The heavy-hole SFRS signal with a shift of $\Delta E_{\mathrm{hh}} = 174\ \pm 5\ \mu$eV allows consequently

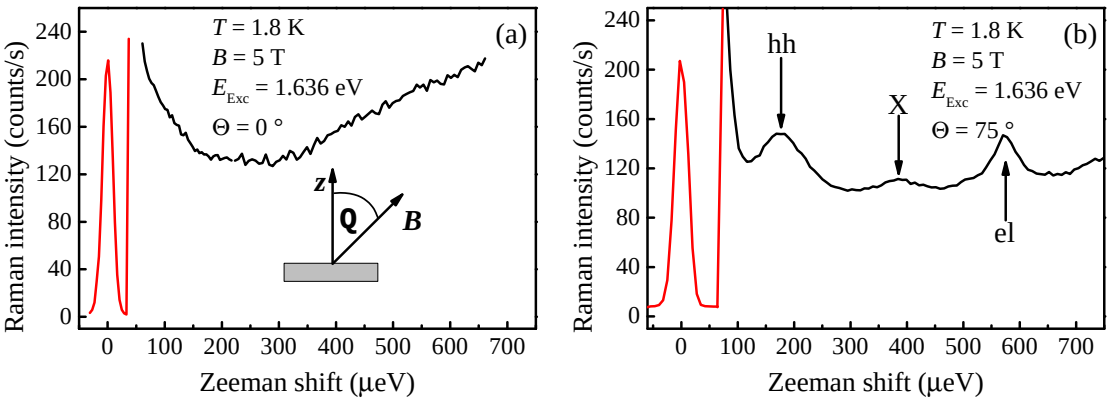

Figure 4-1: (a) SFRS spectrum of the Γ-X mixed exciton for the sample #2890 measured at $T = 1.8$ K in Faraday geometry ($\Theta = 0°$) at a magnetic field of 5 T. Apart from a resonant PL background, which does not shift with the magnetic field strength, no SFRS signals can be observed in this geometry following the differential scattering cross section described in Eq. (4.2). The scheme in figure (a) illustrates the angle Θ between the growth axis of the QDs (**z**) and the magnetic field direction (**B**). (b) SFRS spectrum of the mixed exciton state taken under the same condition as in (a) except for the angle Θ being increased to 75°. Under this condition, the spin-flip signals of the exciton (X), as well as single electron (el) and heavy-hole spin-flip signals (hh) can be observed.

the calculation of its g-factor to $g_{\mathrm{hh}} = 0.75 \pm 0.05$ for $\Theta = 75°$. It can be concluded, that it is the heavy-hole located at the Γ-point. The electron shows a SFRS shift of $\Delta E_{\mathrm{el}} = 575 \pm 3$ μeV corresponding to a g-factor of $g_{\mathrm{el}} = 2.00 \pm 0.01$. This large value for the electron g-factor, being close to the free electron one, is based on its indirect character. At X-valley symmetry points the band gap energies lie within about 4 eV [77]. Moreover, spin-orbit interactions can be neglected. The Roth, Lax and Zwerdling approximation describes the evolution of electron g-factors by [78]:

$$g_{\mathrm{el}} = g_0 \left[1 - \frac{\Delta_{\mathrm{SO}}}{3E_{\mathrm{G}} + 2\Delta_{\mathrm{SO}}} \left(\frac{m_0}{m_e^*} - 1 \right) \right]. \tag{4.3}$$

Here, g_0 is the free electron g-factor and Δ_{SO} the spin-orbit splitting of the valence band. E_{G} is the band gap energy, m_0 the effective mass of the free electron and m_e^* the one of the electron in the semiconductor. The consideration of large band gap energies at the X-valleys, as well as the small spin-orbit splitting result therefore in an almost unperturbed electron g-factor.
The third signal is dedicated to the exciton composed of the X-valley electron and Γ-valley heavy-hole. Its g-factor can both be experimentally determined as well as calculated by the single particle g-factors. The relation

$$g_{\mathrm{X}}(\mathbf{B}, \Theta) = g_{\mathrm{hh}}(\mathbf{B}, \Theta) - g_{\mathrm{el}}(\mathbf{B}, \Theta) \tag{4.4}$$

is valid for all magnetic fields and angles. The excitonic Raman shift takes the value of $\Delta E_{\mathrm{X}} = 388 \pm 5$ μeV, which is equal to a g-factor of $g_{\mathrm{X}} = 1.24 \pm 0.02$. Additionally, the calculation following Eq. (4.4) results in a similar value for the

exciton g-factor of $g_{\mathrm{X}} = 1.25 \pm 0.05$.
A more detailed analysis is given by a full magnetic field dependence of the Raman shifts, seen in Fig. 4-2(a). As the Zeeman splitting is a linear function of the applied magnetic field, the exact evaluation of the g-factors is granted, using a linear fit of the data experimentally collected and depicted in the figure by the colored lines. Moreover, the magnetic field dependence shows, that the g-factor is not a function of the magnetic field. The Zeeman effect for both the X-valley electron and Γ-valley heavy-hole is a linear function of B, and state mixings of non-linear contributions can be neglected.
The SFRS technique also allows the detection of the exciton exchange interaction δ_0, which would be seen as a zero field offset. In case of the indirect (In,Al)As QDs, this offset is not detected at this high tilting angle. The reason for the inability to see the electron-hole exchange coupling can be attributed to fast heavy-hole spin relaxations within the photo-excited exciton. The heavy-hole spin relaxation time is significantly faster than $\delta_0/\hbar$ [100], which is the result of the admixture between bright and dark exciton states, corresponding to the high tilting angle of 75°.
In Fig. 4-2(b), the angular dependences of the g-factors are depicted ranging from $\Theta = 0°$ (Faraday geometry) to $\Theta = 90°$ (Voigt geometry). As can be easily seen, the electron g-factor is only slightly influenced by the tilting angle between the sample growth axis and the magnetic field direction: $g_{\mathrm{el}} = g_{\mathrm{el}}^{\parallel} = g_{\mathrm{el}}^{\perp} = 2.00 \pm 0.01$. It has already be seen in other indirect band gap structures [101, 102].
A stronger dependence is observable for both the heavy-hole at the Γ-valley and consequently the Γ-X mixed exciton g-factors. For the description of the heavy-hole g-factor tensor, the longitudinal $g_{\mathrm{hh}}^{\parallel}$ and transversal $g_{\mathrm{hh}}^{\perp}$ values are required, representing the g-factors along and perpendicular to the magnetic field direction. In knowledge of these two extreme values, the angle-dependent g-factor can be calculated by

$$g_{\mathrm{hh}}(\Theta) = \left[(g_{\mathrm{hh}}^{\parallel} \cos\Theta)^2 + (g_{\mathrm{hh}}^{\perp} \sin\Theta)^2 \right]^{1/2}. \tag{4.5}$$

The use of Eq. (4.5) vice versa allows the calculation of $g_{\mathrm{hh}}^{\parallel}$ and $g_{\mathrm{hh}}^{\perp}$ by adapting the function to the measured angle dependence. This estimation results in values of $g_{\mathrm{hh}}^{\parallel} = 2.43 \pm 0.04$ and $g_{\mathrm{hh}}^{\perp} = 0.03 \pm 0.06$. The small transversal g-factor is furthermore an indication of the absence of light-heavy-hole mixing in the Γ-valley. The angle-dependent exciton g-factor is consequently a linear combination of the isotropic electron g-factor and the angle-dependent heavy-hole g-factor with $g_{\mathrm{X}}(\Theta) = g_{\mathrm{hh}}(\Theta) - g_{\mathrm{el}}$. For simplicity, the transversal heavy-hole g-factor can be neglected [103] reducing the equation to $g_{\mathrm{X}}(\Theta) = g_{\mathrm{hh}}^{\parallel} \cos\Theta - g_{\mathrm{el}}$. Using this equation, the indirect exciton g-factor can be estimated to $g_{\mathrm{X}}^{\parallel} = 0.43 \pm 0.08$ in longitudinal and $g_{\mathrm{X}}^{\perp} = -1.97 \pm 0.08$ in transversal configuration.
The sign of $g_X^{\parallel}$ can be gathered from the negative circular polarization degree induced by magnetic fields, depicted in Fig. 4-3(a). The polarization degrees in this figure have been calculated by Eq. (3.1), using the polarization-resolved PL excited by an above-barrier illumination of $E_{\mathrm{Exc}} = 2.33$ eV. The small negative

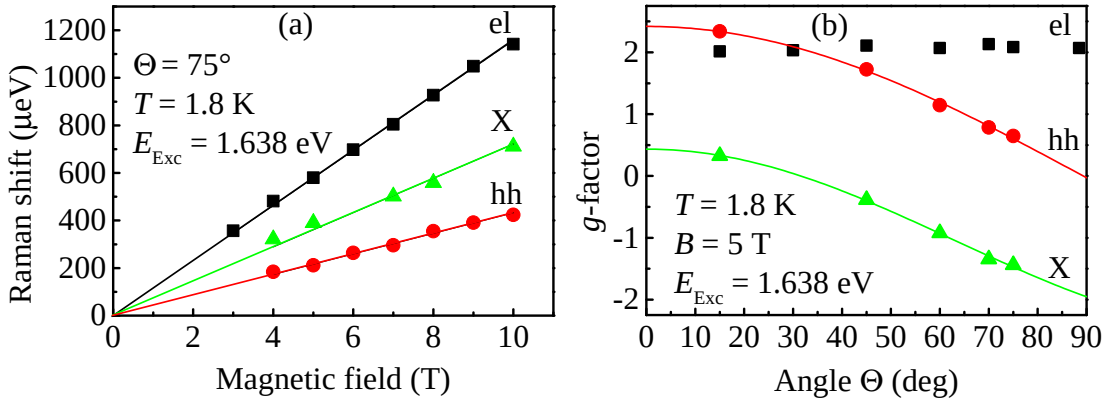

Figure 4-2: (a) Magnetic field dependent Raman shifts of the three spin-flip Raman signals. The Raman shifts of the three spin-flip signals in the Γ-X mixed regime, seen in Fig. 4-1(b), have been determined at $T = 1.8$ K for a tilting angle of $\Theta = 75°$. The linearity of the Raman shifts with the magnetic field strength follows the linear Zeeman splitting $g\mu_B B$. Noteworthy, is an absent zero-field offset for the exciton, which is the result of fast heavy-hole spin relaxations, faster than $\delta_0/\hbar$. (b) Angle dependence of the three g-factors. At a fixed magnetic field of $B = 5$ T the g-factors have been determined for different angles Θ from zero degree (Faraday) to 90° (Voigt). While the electron g-factors are only slightly influenced in tilted geometry, the heavy-hole g-factors follow a cosine-dependence with increasing tilting angles with the extrema $g_{\mathrm{hh}}^{\parallel} = 2.43 \pm 0.04$ and $g_{\mathrm{hh}}^{\perp} = 0.03 \pm 0.06$. The exciton g-factor shows an appropriate cosine-behavior following Eq. (4.4).

polarization degree is seen in the region II and corresponds to the Γ-X mixed exciton state with a g-factor of 0.43, while region I represents the direct excitons with heavy-holes and electrons originating from the Γ-point. As the direct electron could not be observed in the SFRS-spectra, it can be assumed that the corresponding g-factor is small and the resulting spin-flip signal is too close to the laser stray light to be properly resolved. Yugova et al. [36] estimated the Γ-valley electron g-factor in GaAs QWs to $g_{\mathrm{el}} = 0.1$, which coincides with this assumption. The heavy-hole g-factors in this region can be additionally assumed to be close to those determined in region II. In conclusion, the direct Γ-exciton has, although not exactly determined, g-factors larger than zero, which is seen by the negative circular polarization degree in regime I.

The third regime, following our analysis, largely consists of indirect excitons with electrons occupying the X_{xy}-valleys and heavy-holes in the Γ-symmetry point. It can be seen, that in this regime the circular polarization degree changes to positive values, thus indicating a negative exciton g-factor. Following the Roth, Lax and Zwerdling approximation (4.3), the electron g-factors in this region are unchanged and can be predicted to have a value equal to 2.0. In condition of Eq. (4.5) and (4.4), the heavy-hole g-factor has to be decreased to a value lower than 2 for the resulting positive polarization values of the exciton.

As discussed above, the mixing of the conduction band states and the non-zero magnetic field component along the z-axis initiate and enable the observation of electronic SFRS signals. In order to evaluate the exact spin-flip mechanism taking

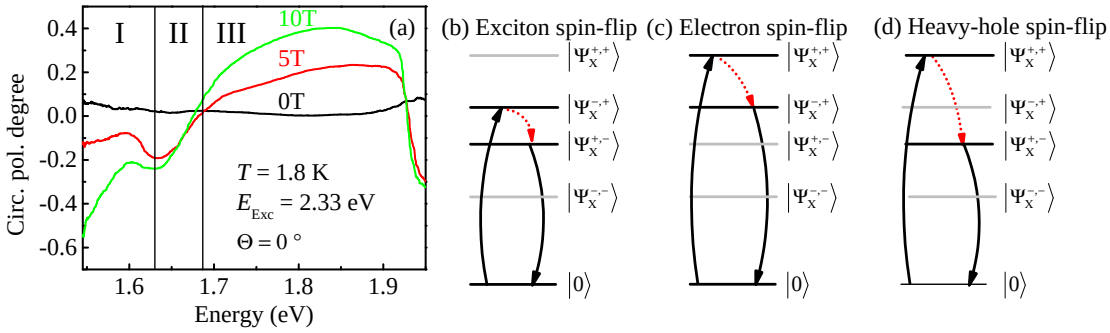

Figure 4-3: (a) Magnetic field induced circular polarization degree of the sample #2890 measured at $T = 1.8$ K. The above barrier excited ($E_{\mathrm{Exc}} = 2.33$ eV) sample was placed in exact Faraday geometry, while the magnetic field strength was increased from $B = 0$ T to $B = 10$ T. Three distinct regimes can be observed with significantly different polarization degrees originating from QDs with different energy levels. The first regime (I) with large negative polarization degree can be attributed to direct band gap QDs with large positive exciton g-factor, while the second regime (II) includes indirect QDs with smaller g-factors (see text for exact value). The third regime is governed by indirect QDs, whose heavy-hole g-factors are smaller than the electron ones. (b)-(d) Schematic spin-flip mechanisms induced by acoustic phonons for exciton, electron, and heavy-hole.

place in the QDs, a theoretical approach is necessary. Under the conditions of an absent light- and heavy-hole mixing and negligible shape variation of the QDs, ensuring a QD symmetry not lower than D_{2d}, the magnetic Hamiltonian takes the form

$$\hat{H}_B = \frac{1}{2}\mu_{\mathrm{B}}\left(g_{\mathrm{el}}^{\parallel}\cos\theta\sigma_z B_z + g_{\mathrm{el}}^{\perp}\sin\theta\sigma_x B_x\right) + g_0\mu_{\mathrm{B}}\left(\kappa_{\mathrm{KL}} j_z + q_{\mathrm{KL}} j_z^3\right) B_z. \qquad (4.6)$$

The Hamiltonian includes the Pauli matrices $\sigma_{x,z}$ and the z-component heavy-hole angular momentum operator j_z. The second term in the equation represents the Kohn-Luttinger Hamiltonian with the parameters κ_{KL} and q_{KL}. As in the previous descriptions, the angle Θ stands for the angle-dependent mixing between the conduction band states allowing the spin-flip scattering. The conduction band spin states under these conditions are $|\Psi_{\mathrm{el}}^{\pm}\rangle = \cos(\Theta/2)|\pm 1/2\rangle \pm \sin(\Theta/2)|\mp 1/2\rangle$, while the valence band and therefore heavy-hole states are $|\Psi_{\mathrm{hh}}^{\pm}\rangle = |\pm 3/2\rangle$. For the excitons confined in the QDs, their states are the products of both states corresponding to $|\Psi_{\mathrm{X}}^{\pm,\pm}\rangle = |\Psi_{\mathrm{el}}^{\pm}\rangle \cdot |\Psi_{\mathrm{hh}}^{\pm}\rangle$. The first index being the electron spin state and the second one describing the heavy-hole spin state. The exciton spin states involved in the spin-flip processes are schematically depicted in the Fig. 4-3(b)-(d). By means of an incident photon with an energy of E_{i} the exciton state $|\Psi_{\mathrm{X}}^{-,+}\rangle$ is created. In the following the exciton spin state scatters with an acoustic phonon, resulting in the change of the exciton spin state to $|\Psi_{\mathrm{X}}^{+,-}\rangle$. The change of the spin coincides with a reduction of the exciton energy by the amount of the Zeeman splitting energy $g_{\mathrm{X}}\mu_{\mathrm{B}}B$. The recombination of electron and heavy-hole causes the exciton spin transition from $|\Psi_{\mathrm{X}}^{+,-}\rangle$ to the vacuum state $|0\rangle$. This process is therein accompanied with the emission of a photon having the energy of $E_{\mathrm{em}} = E_{\mathrm{i}} - g_{\mathrm{X}}\mu_{\mathrm{B}}B$. The exciton spin-flip requires the simultaneous

change of the electron and heavy-hole spin states and is consequently a process of low probability, which is displayed by the small exciton spin-flip intensity in the SFRS spectra. On the contrary to this mechanism, the electron and heavy-hole spins start with the transition from $|0\rangle$ to the $|\Psi_{\mathrm{X}}^{+,+}\rangle$, which becomes optically accessible by the admixture of the $s_{z,\mathrm{el}} = -1/2$ electron spin state. Here again an acoustic phonon scattering of the spin state results in the transition to the $|\Psi_{\mathrm{X}}^{-,+}\rangle$ and $|\Psi_{\mathrm{X}}^{+,-}\rangle$ state, respectively. By means of recombination, photons of reduced energies are emitted corresponding to the single-particle Zeeman splitting energies as seen in the SFRS spectra. Scattering mechanisms involving the $|\Psi_{\mathrm{X}}^{-,-}\rangle$ state require the absorption of acoustic phonons and would only be seen in the anti-stokes regime of SFRS spectra.

4.2 Efficiencies of spin-flip Raman scattering processes

Apart from the shift caused by the Zeeman splitting seen as Raman shift, the SFRS signal intensities hold information about the scattering efficiencies along the QD ensemble. By the observation of the mixed electron spin-flip intensity, the exact Γ-X mixing energy can also be calculated using a two-level quantum system approach. The basis has already been given by the mixed wave function in Eq. (4.1), in which the two states $|\Gamma\rangle$ and $|X\rangle$ are taken as the two orthogonormalized basic states yielding the unperturbed eigenenergies $E_j (j = \Gamma, X)$. The lower (-) and higher (+) lying energy levels read:

$$E_{\mp} = \frac{E_\Gamma + E_X}{2} \mp \frac{1}{2}\sqrt{(E_\Gamma - E_X)^2 + 4V_{\Gamma-X}^2}\ . \tag{4.7}$$

The coefficients $C_j^{\mp}$ for these levels therein take the form

$$\begin{aligned} |C_\Gamma^{\mp}|^2 &= \frac{1}{2}\left(1 \pm \frac{\Delta E_{\Gamma-X}}{\sqrt{\Delta E_{\Gamma-X}^2 + \delta^2}}\right) \quad \text{and} \\ |C_X^{\mp}|^2 &= \frac{1}{2}\left(1 \mp \frac{\Delta E_{\Gamma-X}}{\sqrt{\Delta E_{\Gamma-X}^2 + \delta^2}}\right), \end{aligned} \tag{4.8}$$

where $\Delta E_{\Gamma-X}$ is again the difference between the Γ- and X-state and $\delta = 2|V_{\Gamma-X}|$ is the modulus of the coupling matrix element of the states $|\Gamma\rangle$ and $|X\rangle$, which is based on the mixing between the Γ- and X-conduction band states in a QD. The coefficients allow the composition of a two-level quantum system g-factor

$$g^{\pm} \equiv g(\Delta E_{\Gamma-X}) = g_\Gamma |C_\Gamma \pm|^2 + g_X |C_X \pm|^2, \tag{4.9}$$

where g_Γ and g_X are the electron g-factors in their bare state $|j\rangle$. On basis of this preliminary work, a concept for the electron-SFRS intensity dependence can be created. As such a signal is based on a three-folded process including the excitation by a photon $\hbar\omega_i$, an acoustic phonon scattering of the spin state and finally the emission of a secondary photon $\hbar\omega_{\mathrm{em}}$, the intensity of the SFRS signal I_{sc} is proportional to the product of all involved single process probabilities:

$$I_{\mathrm{sc}} \propto I_0 W_{\mathrm{em}} \tau_{j\bar{s}} W_{\mathrm{sf}} \tau_{js} W_{\mathrm{abs}}. \tag{4.10}$$

The intensity of the excitation light is here I_0, the spin index is described by s with $\bar{s} = -s$, and the exciton lifetime in the state $|js\rangle$ is τ_{js}. In a short form, the exciton lifetime takes the form $\tau_{js} = \frac{\tau_0}{|C_\Gamma|^2+\alpha}$ with $\alpha = \frac{\tau_0}{\tau} \ll 1$. The probability rates W for the absorption, spin-flip process and consequent emission are

$$\begin{aligned} W_{\mathrm{abs}} &\propto |M_{js,0}(\mathbf{e}_{\mathrm{i}})|^2 \delta(E_{js} - \hbar\omega_{\mathrm{i}}), \\ W_{\mathrm{sf}} &\propto |V_{j\bar{s},js}|^2 \left(N_{\mathrm{phon}} + \frac{1 \pm 1}{2} \right) \delta(E_{j\bar{s}} - E_{js} \pm \hbar s q), \\ W_{\mathrm{em}} &\propto |M_{0,j\bar{s}}(\mathbf{e}_{\mathrm{f}}^*)|^2 \delta(E_{j\bar{s}} - \hbar\omega_{\mathrm{f}}). \end{aligned}$$

The matrix elements of the involved processes are depicted by $M_{js,0}(\mathbf{e}_{\mathrm{i}})$, $M_{0,j\bar{s}}(\mathbf{e}_{\mathrm{f}^*})$ and $V_{j\bar{s},js}$ with $\mathbf{e}_{\mathrm{i}}$ and $\mathbf{e}_{\mathrm{f}}$ being the polarization unit vectors. The phonon occupation number is given by N_{phon} for phonons with the wave vector q. According to [58, 59] the probability of an acoustic phonon induced spin-flip event is proportional to the fifth power of the exciton Zeeman splitting energy, described by the simplified relation $W_{\mathrm{sf}} \propto [|C_X|^2]^5$.
For a further approach, few assumptions have to be made. Beginning with the energy shift between the Γ- and X-state, $\Delta E_{\Gamma-X}$, which shall be given by a sum over the average value $\bar{\Delta}$, dependent on the excitation frequency ω_{i}, and the random variation value $\tilde{\Delta}$. The distribution of $\tilde{\Delta}$ shall additionally be given by a Gaussian function with

$$F(\tilde{\Delta}) = \frac{1}{\sqrt{\pi}\tilde{\Delta}} \exp^{\tilde{\Delta}^2/\Delta_0^2}.$$

Finally, it can be assumed that the dispersion of $\tilde{\Delta}$ is larger than the one for δ or for the Zeeman splitting $g_{\mathrm{el}}\mu_{\mathrm{B}}B$. Under these assumptions the scattering intensity

of the three-step process is

$$I_{sc}(\omega_i) \propto \int_{-\infty}^{\infty} d\tilde{\Delta} \frac{e^{-\tilde{\Delta}^2/\Delta_0^2}}{\sqrt{\pi}\Delta_0} \left(\frac{\sqrt{\left[\overline{\Delta}(\omega_i)+\tilde{\Delta}\right]^2+\delta^2} - \left|\overline{\Delta}(\omega_i)+\tilde{\Delta}\right|}{(1+\alpha)\sqrt{\left[\overline{\Delta}(\omega_i)+\tilde{\Delta}\right]^2+\delta^2} - \left|\overline{\Delta}(\omega_i)+\tilde{\Delta}\right|} \right)^2 \times$$
$$\times \left(1 + \frac{\left|\overline{\Delta}(\omega_i)+\tilde{\Delta}\right|}{\sqrt{\left[\overline{\Delta}(\omega_i)+\tilde{\Delta}\right]^2+\delta^2}} \right)^5 . \tag{4.11}$$

To simplify the integration, it can be supposed that both variables δ and Δ_0 are independent of ω_i. For the average splitting value $\bar{\Delta}$ a proposal predicts that a linear ω_i-dependence following

$$\bar{\Delta}(\omega_\mathrm{i}) = \eta\hbar(\omega_\mathrm{i} - \omega_\mathrm{max}) \tag{4.12}$$

well describes the problem, in which ω_max is the specific frequency of the incident light exciting QDs at which the Γ- and X-levels mix most effectively. For the calculation of the SFRS spectra an integration over Eq. (4.11) is required. This is achieved by the use of a δ-form function $\delta(\Omega - |C_X(\tilde{\Delta})|^2)$ with the dimensionless frequency Ω normalized by the Zeeman splitting function of the pure X-state:

$$\Omega = \frac{\hbar(\omega_\mathrm{i} - \omega_\mathrm{f})}{g_\mathrm{X}\mu_\mathrm{B}B}.$$

Ω can be seen as a frequency difference ranging from zero at the Γ-state to unity at the X-state. With the help of this value, the coefficients $|C_X|^2$ and $|C_\Gamma|^2$ can be expressed much easier by:

$$|C_X|^2 = 1 + \frac{|\Delta E_{\Gamma-X}|}{\sqrt{\Delta E_{\Gamma-X}^2+\delta^2}} = \Omega \quad , \quad |C_\Gamma|^2 = 1 - |C_X|^2 = 1 - \Omega. \tag{4.13}$$

The integration of the δ-function therein results in the formulation of the density-of-states dependence:

$$I_\mathrm{sf}(\Omega) \propto \frac{e^{-\Delta_+^2/\Delta_0^2} + e^{-\Delta_-^2/\Delta_0^2}}{\sqrt{\pi}\Delta_0} \left(\frac{\Omega-1}{\Omega-1+\alpha} \right)^2 \frac{\Omega^5}{[1-(2\Omega-1)^2]^{3/2}}, \tag{4.14}$$
$$\Delta_+ = \delta\frac{|2\Omega-1|}{\sqrt{1-(2\Omega-1)^2}} + \overline{\Delta}(\omega_i), \quad \Delta_- = \delta\frac{|2\Omega-1|}{\sqrt{1-(2\Omega-1)^2}} - \overline{\Delta}(\omega_i).$$

On basis of this theory, the experimental results shown in Fig. 4-4 can be well analyzed and simulated. In the figure, the intensity of the electron and heavy-hole spin-flip signal intensities are plotted as a function of the excitation energies in the regime of the Γ-X mixing. The heavy-hole spin-flip intensity followes a Gaussian-

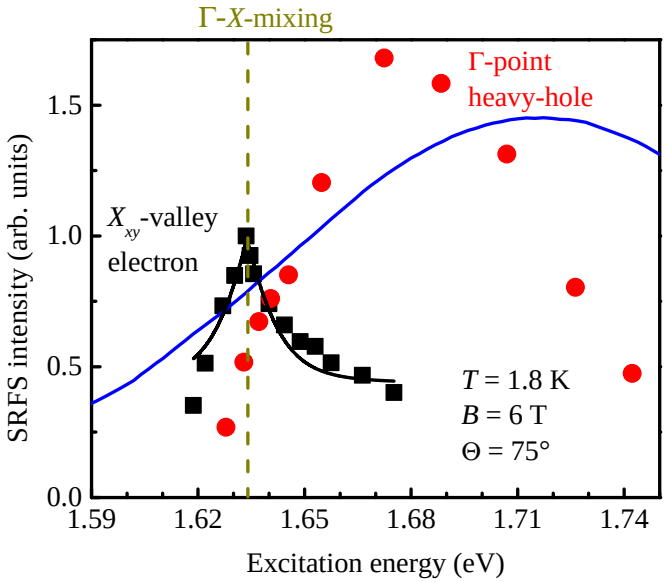

Figure 4-4: Resonance profiles for electron and heavy-hole spin-flip intensities as a function of excitation energies. Illustrated by black squares are the normalized intensities measured at $T = 1.8$ K, at a magnetic field of $B = 6$ T and at a geometry angle of $\Theta = 75°$. The electron spin-flip signals show an asymmetric resonance shape with its maximum at $E_{\mathrm{Exc}} = 1.633$ eV, being steep on the low-energy and smooth on the high-energy side. The maximum of this resonance can be taken as the Γ-X mixing point, thus indicating the stronger admixture between both electrons (direct and indirect). The black line represents the theoretical approximation for the electron spin-flip intensities. In contrast, the heavy-hole spin-flip intensities, marked by red points, follow a Gaussian distribution corresponding roughly to the ensemble´s density of states with a maximum at $E_{\mathrm{Exc}} = 1.685$ eV. Additionally included in the graph is the above-barrier illuminated PL, depicted by the solid blue-colored line.

function behavior. As the heavy-hole occupies the Γ-valleys solely, the spin-flip processes are less dependent on the mixing with the indirect conduction band states. But they depend on the indirect, long-living exciton density of states. On the contrary to this behavior, the spin-flip intensities of the mixed electron states follow a different behavior, with their maximum at the energy with the strongest mixing probability and the strongest exciton oscillator strength, respectively. The shape of the electron-SFRS resonance profile is highly asymmetric, being steep at the low-energy side and smooth on the high-energy side as predicted in the theoretical model presented above. For the classification of the energy position, the above-barrier illuminated PL is added as a reference by the solid blue-colored line. The black line following the electron spin-flip intensities is the theoretically calculated curve based on the Eq. (4.11). The best adaption of the theoretical model with the experimentally gathered data is achieved by a maximal excitation energy of $E_{\mathrm{max}} = E_{\mathrm{Exc}} = 1.633$ eV. In addition to that, the calculation produces $\tilde{\Delta} = 0.157$ eV, $\eta \approx 0.6$, $\delta = 0.012$ eV, and $\Delta_0 = -0.003$ eV as fitting parameters. The value of α, which takes the form of a modulation parameter has eventually a

value of 0.004.[†]

4.3 Conclusion

As has been seen in this chapter, the spin-flip signals measured by the SFRS-method are subjected to strict conditions, such as excitation energy, temperature, magnetic field value, and even incident angle, which have all been analyzed in detail. As shown in the last subchapter, especially the excitation energy dependence divides the indirect (In,Al)As/AlAs QDs from direct band gap QDs. Here, the indirect nature of the X_{xy}-valley excitons requires a mixing with direct Γ-states for the observation by optical methods. Furthermore, the g-factors for indirect electrons, Γ-valley heavy-holes and respective excitons have been determined.

[†]Note, that although this calculation allowes the determination of the exact point of Γ-X mixing, the theoretical background is still a work in progress, so that the results have to be taken with care.

Chapter 5

Spin relaxation times in indirect, negatively charged (In,Al)As QDs

The spin states of electrons and excitons in QDs are of great interest in modern research. In the fields of quantum computation and spintronics they pose one possible underlying system for applications, as they provide both an easy initialization as well as long lifetimes [42, 43]. Especially the second aspect is an advantage in semiconductor QDs, as the lifetimes in QDs are greatly enhanced. In the scope of this chapter, the spin relaxation times of negatively charged excitons in QDs will be determined. The choice of doped structures to excite charged exciton complexes has been made, as they provide in a first approach similar spin structures as single particles. In the provided measuring conditions therefore only singlet trion states need to be considered, in which the two electrons in the trion align their spin oppositely, compensating their contributions to the Zeeman splitting. Furthermore, these charged complexes lack the influence of the exchange interaction, so that no dark exciton states or intrinsic state splittings interfere the measurements of the spin relaxation time. The presented work corresponds to the publication [19].
In the first section of this chapter, the spin relaxation of charged excitons in presence of strong magnetic fields will be discussed and a detailed method for the analysis will be explained. As an alternative approach to the magnetic field induced circular polarization for the determination of the spin relaxation, the second section of this chapter describes the possibility to pump specific spin states by optical means. This technique does not require strong magnetic fields and as will be shown, allows the determination of similar results. In contrast to the undoped (In,Al)As/AlAs QDs, the doped structures do not show discrete PL features, which does not require a differentiation into X_{xy}- or X_z-valley excitons. The sample structure used in this chapter consists of self-assempled (In,Al)As QDs, embedded in an AlAs matrix, grown by MBE (Riper-32P system) on a semi-insulating (001)-orientated GaAs substrate. Ten layers of QDs have been placed in the sample to increase the density of QDs accessable by optical methods, which are separated by 30 nm thick AlAs layers. In order to charge each QD in average with one electron, a delta-layer is placed in the AlAs matrix 2 nm below each QD layer

consisting of silicon donors with a density of 1×10^{-12} cm^{-2} [15]. The sample has been designated as #2104.

5.1 Spin relaxation in negatively charged QDs in high magnetic fields.

The primary value describing the spin relaxation dynamics under a parallel applied magnetic field, is the longitudinal spin relaxation time τ_s. It describes the limitation in time, before the spin of a carrier or a complex, like an exciton, changes its state from the initiated situation back to the equilibrium. Theoretical considerations predicted, that the spin relaxation time is strongly exceeded in QDs in comparison to their bulk material counterparts. The wavefuntions of the particles are strongly localized in QDs, so that the most efficient relaxation processes like the Elliot-Yafet and the D'yakonov-Perel processes are suppressed [59, 58, 104].
The temporal limitation in these structures at low temperatures is therefore provided by the hyperfine interaction with nuclear spins and the carrier-phonon scattering. Based on recent publications, the theory predicts spin relaxation times as long as milliseconds, which exceed the recombination times of excitons in direct semiconductor nanostructures like (In,Ga)As/GaAs or GaAs/(Al,Ga)As QDs by several orders of magnitude [59, 58, 104].
The application of PL measurements, as a tool to determine the spin state dynamics, can therefore not always be used to analyse structures with τ_s-values exceeding the nanosecond time regime [105]. A direct observation of the population and an exchange between the spin states is therefore often not granted by this method and the information about the spin relaxation times normally only indirectly accessable. In difference to that, the recombination times τ of the indirect band gap excitons in (In,Al)As QDs in an AlAs matrix have, as has been shown in chapter 3.3, significantly longer recombination times of up to several hundreds of μs. Still, these structures are characterized as type I structures, whose electrons and holes are confined in the same QD [13, 15, 18] without a spatial separation. Using these structures, the limitation imposed by the exciton lifetime can be overcome and a full observation of the long-term spin relaxation becomes possible.
The inset in Fig. 5-1 illustrates a low-temperature PL spectrum, taken from the sample #2104 in the steady-state regime after excitation above the barrier at $E_{\mathrm{Exc}} = 2.33$ eV. The arrow signifies the maximum of the PL intensity and consequently the detection energy of $E_{\mathrm{Det}} = 1.720$ eV, which has been chosen for all time-resolved measurements on this sample. The PL is slightly blue-shifted compared to some of the undoped samples in chapter 3 and has a FWHM of 140 meV. This demonstrates, that the sample has been annealed in the doping procedure and signifies additionally, that the heterointerface has been smoothed in the process. The annealing procedure enables the transfer of averagely one electron from the doping material into each of the QDs.
The main part in Fig. 5-1 shows the unpolarized PL decay optained by single pho-

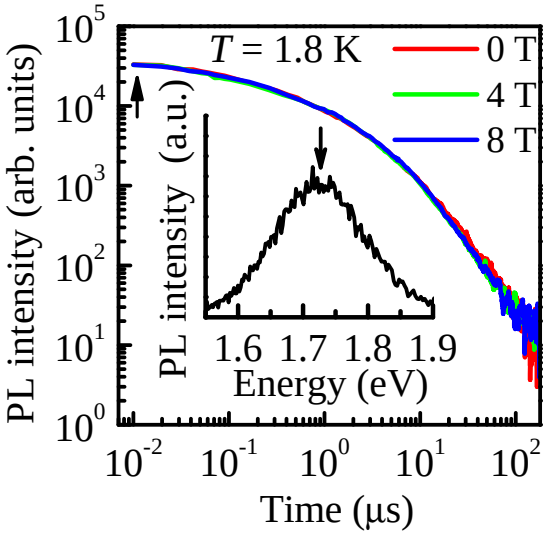

Figure 5-1: Unpolarized PL dynamics of indirect band gap (In,Al)As/AlAs QDs with increasing magnetic fields. Measured results are represented in a double-logarithmic scale to improve the conspicuity of the non-exponential PL decay [18]. The excitation pulse ends at a time of 10 ns, marked by an arrow in the graph. The PL dynamics have been measured at an energy of 1.720 eV. The inset shows the corresponding steady-state PL with an additional marking for the detection energy.

ton counting measurements at the specified energy and under the application of strong magnetic fields of up to 8 T. The graph is plotted in a double-logarithmic scale to demonstrate the non-exponential PL decay typical for the indirect band gap (In,Al)As/AlAs QD ensembles. This behavior stems from the recombination of different QDs emitting at the same energy, influenced by both the material composition and confinement in the QDs, respectively. Despite similar PL energies, these QDs possess different heterointerface sharpness with corresponding variations of τ, as has been described in chapter 3.3. Following the previous descriptions, the PL decay can be written in the style of Eq. (3.3) as:

$$I(t) = \int G(\tau)\exp\left(-\frac{t}{\tau}\right)d\tau.$$

The exciton lifetime distribution function $G(\tau) = (A/\tau^{\gamma})\exp(-\tau_0/\tau)$, in which τ_0 is the distribution maximum and γ a value characterizing the long-time slope of the distribution, is best adapted with $\tau_0 = 1.8$ μs and $\gamma = 2.65$. A demonstration of the trion lifetime distribution function $G(\tau)$ is given in the inset of Fig. 5-2(a). The prolonged PL decay on the μs timescale and the absence of any fast PL component proves, that with an energy of $E_{\mathrm{Det}} = 1.720$ eV, we detect only exciton complexes in the indirect regime of this sample´s QD ensemble.
Finally, the PL decays and the corresponding recombination times τ in the ensemble of QDs are not changed significantly under the application of an external magnetic field and can be taken as constant. With the application of strong magnetic fields, a circular polarization is induced in the (In,Al)As/AlAs QD PL. The

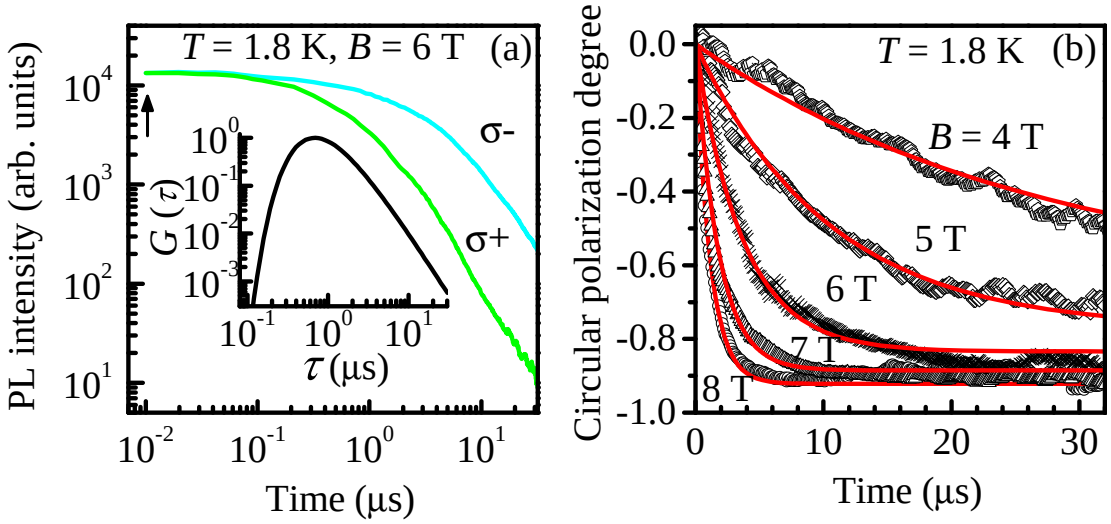

Figure 5-2: (a) Recombination dynamics of left- (σ^-) and right- (σ^+) circularly polarized PL components detected at the QD band maximum (1.720 eV) under the influence of an external magnetic field of $B = 6$ T. The arrow indicates the end of the excitation pulse at 10 ns. The inset shows the trion lifetime distribution function $G(\tau)$ of the n-doped sample #2104. (b) Dynamical circular polarization degree of the PL at different magnetic fields are shown by black symbols. Solid red lines are the results of calculations based on Eq. (5.5) yielding different τ_s-values and constant recombination times.

temporal evolution of the intensities of the two circular polarization components, are shown in Fig. 5-2(a), taken at a magnetic field of $B = 6$ T. In the range of several ns after the linearly-polarized excitation pulse, the intensities of both components differ no more than 3 %, speaking for an equal population of both spin levels. With larger delays, the intensity of the σ^+-polarized PL component $I^+(t)$ decreases much faster than the σ^--polarized component $I^-(t)$. With these two components the trend of the circular polarization degree can be calculated by:

$$\rho_c(B,t) = (I^+(t) - I^-(t))/(I^+(t) + I^-(t)). \tag{5.1}$$

In Fig. 5-2(b) the dynamical polarization degree, reflecting the thermalization between the Zeeman sublevels, are exemplarily plotted for several magnetic fields ranging from 4 to 8 T. With increasing magnetic fields, the final polarization degree increases consequently, saturating at a magnetic field strength of $B = 8$ T with a polarization degree of $\rho_c^{sat} \approx -0.92$ after 5 μs of rise time. Under this condition, the trion spin relaxation time is significantly faster than its recombination time, allowing the fast saturation of the polarization degree. At lower magnetic fields, τ_s becomes much smaller, resulting in lower saturation values for the polarization degree and consequently a much smaller slope of the polarization curve. With magnetic fields below 5 T, the polarization degree does not saturate within 30 μs. Based on the low signal-to-noise ratio, exceeding times of 30 μs, the dynamics of ρ_c can no longer be reliably evaluated.

The trion complex (T^-) in this negatively charged QDs consists of two electrons, one resident electron as well as one photoexcited electron, and one heavy-hole. Any

contribution from light holes can be neglected in this structure, as the splitting caused by biaxial strain and quantum confinement has been calculated to values of up to $\Delta E_{\text{hh-lh}} = 200$ meV [15]. This magnitude of the splitting cannot be compensated by neither an applied magnetic field or increased temperatures, used in the experiments at hand, and allows therefore to neglect any light-hole mixing. The fine structure of the T^--trion is solely determined by the heavy-hole g-factor [108]. As Pauli´s exclusion principle predicts, the two electrons contributing to the trion complex must have opposite spins, accordingly compensating their single electron spin contribution of $\pm 1/2$. The total spin projection of the T^--state is therefore described by -3/2 (+3/2). The recombination of the trion, causes an electron with the spin projection -1/2 (+1/2) to be left in the quantum dot, so that photons with a σ^-- (σ^+-) polarization are emitted. The g-factors of both, electrons and heavy-holes, have been found to be positive [20]. This allows to built a schematic diagram of the spin states and optically allowed transitions between the trion states and the resident carrier states, corresponding to Fig. 5-3(b). The emission of either σ^-- or σ^+-polarized luminescence is directly proportional to the population of the Zeeman split spin states, described in the diagram. The application of magnetic fields along the growth axis of the sample causes one of the spin levels to increase its energy, while the second ones energy is reduced. If the strength of the magnetic field and consequently the Zeeman splitting $\Delta E_{\text{Z}} = g\mu_B B$ greatly exceeds the thermal energy $k_{\text{B}}T$, the two trion spin states are well distinguishable. For a temperature of $T = 1.8$ K, the thermal energy can be calculated to 0.16 meV in comparison to Zeeman splittings in the range of $0.33 - 1.10$ meV for heavy-hole (T^-) splittings from $3 - 10$ T.
With linearly polarized optical excitation, no additional angular momentum is brought into the system, resulting in an equal population of both levels, as can be seen in the zero polarization degree in the beginning of the measurement in Fig 5-2(b). The different decay curves of the circular polarization-resolved PL indicate, that the trion spin states are emptied differently and exchanges between the states occur. After the uniform population, the spin states, in the following denoted by $\uparrow$ and $\downarrow$, tend to an equilibrium situation, which can be described by the Boltzmann distribution ($g\mu_B B/k_{\text{B}}T$), whose predominant factor is the Zeeman splitting. For an exact analysis of the time-resolved spin state population, two rate equations have to be considered:

$$\begin{aligned} \frac{dn_\uparrow}{dt} &= G_\uparrow - \frac{n_\uparrow}{\tau} - \frac{n_\uparrow}{\tau_s} + \frac{n_\downarrow}{\tau_s}\exp\left[-\frac{\Delta E}{k_{\text{B}}T}\right] \\ \frac{dn_\downarrow}{dt} &= G_\downarrow - \frac{n_\downarrow}{\tau} + \frac{n_\uparrow}{\tau_s} - \frac{n_\downarrow}{\tau_s}\exp\left[-\frac{\Delta E}{k_{\text{B}}T}\right], \end{aligned} \tag{5.2}$$

with $G_\uparrow = G_\downarrow$ for the intial pump rates into the spin states, $n_\uparrow$ and $n_\downarrow$ as a population value of the states with the spin projections of $\pm 3/2$. The value τ and τ_s stand furthermore for the trion recombination and spin relaxation time, respectively. Consequently, the intensities of the σ^+- and σ^--circularly polarized PL components are proportional to the $n_\uparrow$ and $n_\downarrow$ values. Under these preliminary

considerations the dynamical circular polarization degree arises to

$$\rho_{\mathrm{c}}(t,\tau,\tau_s) = \frac{n_{\uparrow}(t,\tau,\tau_s) - n_{\downarrow}(t,\tau,\tau_s)}{n_{\uparrow}(t,\tau,\tau_s) + n_{\downarrow}(t,\tau,\tau_s)}. \tag{5.3}$$

For detailed descriptions, the dispersive lifetime distribution, typical for (In,Al)As/AlAs QD ensembles, has to be taken into account. By using Eq. (5.3), it is possible to describe the dynamic polarization degree of one trion complex. Complicatingly, the ensemble of QDs consists of many trions, trapped in QDs with slightly different characteristics, ranging from composition to QD shape. These circumstances result in the PL emission at equal energies, but with different dynamics [18]. A complete description, including the total ensemble spin state occupation ($N^{\uparrow,\downarrow}$), requires the summation over all QDs with

$$N^{\uparrow,\downarrow}(t,\tau_s) = \int G(\tau) n_{\uparrow,\downarrow}(t,\tau,\tau_s) d\tau. \tag{5.4}$$

Accordingly, the overall circular polarization degree for the ensemble of QDs $\rho_{\mathrm{c}}(t,\tau_s)$ is given by:

$$\rho_{\mathrm{c}}(t,\tau_s) = \frac{N^{\uparrow}(t,\tau_s) - N^{\downarrow}(t,\tau_s)}{N^{\uparrow}(t,\tau_s) + N^{\downarrow}(t,\tau_s)}. \tag{5.5}$$

In Eq. (5.2), $\Delta E = |g_{\mathrm{hh}}|\,\mu_{\mathrm{B}} B$ is the Zeeman splitting energy, with the longitudinal heavy-hole g-factor g_{hh} and the Bohr magneton μ_{B}. As a free fitting parameter, τ_s is used. The experimentally gathered data of the dynamic polarization degree are plotted in Fig. 5-2(b) by black symbols. The red lines, respresent the fitting of Eq. (5.5) on the experimental data, and allows the determination of the spin relaxation times, taking into account the mentioned trion lifetime dispersion. The heavy-hole g-factor $|g_{\mathrm{hh}}|$ has been calculated to a value of 1.9, evaluated from the saturation levels of the circular polarization degree in the temperature dependence in the steady-state regime, shown as black circles in the inset of Fig. 5-3(a). The values of the saturation levels are proportional to a tangens-hyperbolic function

$$\rho_{\mathrm{c}}^{\mathrm{sat}}(T) \sim \tanh\left[|g_{\mathrm{hh}}|\,\mu_{\mathrm{B}} B/(k_{\mathrm{B}} T)\right],$$

which is depicted as a solid blue line.

The spin relaxation time has been determined both, in magnetic field and temperature dependence. The temperature dependence on the one hand, seen in Fig. 5-3(a), shows a decrease of the spin relaxation time with increasing temperatures up to 30 K. The behavior described, is best approximated using a $T^{-0.9}$ dependence. On the other hand, with increasing magnetic fields, it can be seen in Fig. 5-4(a), that a drastic decrease of τ_s takes place additionally with much stronger dependence, best decribed by $\tau_s(B) \sim B^{-5}$.

The process of spin relaxation in neutral, as well as charged exitons, typically requires both, the dissipation of momentum and energy, especially under the influence of externally applied magnetic fields. In this condition, the Zeeman effect

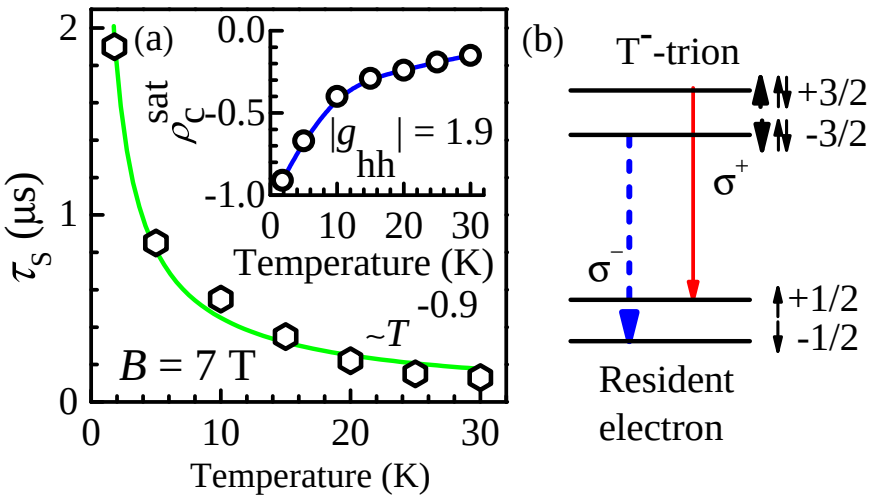

Figure 5-3: (a) Spin relaxation time as a function of temperature, measured at $B = 7$ T. The green solid line represents the best fit, giving rise to $\tau_s(T) \sim T^{-0.9}$. The inset shows the temperature dependence of the saturation level of the circular-polarization degree. A fit is shown by the solid line. (b) Spin level scheme for the T^--complex in a magnetic field shown for positive values of electron and heavy-hole g-factors [108]. The spin projection of the electron (heavy-hole) is indicated by a thin (thick) arrow. Long arrows mark optical transitions. Excited states with spin projections of $\pm 3/2$ are dominated by heavy-hole g-factors, as electron spins compensate each other. Under emission of circularly polarized light (σ^-/σ^+), the trion complex recombines, leaving behind one resident electron.

causes a splitting of the spin states, increasing the energy difference with increasing field strength. With the application of higher magnetic fields in the few Tesla range the energy differences between the spin states start to match the energy of high phonon populations. The emission or absorption of single acoustic phonons [58, 106, 107] or a two-phonon Raman process [104, 109] would allow this dissipation of energy. Responsible for the change of the trion spin could be two interactions: The spin-orbit interaction and the hyperfine interaction with the nuclear spins.

The last mentioned one can be taken as less favorable, as the interaction is mostly defined by the Fermi contact interaction. The corresponding envelope function $|\Psi(\mathbf{r}_n)|^2$ [115] is minimal for negatively charged QD, whose spin is dominated by the heavy-hole with p-type wavefunction, in contrast to the central-symmetric nuclear wave function. The spin-orbit interaction can therefore be taken as the dominant one in trion sytems with two electrons and one hole. A huge impact on the spin relaxation times in two-level systems has the ratio between the Zeeman splitting influenced by the external magnetic field strength and the thermal energy $\Delta E_Z/k_BT$ [59, 58, 104, 106, 109]. With the experimental conditions used in the measurements, $g_{hh}\mu_B B \geq k_B T$, theoretical considerations predict a magnetic field dependence of $\tau_s(B) \sim B^{-2}$ in case of two-phonon Raman process, and $\tau_s(B) \sim B^{-5}$ for one-acoustic phonon scatterings [58, 104, 57]. The experimental results correspond therefore to a spin relaxation mechanism based on spin-orbit

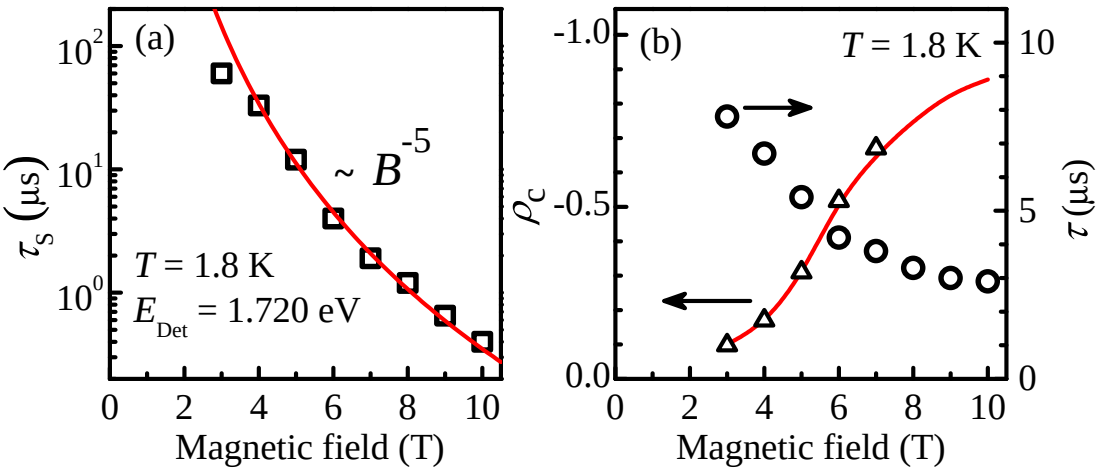

Figure 5-4: (a) Spin relaxation time τ_s as a function of magnetic field. τ_s follows a B^{-5} dependence, as indicated by the solid curve. (b) Circular polarization degree of steady-state PL as a function of magnetic field: experimental data are shown by triangles and calculation by the line. Open circles give the values of a single-trion lifetime evaluated from the simplified model.

interaction mediated by single phonons. An additional proof is given by the temperature dependence, which is consistent with this assumption, showing a decrease of τ_s proportional to $T^{-0.9}$ in comparison to a dependence of T^{-1} predicted for such a situation [43].
The inclusion of a lifetime distribution, as seen in the inset in Fig. 5-2(a), instead of a single-trion recombination time has been proven to be imperative to describe the spin relaxation in dependence on magnetic fields. In Fig. 5-4(b) the steady-state PL circular polarization degree $\rho_c(B)$ is plotted for an increasing magnetic field strength. Black triangles represent here measured data and the red line corresponds to calculations based on the solution of the rate equations (5.2) in a steady-state condition of $\frac{dn_{\uparrow,\downarrow}}{dt} = 0$.
The use of a single trion recombination time τ, as a fitting parameter to calculate the circular polarization degree following the rate equation, produces a strong magnetic field dependence. As can be seen by the black circles in Fig. 5-4(b), the fitted recombination times noticeable decrease with increasing magnetic fields. This behavior is in contradiction to the results presented in Fig. 5-1. The measured PL decays there evidently do not depend on any externally applied magnetic field. The main problem poses here the dispersive lifetimes, which require a distribution, as seen in the inset of Fig. 5-2(a), for a comprehensive description.

5.2 Spin relaxation times in the weak magnetic field regime

In the case of large magnetic fields, which has been discussed in the previous section, the spin states have been seen to be significantly split, so that the equilibrium

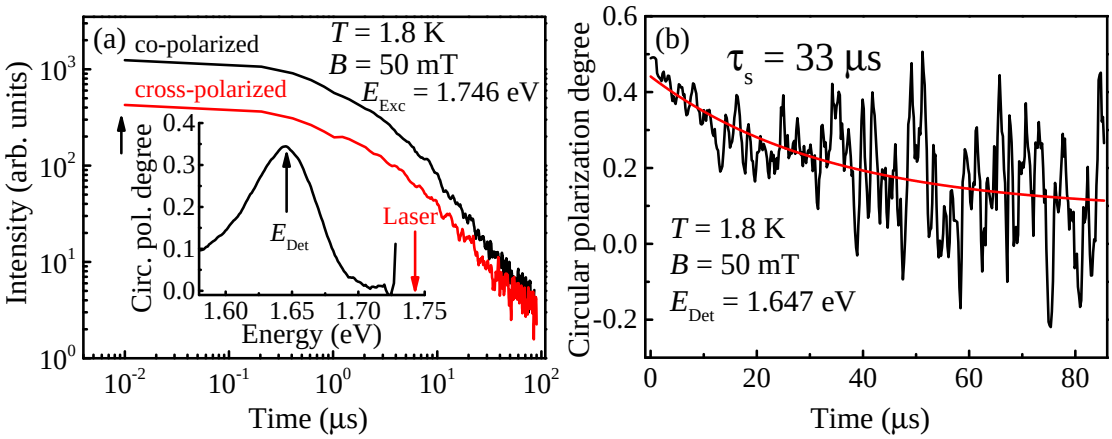

Figure 5-5: (a) Circular polarization-resolved PL decay, excited by σ^--polarized excitation at $E_{\mathrm{Exc}} = 1.746$ eV, measured at $T = 1.8$ K. The higher intensive PL decay corresponds to the co-polarized conditioned PL. The end of the excitation pulse with 1 μs pulse width ends at $t = 10$ ns. The inset illustrates the spectrally resolved circular polarization degree in the time-integrated regime. The black arrow marks the energy exhibiting the highest polarization degree, used for all following measurements. (b) Time-resolved polarization degree based on the two circular components presented in (a) taken under the influence of a small longitudinal magnetic field of $B = 50$ mT. Spin relaxation times were approximated by the fit of an exponential decay function.

condition predicts a stronger population of one spin state (mostly the lower-energy state). The major disadvantage of this method is the energy difference between the spin states, which corresponds to increased phonon population energies. These can efficiently cause a relaxation of the carrier spin states, as has been seen in Fig. 5-3 and 5-4(a).

An alternative technique to determine the spin relaxation times in semiconductor structures, is the optical orientation of single spin states. By the use of circularly polarized resonant light excitation, specific spin states, in the present case the $\pm 3/2$-states, can be directly excited. This cancels out the need of large magnetic fields influencing the Boltzmann distribution. A disadvantage of this technique are low absorption coefficients provided by the resonant excitation, requiring high excitation densities or drastically increased accumulation times in the measurements for moderate PL intensities.

In case of optically induced spin states, the spin levels do not require any spin state splitting, instead the selection rules refering to the angular momentum projection are solely important. They allow the specific excitation of the spin states. With σ^-- and σ^+-circularly polarized light excitation, the excited exciton complexes receive a pre-determined angular momentum projection corresponding to an increase of $\Delta M = \mp 1$. For the trion complexes at hand, this means an increase of the projection value from $-1/2$ to $-3/2$ with σ^--excitation or from $+1/2$ to $+3/2$ with σ^+-excitation. Recombination arising from these states have accordingly σ^-- or σ^+-polarization, respectively. As in the previous condition under linear excitation, the population of the spin states can be approximated by a circular polarization degree $\rho_{\mathrm{c}}^{\mathrm{o}}$. A postive value of $\rho_{\mathrm{c}}^{\mathrm{o}}$ corresponds here to a co-polarized

emission polarization in relation to the excitation, while negative values describe cross-polarized situations. In the inset of Fig. 5-5(a), the time-integrated optically induced circular-polarization degree is depicted, excited at $E_{\mathrm{Exc}} = 1.746$ eV with σ^--polarization. Unlike the intensity in the above-barrier excited PL spectrum in the inset of Fig. 5-1, the maximum of the circular polarization degree can be seen at an energy of $E_{\mathrm{Det}} = 1.647$ eV. Under pulsed excitation with a pulse width of 1 μs, the two spin states are initially non-equally populated, as can be seen by the polarization resolved PL decay curves in Fig. 5-5(a), which have been taken under the additional influence of a small longitudinal magnetic field of 50 mT. The magnetic field serves here to cancel out the degeneration of the spin state energies. The two components, denoted by co-polarized and cross-polarized, show significantly different PL intensities during the first μs after the excitation, but with an equal decay slope. In the time regime following, the intensities approach each other, as spin-flip events equalize the population of both spin levels. The dynamical evolution of $\rho_{\mathrm{c}}^{\mathrm{o}}$ can be calculated by the two circular polarization components, using the same equation as in the previous high magnetic field measurements in Eq. (5.3).* In contrast to ρ_{c}^{B}, the optical induced spin polarization $\rho_{\mathrm{c}}^{\mathrm{o}}$ starts at a maximal polarization degree, decreasing with the time delay. In Fig. 5-5(b), the corresponding dynamical polarization degree is illustrated, based on the polarization-resolved PL decays in Fig. 5-5(a). The high noise, that can be seen in the dynamical polarization, is the consequence of the low PL intensities at time delays exceeding 30 μs. As the spin relaxation times are expected on the μs timescale solely, the spin relaxation times have been calculated by fitting an exponential decay function $\rho_{\mathrm{c}}^{\mathrm{o}} = A_1 \exp^{-t/\tau_s}$ on the dynamical circular polarization degree. The value of A_1 describes here the maximal polarization degree shortly after the end of the excitation. The spin relaxation time τ_s has been used as the fitting parameter. The depolarization occuring at higher time delays, is heavily influenced by the noise, resulting in larger τ_s-values having a larger error, correspondingly.

In this way, the spin relaxation times of the n-doped (In,Al)As/AlAs QD sample #2104 have been determined for low magnetic fields ($0 < B < 70$ mT) in Faraday geometry and low temperatures between 1.8 and 30 K. The magnetic field dependence of the spin relaxation time is illustrated in Fig. 5-6(a) by black squares, for increasing magnetic field strength between 0 and 70 mT and at $T = 1.8$ K. In absence of external magnetic fields, the spin relaxation time is minimal with a value determined to 5.8 μs. With increasing strength of the applied magnetic field, this value increases as well, following an almost quadratic field dependence of $\tau_s \sim B^{1.9}$. At the maximal magnetic field provided by the experimental setup of $B = 70$ mT, the spin relaxation time exceeds 55 μs. This relaxation time is on the same scale as it has been seen for 3 T in the previous section. Two spin relaxation times, measured at 5 and 10 mT, are depicted by red points, instead. These exhibit statistical deviations, as they imply drastically increased τ_s-values at

*To denote the difference between optically and magnetic field induced circular polarization degree, the first one is here abbreviated by $\rho_{\mathrm{c}}^{\mathrm{o}}$ instead of ρ_{c}^{B} for the latter.

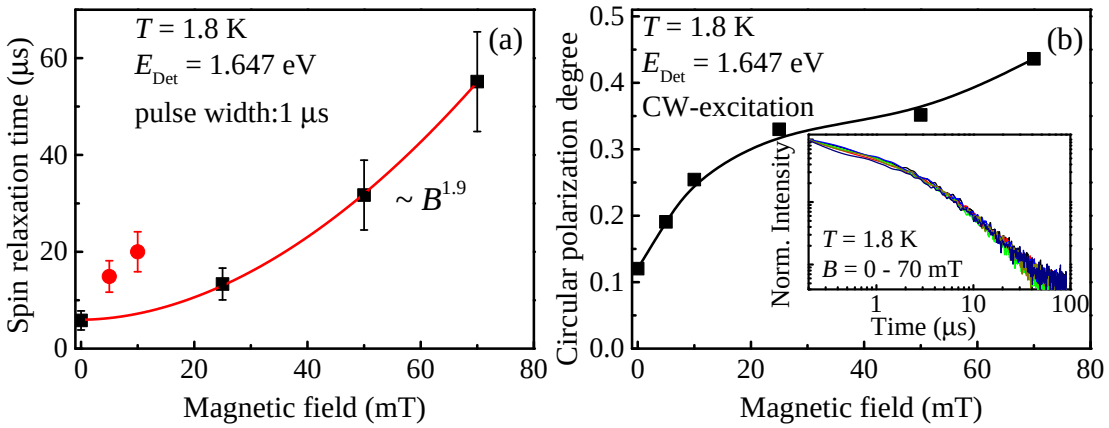

Figure 5-6: (a) Spin relaxation times in dependence of external applied magnetic fields, shown by black squares, taken at $T = 1.8$ K. Measured times, illustrated by red points, are inconsistent with additional measurements and are not further considered. The red line depicts the calculation of the magnetic fields dependence, revealing a $\tau_s \sim B^{1.9}$ dependence for the relaxation times at low magnetic fields. Increasing error bars represent the decreased signals to noise ratio for time delays exceeding 30 μs. (b) Time integrated circular polarization degree, signifying the increase of ρ_c^o with increasing field strength. The monotonic increase evidences the inconsistency of the relaxation times, depicted by red points in (a). The inset proves the absence of any PL decay acceleration with the application of magnetic fields. The PL decay curves presented, illustrate measurements taken at magnetic fields corresponding to the values in the main part of the figure, ranging from 0 to 70 mT.

very small magnetic fields, which would be followed by a decrease of τ_s at 25 mT. To decide between statistical relevant and errors in the measurement procedure, one can have an additional look at the time-integrated polarization degrees in Fig. 5-6(b) and its inset describing the PL decay at the applied magnetic fields. The inset demonstrates, that apparently no changes of the recombination time are induced by the application of small magnetic fields, indicating that for example intermixing between light- and heavy-hole states can be neglected. In the main part of the figure, the time-integrated circular polarization degree can be seen to increase consequently with increasing field strength. For small magnetic fields up to 10 mT the polarization degree increases fastly, while for further increased magnetic field strength, the rise of the polarization is reduced. The maximum of the observable polarization degree is known to depend on the ratio between the recombination time and the spin relaxation time. With constant recombination dynamics observed in the inset, the spin relaxation time has to increase monotonic with rising field strength to produce the behavior seen in the main part of the figure. This would contradict with the spin relaxation times marked by the red points in Fig. 5-6(a), as they represent a local maximum of the spin relaxation times. With an otherwise decreased value for τ_s at 25 mT, the time-integrated circular polarization degree should decrease at this magnetic field, additionally.
Under the influence of a moderate magnetic field strength of 50 mT, the temperature dependence of the spin relaxation time has been analyzed in Fig. 5-7. The

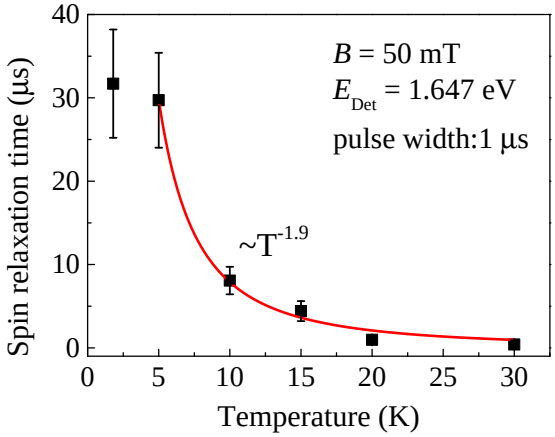

Figure 5-7: Temperature dependence of the spin relaxation time in presence of a small magnetic field of $B = 50$ mT. Measured relaxation times are presented by black squares, while the red solid line shows the fit of the almost inverse quadratic temperature dependence between 5 and 30 K. A deviation to this behavior poses the value measured at 1.8 K, indicating a possible plateau of ρ_c^o for lower temperatures.

τ_s-values have been determined in a temperature range from 1.8 to 30 K. Ignoring firstly the τ_s-value at the lowest temperature of $T = 1.8$ K, the spin relaxation times decrease drastically by non-linear means from values of 29.7 μs at $T = 5$ K down to 410 ns for $T = 30$ K. A polynomial fit, shown by the red solid line with the exponent as the fitting parameter, allows the calculation of the temperature dependence. The temperature dependence was best fitted by an exponent of $T^{-1.9}$, which is close to a quadratic decrease with the temperature. The spin relaxation time at $T = 1.8$ K poses a deviation from the observed dependence. With a value of 33 μs, it is very close to the value determined for $T = 5$ K and could be representative for a plateau of the spin relaxation times at very low temperatures ($T < 2$ K) and at weak magnetic fields.
In this regime of weak magnetic fields, the approximation of $g_{\mathrm{hh}}\mu_{\mathrm{B}}B \geq k_{\mathrm{B}}T$ is no longer valid. The spin states cannot be taken as energetically fully separated by the Zeeman splitting, as in the case of high magnetic fields. The small separation of the spin states has the consequence, that some spin relaxation mechanisms, that have been observed to be dominating previously, now can be neglected or take place with significantly reduced influence. The one-acoustic phonon mediated spin relaxation is in the presence of small magnetic fields in the mT range almost negligible, as the density of phonons matching the small Zeeman energies is small, as well. The influence of the nuclear hyperfine interaction is two-folded. Firstly, a dipole-like spin interaction between the holes and a nuclear spin bath has to be considered. This spin relaxation mechanism requires spin splitted states of both carriers and nuclei, so that its contribution at least in the absence of magnetic fields can be neglected. Secondly, the random orienation of nuclear spins in QDs can cause a fluctuation field, which can destabilize the spin orientation of

carriers.[†] Although the coupling between holes and nuclear spin system can be seen to be one order of magnitude smaller compared to electron couplings, their contribution cannot entirely be excluded [111, 112]. Finally, a two-phonon assisted Raman process can be discussed, in which the trion is excited to a virtual state by an elastic scattering with a phonon. The virtual trion state is coupled via a second phonon scattering to a final state with opposite spin projection [113]. Such a process could, for example, initially increase the trion spin state energy by a phonon absorption and reduce it subsequently by a phonon emission with slightly different energy. It has been predicted in theoretical publications [104, 58, 114] and experimental work [113], that such kind of mechanism follows a T^{-2}-dependence at temperatures exceeding 2 K and at low magnetic fields.
This behavior coincides well with the observation of the temperature dependence, presented in Fig. 5-7. The approximated temperature exponent of -1.9 is close to the predicted value of -2 for temperatures exceeding $T = 5$ K. The abberation of this dependence at a temperature of 1.8 K means, that the spin relaxation cannot be exceeded further by decreasing the temperature, but reaches a plateau. For temperatures below 5 K, an additional spin relaxation mechanism seems to dominate on a μs timescale. Furthermore, the magnetic field dependence in Fig. 5-6(a), which has been measured at $T = 1.8$ K, evidences an increase of the spin relaxation time, which is not saturated at a magnetic field of 70 mT. The observed dependence of $B^{1.9}$ does not coincide with the earlier mentioned prediction of a B^{-2}-dependence for a two phonon Raman interaction.[‡]
From the discussed processes, the hyperfine interaction between the holes and randomly oriented nuclear spin fluctuating with time is the most promissing. The fluctuation field, caused by the nuclear spin system, induces spin relaxations of the heavy-holes, especially in absence of external magnetic fields. With the application of magnetic fields, the splitting of carrier and nuclear spins increase non-equally, so that an increasing mismatch of the Zeeman energies is the result, while at the same time the nuclear spins are aligned. In the present case, this causes an increase of the longitudinal spin relaxation times. Recently it has been seen, that this relaxation process effectively can take place on a μs timescale [113], which could therefore describe the observed case as well.

5.3 Conclusion

In summary, it has been shown in the course of the two sections, that the spin relaxation times of trions in indirect (In,Al)As QDs are subject to different spin relaxation mechanisms defined by the relation between the thermal energy $k_{\mathrm{B}}T$ and the Zeeman splitting $g_{\mathrm{hh}}\mu_{\mathrm{B}}B$. The condition of $g_{\mathrm{hh}}\mu_{\mathrm{B}}B \geq k_{\mathrm{B}}T$ is given especially at high magnetic fields. There it can be seen, that τ_s follows B^{-5}- and

[†]Further insight in this spin relaxation mechanism will be given in chapter 6.

[‡]This prediction is related to the condition of $g_{\mathrm{hh}}\mu_{\mathrm{B}}B \geq k_{\mathrm{B}}T$, which is not fulfilled at the low magnetic fields used in the measurements.

T^{-1}-dependencies, correlating to an one-acoustic phonon induced spin relaxation. Furthermore, it was shown in that context, that an approach based on the solution of the rate equations in Eq. (5.2) and under consideration of dispersive lifetime distributions instead of constant τ leads to very precisely determined spin relaxation times. While on the contrary, simplified models with constant recombination times resulted in contradictory interpretations.
For low magnetic fields in the mT range, the thermal energy typically exceeds the Zeeman splitting energy. In this regime, the accounting for specific relaxation mechanisms is more difficult. As has been shown, the temperature plays the key role for the understanding in this regime. Accordingly, for higher temperatures above 5 K the two phonon assited spin relaxation seems to dominate the hole spin relaxation, leading to the observed T^{-2}-dependence. For lower temperatures, as it has been seen at $T = 1.8$ K, an interaction between the hole states and the nuclear fluctuation field causes the hole spin relaxation. The observed dependence of $\tau_s \sim B^{1.9}$ has not be predicted in the literature before, but follows qualitatively the predicted spin relaxation time stabilization with the reduced influence of the hyperfine interaction.

Chapter 6

Optically induced spin orientation of neutral excitons

In this chapter the optical orientation of indirect exciton spin in (In,Al)As QDs in the time-integrated regime will be discussed. In contrast to the magnitude of the measurements shown for example in chapter 3, 4 and 5.1, the optical orientation measurement uses circularly polarized light to excite and orientate distinct spin states in semiconductors. Despite the absence of high magnetic fields, causing a spin state splitting based on the Zeeman effect, high spin polarization will be realized. This allows to determine the origin of dominant spin-relaxation mechanisms under these conditions. As will be seen, the ensemble of QDs with direct or indirect exciton contributions will control the appearance of optical orientation effects depending on the corresponding exciton fine structure. As an exemplary structure the sample #2890 has been studied, which is identical to the one characterized in chapters 3 and 4.

6.1 High optical orientation in indirect (In,Al)As QDs

The indirect X-states in the (In,Al)As QDs are optically inaccessible and can only be populated by relaxation of electrons from energetically higher lying Γ-states or under momentum scattering. In all measurements presented in this chapter, the ensemble of QDs will be excited selectively with a Ti:Sapphire laser, resulting in the distinct PL features, as seen in Fig. 3-7 in chapter 3.2. In contrast to the previous selective excitation measurements, the excitation light is circularly polarized for the optical orientation measurements. This enables the population of distinct spin states with and without externally applied magnetic fields. As the effect of optical orientation can coincide with magnetic field induced circular polarization, one has to distinguish between both effects. The use of two opposite circularly polarized excitations and by measuring both corresponding detection polarizations allows

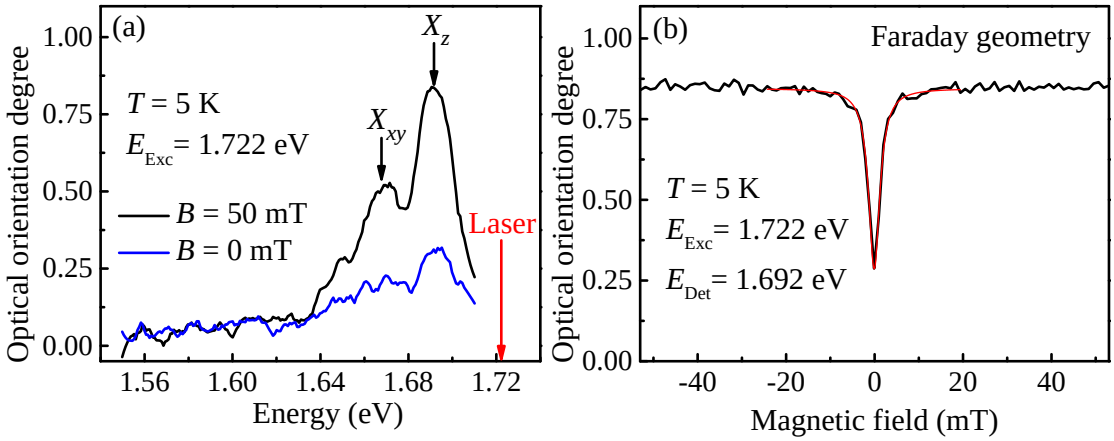

Figure 6-1: (a) Spectrally resolved optical orientation degree excited in the regime of indirect QDs at $E_{\mathrm{Exc}} = 1.722$ eV and $T = 5$ K, with and without the application of small magnetic field. Under the condition of completely compensated external magnetic fields, shown by the blue line, the indirect QD PL exhibits moderate optical orientation degrees, which is further reduced towards the regime of direct QDs. With the application of a small magnetic field in Faraday geometry, the optical orientation degree is strongly enhanced, presenting values of more than 0.8 % polarization at the spectral position of the X_z-valley denoted exciton. (b) Magnetic field dependence of the optical orientation degree for the indirect X_z-valley exciton. Smallest values of $\rho_{\mathrm{c,o}} = 0.22$ at $B = -0.08 \pm 0.02$ mT are in opposition to values exceeding $\rho_{\mathrm{c,o}} = 0.83$ with applied magnetic fields above 5 mT.

this determination. The comparison of the resulting intensities $I^{\sigma^\pm}_{\sigma^\pm}$, in which the upper index describes the excitation and the lower the detection polarization, enables the distinction of both effects, firstly by the calculation of the polarization degrees $\rho_{\mathrm{c}}^{\sigma^\pm}$:

$$\rho_{\mathrm{c}}^{\sigma^+} = \frac{I^{\sigma^+}_{\sigma^+} - I^{\sigma^+}_{\sigma^-}}{I^{\sigma^+}_{\sigma^+} + I^{\sigma^+}_{\sigma^-}} \quad , \quad \rho_{\mathrm{c}}^{\sigma^-} = \frac{I^{\sigma^-}_{\sigma^+} - I^{\sigma^-}_{\sigma^-}}{I^{\sigma^-}_{\sigma^+} + I^{\sigma^-}_{\sigma^-}}. \tag{6.1}$$

With these notations for the polarization degrees under σ^+- and σ^--circular polarization excitation, the corresponding magnetic field induced circular polarization $\rho_{\mathrm{c,B}}$ and the optical orientation degree $\rho_{\mathrm{c,o}}$ take the form*:

$$\rho_{\mathrm{c},B} = \frac{\rho_{\mathrm{c}}^{\sigma^+} + \rho_{\mathrm{c}}^{\sigma^-}}{2} \quad , \quad \rho_{\mathrm{c,o}} = \frac{\rho_{\mathrm{c}}^{\sigma^+} - \rho_{\mathrm{c}}^{\sigma^-}}{2}. \tag{6.2}$$

The different origins of circularly polarized light emission can therefore be detected and calculated. For the appearance of high optical orientation degrees the polarization degrees in Eq. (6.1) do not simply need to be large, the sign of both circular polarization degrees need to be opposite, following the excitation polarization direction. An example for this behavior can be seen in Fig. 6-1(a), in which the sample was excited by circularly polarized light with an energy of $E_{\mathrm{Exc}} = 1.722$ eV.

*For the differentiation between the optically induced circular polarization in chapter 5 and the optical orientation, the latter is denoted by $\rho_{\mathrm{c,o}}$ instead of $\rho_{\mathrm{c}}^{\mathrm{o}}$.

The sample was cooled down to a temperature of $T = 5$ K and the presence of any external magnetic field has been compensated, so that $B = 0$ mT with a reliability of ± 0.1 mT can be assured. As can be seen in Fig. 6-1(a), illustrated by the blue line, the zero-field optical orientation degree is relatively low with the maximum of $\rho_{\mathrm{c,o}} = 0.31$ at the supposed X_z-valley exciton. The second feature, at the ground state of the X_{xy}-valley exciton, shows even lower values for the optical orientation of $\rho_{\mathrm{c,o}} = 0.20$. The optical orientation degree further decreases with increasing distance to the excitation energy down to complete absence at the regime of Γ-valley excitons.
The identical measurement has been repeated with the difference of a small externally applied magnetic field of $B = 50$ mT in Faraday geometry; the optical orientation degree is shown by the black line. In presence of the small field the optical orientation degree of the QD PL drastically increases. The X_z-valley exciton denoted feature reaches values of up to $\rho_{\mathrm{c,o}} = 0.83$, while the X_{xy}-valley exiton at least reaches an optical orientation of $\rho_{\mathrm{c,o}} = 0.52$. Based on the spectral proximity of both features presented in Fig. 6-1(a), it cannot be excluded that $\rho_{\mathrm{c,o}}$ of the X_{xy}-valley is increased by an overlap with $\rho_{\mathrm{c,o}}$ stemming from the X_z-valley exciton. As in the measurement with an absent magnetic field, the optical orientation in this condition rapidly reaches zero towards the regime of direct excitons. The applied magnetic field is not strong enough to cause a magnetic field induced circular polarization, but it cancels out the degeneration of the carrier spin levels instead. Due to the significant higher polarization effect in the X_z-valley exciton, this signal will further be proceeded as being representative for the indirect excitons in the sample.
In Fig. 6-1(b) the optical orientation at the position of the X_z-valley exciton is presented in dependence on the applied magnetic field in Faraday geometry. It confirms the observation seen in the full spectra by a great extent in the way that the zero-field polarization is significantly reduced compared to those taken at small magnetic fields.[†] With the application of magnetic fields, the optical orientation degree strongly increases reaching values of $\rho_{\mathrm{c,o}} = 0.8$ and more at field strengths of only 5 mT.
The high optical orientation degree can only be achieved, if the spin relaxation time τ_s is significantly longer than the exciton recombination time τ. With excitation and orientation of a single exciton spin state by optical means, this state is therefore conserved during the complete lifetime of the corresponding indirect exciton. More surprising about the high optical orientation degree is that the X-valley excitons cannot be populated directly. Instead, an optical excitation occurs only in the direct Γ-valley excitons followed by a phonon-assisted relaxation of electrons to the indirect X-valleys. Despite the relaxation process where the momentum $\mathbf{k}$ is changed, the spin angular momentum is efficiently conserved. The high value of $\rho_{\mathrm{c,o}}$ instantly saturates and remains stable in the complete measured region of up

[†]Moreover it can be seen that the minimum of $\rho_{\mathrm{c,o}}$ is shifted to a value of $B = -0.08 \pm 0.02$ mT with $\rho_{\mathrm{c,o}} = 0.22$. The shift of the minimum can be taken as artificial, as the optical cryostat has magnetic parts inside with a magnetization resulting in a low-field strength in the order of 1 mT.

to 50 mT. The fast increase with small field strengths is best approximated by a Lorentzian function, resulting in a FWHM-value of 2.3 mT.
In difference to high magnetic field measurements, the interaction between electron and nuclear spins is increasingly important at low magnetic fields. The respective dominating effect is the Fermi contact interaction [115]:

$$H_{\mathrm{hf}} = \sum_n a_n (\boldsymbol{s}\boldsymbol{I}_n), \tag{6.3}$$

with $\boldsymbol{I}_n$ and $\boldsymbol{s}$ as the n-th nucleus and electron spin operator, respectively, and

$$a_n = V_0 A_n |\Psi(\mathbf{r}_n)|^2. \tag{6.4}$$

The unit cell volume is here described by V_0, and A_n is the hyperfine constant, which is proportional to the g-factor of the n-th nucleus. The envelope wave function $\Psi(\mathbf{r}_n)$ is devoted to the carrier system interacting with the n-th nucleus, in this case the electron in one of the X-valleys. The heavy-holes taking part in the indirect exciton complexes have a p-type wave function while nuclei are central symmetric. The envelope wave function between the two systems is close to zero and can be neglected [116].
It can be assumed that the nuclear spins are disordered in the absence of external magnetic fields. The interaction and especially the spin transfer with the electron system can therefore be taken as random. This results in the so-called nuclear spin fluctuation field B_{NF} corresponding to:

$$\left\langle B_{\mathrm{NF}}^2 \right\rangle = \frac{V_0^2 \sum_n A_n^2 |\Psi(\mathbf{r}_n)|^4 I_n(I_n+1)}{\mu_{\mathrm{B}}^2 g_{\mathrm{el}}^2} \approx \frac{B_{\mathrm{N,max}}^2}{N}. \tag{6.5}$$

The value $B_{\mathrm{N,max}}$ describes here the maximal possible magnetic field originating from the nuclei under the condition of complete and uniform polarization. Typical values of $B_{\mathrm{N,max}}$ are in the range of Tesla with QDs consisting of about 10^5 atoms, this results in fluctuation field strengths of tenth of mT [42]. For the exact calculation of the nuclear fluctuation field, an approximation following [117] can be used, in which the the sum over the unit cells or lattice nuclei is replaced by an integration leading to:

$$B_{\mathrm{NF}}^2 = \sum_j B_{\mathrm{N},j}^2 = \frac{2}{(g_{\mathrm{el}}\mu_{\mathrm{B}})^2} \frac{1}{N_{\mathrm{L}}} I_j(I_j+1) A_j^2 x_j. \tag{6.6}$$

In this expression j is the index of the nuclei type and N_{L} the number of nuclei in one unit cell volume following $N_{\mathrm{L}} = \frac{iV_{\mathrm{L}}}{V_0}$ with the number of nuclei in one unit cell, $i = 8$. As the nuclear field strength is a sum over the contribution of each alloy type, the fraction x_j is additional included in the equation for the description of the ternary alloy substitution. The localization volume V_{L} is here equal to the lens-shaped QD volume, which can be calculated by $V_{\mathrm{L}} = \frac{1}{6}\pi h(3a^2+h^2)$, with the height of the QDs $h = 3$ nm and the QD in-plane radius $a = 6$ nm. The unit cell volume

V_0 is here equal to a_0^3. The unit cell constant a_0 for the mixed $(In_x,Al_{x-1})As$ QD is taken as a linear function between the InAs and AlAs unstrained lattice constant $a_0(\mathrm{InAs}) = 0.606$ nm and $a_0(\mathrm{AlAs}) = 0.566$ nm [118] resulting for an InAs fraction of 0.3 as in the case of sample #2890 to $a_0((In_{0.3}, Al_{0.7})As) = 0.578$ nm. The number of nuclei in one QD can therefore be approximated to 7610 nuclei. Further required for the calculation of the nuclear fluctuation field strength of one alloy type is the corresponding hyperfine constant A_j.
In agreement with [117] the hyperfine constant for a reduced two-nuclei unit cell $\tilde{V}_0 = a_0^3/4$ can be approximated by

$$A_j = \frac{16\pi\mu_B\mu_j\eta_j}{3I_j\tilde{V}_0}. \tag{6.7}$$

The dimensionless electron density in proximity of the nuclei η_j has replaced in this expression the square of the electron Bloch function at n-th nucleus by $\eta_j = |u_c(\mathbf{r}_n)|^2\tilde{V}_0$. The value of μ_j in the equation describes furthermore the nuclear momentum of each of the nuclei and can be taken from Ref. [119] together with the values of the nuclear spins I_j. The three ions taking part in the ternary alloy then have $I_{\mathrm{In}} = 9/2$, $\mu_{\mathrm{In}} = 5.534$, $I_{\mathrm{Al}} = 5/2$, $\mu_{\mathrm{Al}} = 3.641$, $I_{\mathrm{As}} = 3/2$, and $\mu_{\mathrm{As}} = 1.439$. The electron density η_j for In ($\eta_{\mathrm{In}} = 6350$) and As ($\eta_{\mathrm{As}} = 4420$) have been taken from [120] and [121], while a convenient value for Al ($\eta_{\mathrm{Al}} = 1720$) has been calculated using [122]. The corresponding hyperfine constants therefore take values of $A_{\mathrm{In}} = 78.4$ μeV, $A_{\mathrm{Al}} = 25.2$ μeV, and $A_{\mathrm{As}} = 42.6$ μeV.[‡]
With these approximated values the nuclear fluctuation field contributions in Eq. (6.6) can be calculated resulting in $B_{\mathrm{NF}} = 31.1$ mT.
This estimation does unfortunately not coincide with the polarization behavior seen in Fig. 6-1(b). Despite the differences between calculation and experiment, the electron spins can be considered as constantly depolarized by the interaction with the fluctuating nuclear magnetic field reducing the spin relaxation times of the electrons drastically. With applied magnetic fields stronger than the fluctuation field, the nuclear spin system is aligned along the magnetic field axis and does not cause depolarization of the electron spin system. A secondary effect responsible for the spin relaxation is based on the spin-orbit coupling and is therefore mediated by acoustic phonons. For measurements in high magnetic fields (Tesla range) this effect is dominant, as the Zeeman splitting energy becomes equal to the energy of high acoustic phonon populations with increasing fields. With the application of small fields in the mT range, the corresponding Zeeman splitting energies are three orders of magnitude smaller and the population density of phonons matching these energies is minimal. Contradictory to that, in a condition of completely compensated magnetic fields and consequently fully degenerated spin states, the exact energy of phonons becomes less important. The phonons in this condition

[‡]The calculations performed did not take into account the isotope abundance, as the errors produced by the roughly estimated localization volume are higher than the not-considered isotope variations, which mostly concerns the ^{115}In-Isotope with a fraction of 95.7 %.

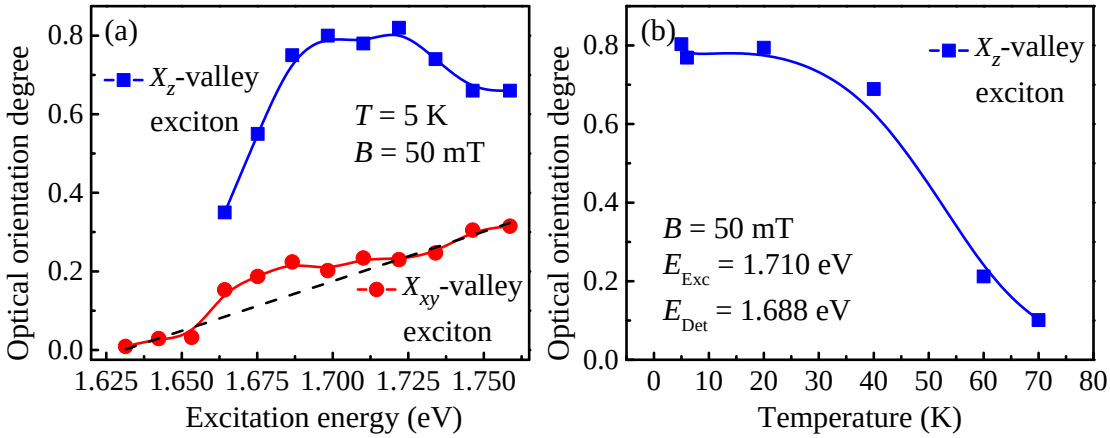

Figure 6-2: (a) Variation of the optical orientation degree with the excitation energy. The optical orientation of the X_z-valley exciton PL, shown by red points, reveals a linear increase with the excitation energy, additionally indicated by a dashed black line as a guide for the eye. Beginning at $E_{\mathrm{Exc}} = 1.675$ eV, the second PL feature emerges with significantly larger values for $\rho_{\mathrm{c,o}}$ exhibiting a non-linear behavior with increasing excitation energy. (b) Temperature dependence of the optical orientation degree for the high energy PL feature in presence of weak magnetic fields. Stable orientation values can be seen up to 40 K before the optical orientation degree decreases rapidly.

are no longer needed for the dissipation of energy, but as a mediator between the electron and lattice for the compensation of the spin.

As previously described, the transfer of electrons is a phonon-assisted relaxation process which needs to be spin conserving for achieving the high optical orientation degrees. For the relaxation, the energy $\Delta E_{\Gamma-X}$ from the Γ- to the X-state has to be dissipated. This energy can take values ranging from zero to hundreds of meV, so that the relaxation relies on both, optical phonons having a discrete energy dispersion and acoustic phonons with a continous energy dispersion. The relaxation mediated by optical phonons is limited due to their discrete energy distribution, typically requiring additional acoustic phonon mediated relaxations to populate the lowest energy conduction band states. In respect to these considerations, the transfer of the electrons and thereby of the spin state should be amplified in a condition in which the energy difference between the direct and indirect state is exactly equal to the energy of the optical phonons $\Delta E_{\Gamma-X} = E_{\mathrm{LO}}$, neglecting the need for acoustic phonons in the process. For the finding of such a resonance condition, the optical orientation has been measured at different excitation energies in Fig. 6-2(a).

For the increase of the optical orientation degree, a small magnetic field in the range of 50 mT has been applied parallel to the growth axis. The optical orientation degree of the two distinct features of the PL stemming from the X_{xy}- and supposed X_z-valley excitons are presented in the figure, which has been corrected from the background luminescence and laser stray light. The lines following the data in close proximity have been drawn as a guide for the eye only. For the ground state exciton with a X_{xy}-valley electron, depicted as red points, the optical orientation shows an almost linear behavior starting at zero polarization in

the regime of the Γ-X mixing and reaches $\rho_{\mathrm{c,o}} = 0.30$ at an excitation energy of $E_{\mathrm{Exc}} = 1.759$ eV. Corresponding to Fig. 3-7, $\Delta E_{\Gamma-X}$ reaches the value of the InAs LO phonon of 32 meV at an excitation energy of 1.675 eV. In this region a small deviation of the measured data appears on the black dashed line, which has been included as a guide for the linear increase, shifting the optical orientation degree to higher values.
The high-energy PL feature, represented by blue squares and approximated by the blue line, shows significantly higher optical orientation degrees, starting with its emergence at 1.677 eV. In difference to the first PL feature, the optical orientation in this region shows no linear dependence, but rapidly increases to a maximum of more than $\rho_{\mathrm{c,o}} = 0.80$. The initially fast increase of the optical orientation degree can at least partially be attributed to low PL intensities in the spectral regime after the emergence of this PL feature. The comparably high background in this case would artificially reduce the observable optical orientation degree. This value maintains over an excitation distance of more than 40 meV, before the value decreases again. In respect to the InAs LO phonon resonance condition, which should take place at approximately 1.726 eV, the optical orientation is actually beginning to decrease.
In conclusion, it can be observed that the optical orientation of the exciton ground state shows a small deviation from its behavior, which is unfortunately not pronounced enough to clearly speak for a resonance condition. As an explanation for the spectral behavior, two assumptions can be made. Firstly, at lower energies the electronic X-states cannot be taken as purely indirect states, but as mixed states with the direct Γ-band excitons. In this situation the spin-orbit interaction is significantly increased, thus reducing the spin relaxation time. Moreover, a mixing of heavy- and light-holes becomes possible in this direct QD regime giving rise to anisotropic exchange interaction. As a consequence, linearly polarized light can be typically seen from excitons with direct transitions [123]. Additionally, at high excitation energies $\Delta E_{\Gamma-X}$ continuously increases and finally exceeds energies which cannot be dissipated by single-phonon assisted relaxation processes. With more phonons necessary to contribute to the relaxation process the conservation of spin orientation becomes less presumable, since the scattering with lattice vibrations can change the electron spin state.
A remarkable feature observed for the effect of optical orientation in indirect excitons, is the robust temperature stability. As presented in Fig. 6-2(b), the indirect excitons have been excited with an energy of $E_{\mathrm{Exc}} = 1.710$ eV under the influence of a small external magnetic field for temperatures ranging from 5 to 70 K. Below temperatures of 40 K, the optical orientation degree is almost unchanged and decreases from values of $\rho_{\mathrm{c,o}} = 0.8$ down to 0.7. In this temperature range, the longitudinal spin relaxation time is obviously significantly longer than the exciton recombination time, following [42]:

$$P = \frac{P_0}{1 + \frac{\tau}{\tau_s}}. \tag{6.8}$$

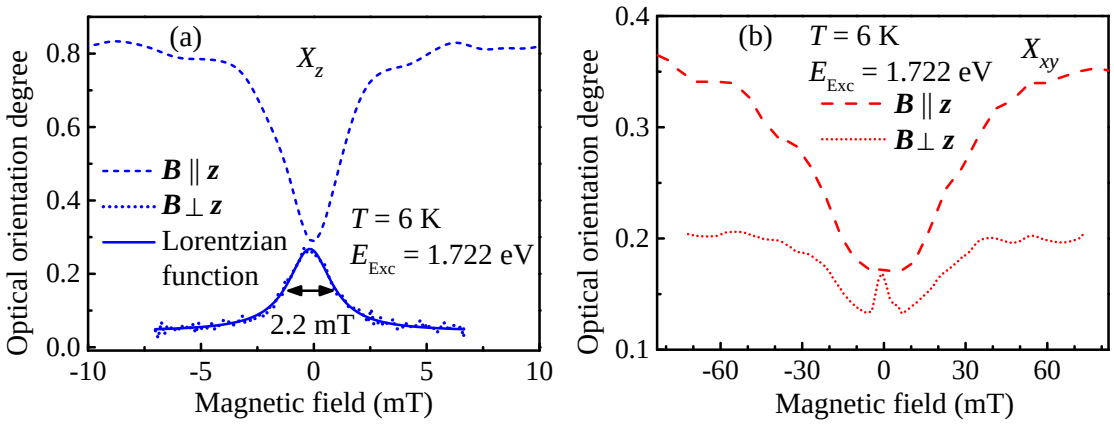

Figure 6-3: (a) Polarization and Hanle curves of the X_z-valley exciton. The dashed blue line indicates the polarization curve of the high-energy PL related optical orientation under influence of a longitudinal magnetic field ($\mathbf{B}\|\mathbf{z}$), similar to Fig. 6-1(b). Shown by the dotted blue line, is the corresponding Hanle curve, illustrating the reduction of the optical orientation under influence of transversal magnetic fields ($\mathbf{B}\perp\mathbf{z}$). The solid blue line depicts the fit based on a Lorentzian function. (b) Polarization and Hanle curves of the X_{xy}-valley exciton. The dashed red line presents polarization effect of longitudinal fields, while the dotted red line is devoted to the Hanle curve.

The equation describes the spin polarization degree P of carriers under consideration of spin relaxation τ_s and carrier recombination times τ. The value of P_0 denotes the maximal possible polarization, which apparently lies in the range above $\rho_{c,o} = 0.80$. Based on this assumption, one can assume that the spin relaxation time is not changed drastically, so that the ratio τ/τ_s is almost stable in this regime. In Fig. 3-9, the recombination time of the X_z-valley exciton has been approximated to be in the range of several hundreds of ns (82 ns and 320 ns to be exact), so that the spin relaxation time needs to be significantly longer. For temperatures exceeding 40 K, the optical orientation degree is strongly changed, speaking for a stronger accelerated spin relaxation time than accelerated recombination time.

An advanced application for the optical spin orientation is the Hanle effect [124]. This effect is based on the depolarization of the circularly polarized PL with the application of transversal magnetic fields [125], causing a precession of the optically excited electron spin around the direction of an applied magnetic field. The precession with the typical Larmor frequency $\Omega = g_B \mu_B B/\hbar$ consequently results in a reduced projection of the carrier spin along the optical axis, which defines the circular polarization. The average spin vector along the z-axis, S_z, takes in dependence on the external magnetic field the form:

$$S_z(B) = \frac{S_z(0)}{1 + (\Omega\tau^*)^2} \ . \tag{6.9}$$

The characteristic time τ^* is called the spin lifetime and consists of the spin relaxation time τ_s and the lifetime of the exciton complex τ :

$$\frac{1}{\tau^*} = \frac{1}{\tau} + \frac{1}{\tau_\mathrm{s}} \ . \tag{6.10}$$

The exciton spin lifetime also defines the width of the depolarization curve with increasing transversal magnetic field strength. In Fig. 6-3(a), the polarization curve under the influence of longitudinal fields ($\mathbf{B}\|\mathbf{z}$) and the depolarization curve caused by transversal fields ($\mathbf{B}\perp\mathbf{z}$) are depicted for the X_z-valley exciton. As in the case of the polarization curve, the depolarization curve can be best fitted by a Lorentzian function, illustrated by the solid blue line. The width of the graph has been calculated to $B_{1/2} = 2.2$ mT, which coincides well with the polarization curve width of 2.3 mT. This behavior is rather surprising, as the origin of both effects are basically different; the first being the result of the nuclear fluctuation field, and the second mostly of the precession of electron spins around the external magnetic field.[§] In Fig. 6-3(b) the polarization and depolarization curves of the X_{xy}-valley exciton are illustrated. The depolarization curve, shown by the red dashed line, exhibits a much broader polarization profile compared to the X_z-valley exciton. An approximation of this line by a Lorentzian function allows the calculation of the polarization FWHM-value to 45 mT, which is twenty times larger than in case of the X_z-valley exciton and corresponds better to the calculated nuclear fluctuation field strength of $B_\mathrm{NF} = 31.1$ mT. This allows the assumption that the interaction between the nuclear fluctuation field and excitons confined in the QDs is much stronger for the indirect excitons with electron spins aligned along the in-plane X-valleys than for those with X-valleys aligned along the z-axis. This interaction is described by the hyperfine coupling constant A_n in Eq. (6.4). An alternative explanation is given by the exciton Zeeman splitting, which is canceling the spin state degeneration with the application of external magnetic fields. The factor of about 20 is here also seen in the values of the longitudinal X_z- and X_{xy}-valley exciton g-factors, indicated in Fig. 3-8, which approximately differ by a value of 20 as well.[¶] The different influence, which the nuclear spin system has on the polarization of the exciton PL, can therefore be explained by the different longitudinal g-factors.

In the Voigt geometry, where $\mathbf{B}\perp\mathbf{z}$, the depolarization curve of the X_{xy}-valley exciton shows a more complex, two-stage behavior. The first step describes a depolarization due to precession of the carrier spins along the externally applied magnetic field. This interior stage of the Hanle curve can be calculated to have a $B_{1/2}$-value of 4.5 mT and reduces the optical orientation degree from 0.17 to 0.13. In the following an additional polarizing effect occurs, thus increasing the

[§]In fact the nuclear fluctuation field has also influence on the Hanle measurements. This influence can be seen as small in the Voigt geometry in comparison to the Faraday geometry.

[¶]The longitudinal g-factors of both exciton states have been approximated in the corresponding text, while in Fig. 3-8 the influence of the anisotropic exciton g-factor is shown in the presence of high magnetic fields at different angles of $\Theta = 0° - 70°$ with respect to the growth axis.

optical orientation degree again. It leads to a larger polarization of $\rho_{\mathrm{c,o}} = 0.2$ at field strengths above 40 mT. This untypical behavior can be attributed to two opposite effects taking place in this magnetic field regime. The Hanle effect, on the one hand, reduces the optical orientation degree already at small magnetic fields applied in transversal direction. The precession of the carrier spin around the field direction reduces the spin projection along the growth axis. In the zero-field part, the influence of the Hanle effect is absent, while its contribution to a depolarization becomes stronger in a small mT range. The increase in the optical orientation degree at stronger magnetic fields can, on the other hand, be attributed to a small angle mismatch to the Voigt geometry during the measurement. In case of a deviation from the $\Theta = 90°$ angle, a small magnetic field contribution along the Faraday geometry could cause the increase of the optical orientation degree. The effect itself can be seen as two-folded. Firstly, the spin relaxation times are extended due to the stabilization of the nuclear fluctuation field, and furthermore a linear to circular conversion can take place, reinforcing the ability to address circularly polarized exciton spin states [126]. Secondly, the mechanism can be summarized as a magnetic field induced splitting of previously linearly combined and linearly polarized exciton states into pure states with circularly polarized character. The W-like behavior, seen in the depolarization curve, can therefore be explained by a small deviation from the exact Voigt geometry.
In semiconductor structures, the half-width of the Hanle curve can be used for the determination of the carrier or exciton spin lifetime by [32]

$$\tau^* = \frac{\hbar}{g_{\mathrm{X}}\mu_{\mathrm{B}}B_{1/2}}. \tag{6.11}$$

Apart from the constants μ_{B} and $\hbar$, and the calculated Hanle curve width of $B_{1/2} = 2.2$ mT for the X_z-valley excitons, the equation consists of the exciton g-factor. In chapter 3.2 the transversal X_z-valley exciton g-factor $g_X^{\perp}$ has been approximated to a value close to zero (≈ 0.1). The corresponding spin lifetime can therefore be calculated to $\tau^* = 51.7$ ns. This surprisingly small value for the indirect exciton contradicts with the long recombination times seen in Fig. 3-9 and the observation of high optical orientation degrees for the corresponding PL, requiring spin relaxation times longer than the recombination times. Under assumption of $\frac{1}{\tau^*} \approx \frac{1}{\tau}$ and recombination times larger than 300 ns, the Hanle curve width should accordingly be six times smaller.
For the description of the very weak magnetic field regime of the X_{xy}-valley exciton in Fig. 6-3(b), the transversal exciton g-factor, which is equal to the free electron g-factor of 2.0, which has been determined in chapter 4, can be used. The corresponding spin lifetime can accordigly be calculated to $\tau^* = 1.3$ ns.
Based on the previously gathered results, it can furthermore be assumed that the spin relaxation and recombination times of the exciton ground states are in the μs-range instead being on the ns-timescale. Corresponding widths of the Hanle curves are therefore expected to be in the μT range and could, if not properly compensated, be overcome by the earth magnetic field. This would eventually

extend the maximal magnetic field resolution provided by the experimental setup.

6.2 Conclusion

In conclusion, it has been demonstrated, that the optical spin orientation provides an efficient feature for initializing single exciton spin states in QDs with indirect band gaps. From the two exciton features analyzed, the excited state, denoted to as the exciton with X_z-valley electrons, exhibits significant high optical orientation degrees. Although the population of this state underlies relaxation processes from the direct optical transition in the Γ-point, high values of the optical orientation degree have been realized. With and without the application of small magnetic fields along the assumed X_z-valleys in the mT range, the hyperfine interaction can controllable be switched on or off.
The widths of the polarization curves follows the g-factor differences between the X_{xy}- and X_z-valley excitons. Furthermore, with stabilized nuclear fields the optical orientation is almost constant up to 40 K and can still be measured up to 70 K. With the application of transversal magnetic fields for the observation of the Hanle effect, it has been shown, that the optical orientation degrees of both PL features are influenced differently. The X_z-valley exciton denoted feature presented a slim Hanle curve with a width of 2.2 mT. This value allows to approximate the spin lifetime to $\tau^* = 51.7$ ns. The optical orientation of the low-energy PL feature denoted to the X_{xy}-valley exciton, on the other hand, showed an untypical W-shape behavior with the application of a transversal magnetic field. It has been presumed, that a small tilting angle between the sample growth axis and the applied magnetic field together with a large transversal g-factor present for this exciton feature, caused a further increase of the optical orientation degree. Taking the small magnetic field part solely as the Hanle curve, the width has been determined to 4.5 mT corresponding to a spin lifetime of $\tau^* = 1.3$ ns. These calculated values unfortunately contradict with the direct observation of the exciton recombination and spin relaxation times. This leads to the conclusion, that the Hanle effect cannot be used for the approximation of carrier spin lifetimes in indirect excitons.

Chapter 7

Summary

In the scope of this thesis, indirect band gap InAs QDs in a matrix of AlAs, with X-valleys being the lowest states in the conduction band and the Γ-point as the lowest state in the valence band, have been shown to exhibit remarkable features. These cover not only typical features having all QDs in common like discrete PL lines, confinement driven control of the emission energies, seen in chapter 3, and prolonged spin relaxation times, but show additionally prolonged exciton recombination times and reduced spin-orbit interactions influencing the electron in the indirect X-valleys. The mismatch in the momentum space between electrons and holes in different symmetry points of the reciprocal lattice, have been shown to result in drastically prolonged recombination times, as seen in chapter 3.3. These can easily range into hundreds of μs and even ms, depending highly on the exact conditions during the growth process. In order to characterize the non mono-exponential PL decays observed for the indirect excitons, a phenomenological exciton lifetime distribution function has been developed. It allowed further to simulate the occurring PL decay by five orders of magnitude in time. Main characteristic limiting the maximal exciton recombination times, has been found in the thickness of the layer surrounding one QD containing material diffused from both, the QD and the surrounding matrix. In respect to the presence of such an interdiffused layer, the notation of these QDs has been changed to (In,Al)As/AlAs QDs, while the length of the corresponding layer surrounding the QDs describes effectively the heterointerface sharpness of the QD-matrix transition.
Under resonant excitation measurements, the exact energy levels of Γ- and lowest X-valley states (X_{xy}-valley) have been observed, depicting additionally the increasing energy differences between the two states with decreasing QD size. These parameters presented remarkable agreements with calculations, which had been performed prior to the experimental work. Furthermore to the expected PL features, an additional discrete feature appeared at elevated excitation energies. This feature has been seen to possess high intensities, speaking at least for an accelerated recombination time in comparison to the indirect exciton ground state. In the attempts to find the origin of this PL feature in chapter 3.2, it was observed, that this features exhibits opposite spin characteristics than the indirect exciton

ground state, having the effect of opposite circularly polarized PL in presence of external magnetic fields. Although several possible origins of this feature have been intensively discussed in that chapter, no comprehensive statement about the origin could be given. As all of the six possible origins were unable to describe all characteristics observed for this feature.
In chapter 4 the indirect excitons in the (In,Al)As QDs are examined by the technique of SFRS spectroscopy. This measuring method allows the exact determination of carrier g-factors and of their combined exciton complexes by an elastic scattering between the incident light and the corresponding carriers and exciton complexes, respectively. The energy differences between the incident light and the energy of the scattered exciton PL is equal to the Zeeman energy. By the use of this method in the range of the Γ-X mixing regime it has been revealed, that the electrons occupying one of the X-valleys along the xy-plane have g-factors almost equal to the free electron one of $g_{\mathrm{el}} = g_0 = 2.0$ and that these are highly isotropic. This means, that the value is not only equal to 2.0, but is furthermore independent from the scattering angle between the magnetic field and the sample growth axis. The large value for the electron g-factor is attributed to the large direct band gap at the X-valley of approximately more than 4 eV and the accordingly low spin-orbit interaction under this condition. In contrast to this behavior, the heavy-hole has been seen to follow a cosine-function with the scattering angles, having a value of 2.4 at $\Theta = 0\,^\circ$ and close to zero for $\Theta = 90\,^\circ$. In the same way the heavy-hole is changed with the angle, the excitons, which include the constant electron g-factor value and the anisotropic heavy-hole one, is changed as well with the difference of minimal g-factor in Faraday geometry and maximal g-factors with an opposite sign in the Voigt geometry. The comparison of the SFRS intensities under different excitation energies revealed further, that the detection of the electron spin-flip in the indirect X_{xy}-valleys only succeeded in the mixed regime of Γ- and X-valley, where the energy of both levels are almost equal. For the exact evaluation of the Γ-X-mixing point, a descriptive theory has been developed in section 4.2 allowing to describe the intensity evolution with the excitation energy.
While in chapter 4, a determination of electron and heavy-hole spin states has been achieved in the time-integrated regime, the dynamical behavior could not be observed. Spin relaxation times and the corresponding mechanisms limiting the lifetime of single spins have not been able to be observed by this technique. For the determination of spin relaxation times, a n-doped (In,Al)As QD sample has been excited by a pulsed laser in presence of external applied high magnetic fields in chapter 5.1. Pulsed excitation sources are used to induce a non-equilibrium condition between the spin states. In case of high magnetic fields with energetically split spin levels, the equilibrium condition is approximately described by a Boltzmann distribution. It depends on the Zeeman splitting and the thermal energy. The use of a linearly polarized laser pulse initially populates both spin levels equally. With typical dynamics corresponding to the spin relaxation time, the initial equal population is changed towards the equilibrium condition. The increased exciton recombination times of the indirect excitons enable simultaneously to observe this repopulation of the spin states, which is seen by the dynamical circular polariza-

tion degree. It has been found in the presence of high magnetic fields, that the spin relaxation time follow on the one hand a B^{-5} dependence with increasing magnetic fields and on the other hand a T^{-1}-dependence with the temperature. These behaviors speak for a one-phonon induced spin relaxation.
In presence of weak magnetic fields in the mT range, as shown in chapter 5.2, the splitting between the spin levels is too small for a one-phonon induced spin flip mechanism. Instead other spin relaxation mechanism dominate the spin dynamics, like the hyperfine interaction and two-phonon assisted spin relaxations. The latter has been shown to dominate at increased temperatures, starting at 5 K, while the first mentioned one is assumed to control the spin relaxation at very low temperatures around 2 K. As at these magnetic field strengths the magnetic field induced circular polarization is too small to allow the observation of a repopulation between the spin states, so that the spin states have been specifically excited by optical means. By the use of circularly polarized light, exciting and orienting single spin states, the population is reversed in comparison to the previous condition. This can be seen by the maximal circular polarization degree shortly after the excitation, which is consequently reduced by the spin relaxation processes equalizing the population of spin states, accordingly.
The use of circularly polarized light for the excitation and orientation of single exciton spin states is continued in chapter 6 for the analysis of the optical orientation of neutral excitons. To divide between magnet field induced and optically induced circular polarizations, the chapter is initiated by the description of evaluation rules allowing to separate between both effects. The two distinct PL features observed previously by selective excitation measurements, have been seen to exhibit moderate optical orientation degrees in absence of external magnetic fields. In contrast to that, with the application of very small magnetic fields in the range of mT, the optical orientation degree of the higher energy PL feature could be increased easily from values of 0.22 to values exceeding 0.8. These high optical orientation degrees have been further seen to be remarkably temperature robust, keeping equal values up to 40 K and only slowly decrease at higher temperatures. The high dependence of the optical orientation degree on small scale magnetic fields revealed further, that in this regime, the nuclear hyperfine interaction influences the spin relaxation dominantly.
In the attempt to determine the spin lifetime of both PL features, Hanle measurements have been performed. These unfortunately could not give consistent results, as the approximated spin lifetimes contradicted with the previously gathered data. The reason for these inconsistent results, are still unknown and require further investigation.

Chapter 8

Outlook

The indirect band gap (In,Al)As QDs have been intensively studied in the last years and many unique characteristics have been observed in these structures, ranging from increased exciton lifetimes to high optical orientation degrees. Nevertheless, many aspects in these structures are still undetermined and require further measurements or theoretical approaches for the understanding. Among these is the finalizing of the origin of the higher energy PL feature. Additional, the spin relaxation times of neutral and p-doped (In,Al)As QDs are object of future studies.
Apart from the indirect band gap structures with electrons in one of the X-valleys, novel structures have already undergone preliminary studies, having the electrons confined in one of the 8 degenerated L-valleys. Especially SbAs structures with reduced dimensionality are here promising candidates.

8.1 Spin dynamics of the discrete PL features in undoped structures

One of the characteristics seen for undoped structures are the discrete PL features appearing under selective excitation of the QD ensemble. As these features are shifted from each other by more than 26 meV, the separated analysis of the PL feature´s recombination and spin relaxation times should be easily achieved. Unfortunately, the excitation sources used up to now are based on an optical chopping of the continuous wave laser emission into small time regimes of emission and long dark times. As a result, the excitation conditions used with typical repetition frequencies of 1 kHz and 100 ns to 1 μs pulse duration reduce the average excitation power by factors of 10^{-3} to 10^{-4}. The resulting excitation power has been seen to be too low to study the spin dynamics of both features under the same excitation conditions. The use of pulsed excitation sources, like Q-switched lasers with variable emission energies could solve this problem ultimately, as the excitation densities within one pulse are significantly higher.
With an obtained excitation source fitting to the requirements for the measure-

ments, the spin dynamics of both PL features should be accessible by both magnetic field induced circular polarization or the optically excited optical orientation. The information gathered by this technique will give an increased insight into the different spin and recombination processes of the two distinct PL features. This will further strengthen the possibility to distinguish between the possible origins of the high energy PL feature.

8.2 Recombination and spin dynamics of neutral excitons in (In,Al)As QDs under consideration of dark states

As described in the theory in chapter 1.2, the combination of heavy-holes and electrons allows the formation of four excitons states with angular momentum projections of $M = \pm 1$ and ± 2. The influence of dark excitons with $M = \pm 2$ has up to now not been discussed in this thesis, as it is object to actual research. It has been seen in recent experiments, that in specific magnetic fields, the dark excitons might be contributing to the radiative recombination and therefore appear in the PL decay curves with an additional very long-living decay. In general, this behavior speaks for the crossing of bright and dark exciton states at specific magnetic fields, in which the Zeeman split states become equal in energy, as it is depicted in Fig. 8-1(b). In this crossing condition, spin polarized carriers stemming from dark exciton states could be given a channel for radiative recombination via bright exciton states. The radiative recombination can be typically taken as more efficient and faster. This effect has the additional consequence, that in the dynamical circular polarization degree a crossing from positive to negative polarization degrees may occur. This effect is subject to the assumption, that different timescales for the recombination τ, spin relaxation between bright states τ_s and finally between bright and dark states τ_{bd} are present. As previously seen, τ needs to be longer for the complete observation of the spin relaxation. A redistribution of carriers caused by the mixing of bright and dark states can lead to prolonged populations of the higher in energy lying bright exciton state. As an example for this phenomenon, the time-resolved magnetic field induced circular polarization has been illustrated in Fig. 8-1(a), taken in a tilted geometry of $\Theta = 45°$ and at a magnetic field of $B = 7$ T. The tilting of the geometry causes an increase of the mixing between bright and dark states, making the crossing of the polarization degree directions more pronounced and easier to observe.

The spin relaxation times of neutral excitons have been previously determined by a first approximation in the thesis of J. Debus [99] without consideration of the influence of dark exciton states. Already without this consideration, the same dependencies of $\tau_s \sim B^{-5}$ and $\tau_s \sim T^{-1}$ have been observed as in chapter 5 for negatively charged excitons. With dark exciton states considered, the determination of spin relaxation times of bright exciton states can be expected to be further

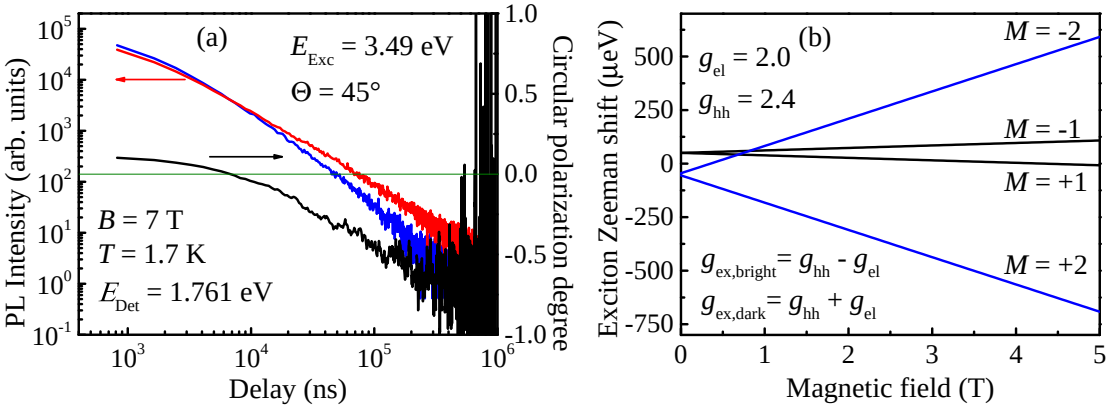

Figure 8-1: (a) PL and polarization dynamics of neutral excitons in indirect band gap (In,Al)As QDs in tilted geometry of $\Theta = 45°$. (b) Calculated fine structure splitting for bright and dark exciton states in presence of external applied magnetic fields.

improved. A challenging aspect of this advanced work poses the numerical solution of four instead of the previous two rate equations in chapter 5, while the four rate equation are extended by the bright-dark state mixing term.

For a full understanding of the factors limiting the spin lifetimes in indirect band gap (In,Al)As QDs, a similar work as in chapter 5 has to be conducted in p-doped QDs, so that the spin states of positively charged excitons are dominated by a single electron. In this way, a comparison between n- and p-doped structures would give a completed overview about the spin dynamics in indirect QDs. Up to date, the p-doping performed by the implantation of beryllium caused a strongly accelerated recombination time, neglecting the possibility to observe the population dynamics between the spin split states. An exchange of the doping material could therefore prevent the acceleration of the recombination.

8.3 Recombination and spin dynamics in indirect low-dimensional structures with lowest conduction band states in the L-valleys

With the experience gathered in the fabrication and observation of indirect band gap (In,Al)As QDs with electrons in the indirect X-valleys, attempts have been made to produce low-dimensional structures containing other indirect transitions. A logical choice for structures with fcc lattice are the conduction band states with L-valley symmetry-points. Excitons in these structures would accordingly be composed of electrons in the L-valleys, while heavy-holes are left in the valence band Γ-point. As the L-valley states can be found at the edges of the Brillouin zone either, the corresponding mismatch in the momentum space between conduction and valence band states is similar to the indirect excitons, that have been analyzed

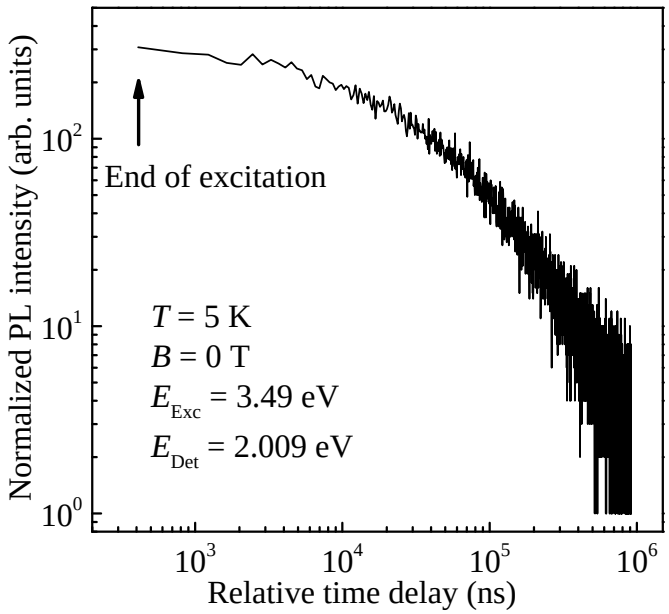

Figure 8-2: PL dynamics of exciton complexes in indirect band gap InSb QDs.

in this work. Indium antimonide QDs embedded in a matrix of AlAs are promising candidates for the realization of indirect L-valley electron excitons. Preliminary measurements performed on these structures have shown that the grown structures have extended lifetimes comparable to X-valley exciton structures, as seen in Fig. 8-2. The growing process still requires some improvements, as impurities of other materials influence the PL and its decay dynamics. The L-valley excitons in contrast to the X-valley excitons are more difficult to construct and analyze due to their alignment along the (111)-axis, which are not parallel to the macroscopic sample axis. Especially calculations approximating the energy levels of the 8 L-valleys, which are degenerated in a bulk crystal, are expected to be challenging, as the non-uniform confinement in self-assembled QDs will shift these conduction band states differently.

Bibliography

[1] J. C. Maxwell. *On physical lines of force.* Phil. Mag. **21**&**23**, p.161-175, p.281-291, p.338-348 (1861).

[2] J. E. Lilienfeld. *Method and apparatus for controlling electric current.* U.S. Patent 1745175 Canada (1925).

[3] L. Esaki and R. Tsu. IBM J. Res. Develop. **14**, 61 (1970).

[4] C. Weisbuch. Semiconductor and Semimetals, vol. 24, Academic Press Inc., New York (1987).

[5] D. A. B. Miller, D. S. Chemla,D. J. Eilenberger, P. W. Smith, A. C. Gossard, and W. T. Tsang. Appl. Phys. Lett. **41**, 679 (1982).

[6] D. S. Chemla, T. C. Damen, D. A. B. Miller, A. C. Gossard, and W. Wiegmann. Appl. Phys. Lett. **42**, 864 (1983).

[7] P. Zeeman. *The effect of magnetisation on the nature of light emitted by a substance.* Nature **55**, 347 (1897).

[8] L. H. Thomas. *The motion of the spinning electron.* Nature **117**, 514 (1926).

[9] J. Stolze and D. Suter. *Quantum Computing. A Short Course from Theory to Experiment.* Wiley-VCH Verlag, Weinheim (2008).

[10] P. Dawson, C. T. Foxon, and H. W. van Kesteren. Semicond. Sci. Technol. **5**, 54 (1990).

[11] P. Dawson, Z. Ma, K. Pierz, and E. O. Göbel. Appl. Phys. Lett. **81**, 2349 (2002).

[12] P. Dawson, E. O. Göbel, and K. Pierz. J. Appl. Phys. **98**, 013541 (2005).

[13] T. S. Shamirzaev, A. M. Gilinsky, A. K. Bakarov, A. I. Toropov, D. A. Ténné, K. S. Zhuravlev, C. von Borczyskowski, and D. R. T. Zahn. JETP Lett. **77**, 389 (2003).

[14] T. S. Shamirzaev, A. M. Gilinsky, A. K. Kalagin, A. V. Nenashev, and K. S. Zhuravlev. Phys. Rev. B **76**, 155309 (2007).

[15] T. S. Shamirzaev, A. V. Nenashev, A. K. Gutakovskii, A. K. Kalagin, K. S. Zhuravlev, M. Larsson, and P. O. Holtz. Phys. Rev. B **78**, 085323 (2008).

[16] T. S. Shamirzaev, A. V. Nenashev, and K. S. Zhuravlev. Appl. Phys. Lett. **92**, 213101 (2008).

[17] T. S. Shamirzaev, D. S. Abramkin, D. V. Dmitriev, and A. K. Gutakovskii. Appl. Phys. Lett. **97**, 263102 (2010).

[18] T. S. Shamirzaev, J. Debus, D. S. Abramkin, D. Dunker, D. R. Yakovlev, D. V. Dmitriev, A. K. Gutakovskii, L. S. Braginsky, K. S. Zhuravlev, and M. Bayer. Phys. Rev. B **84**, 155318 (2011).

[19] D. Dunker, T. S. Shamirzaev, J. Debus, D. R. Yakovlev, K. S. Zhuravlev, and M. Bayer. Appl. Phys. Lett. **101**, 142108 (2012).

[20] J. Debus, T. S. Shamirzaev, D. Dunker, V. F. Sapega, E. L. Ivchenko, D. R. Yakovlev, K. S. Zhuravlev, and M. Bayer. *Fine structure of* Γ*-X mixed exciton in indirect band-gap (In,Al)As/AlAs quantum dots determined by spin-flip Raman scattering.* To be published.

[21] G. Kirchhoff. *Über die Fraunhofer'schen Linien.* Annalen der Physik **185** (1), p.148 (1860). And: G. Kirchhoff. *Über das Verhältniss zwischen dem Emissionsvermögen und dem Absorptionsvermögen der Körper für Wärme und Licht.* Annalen der Physik **185** (2), p.275 (1860).

[22] M. Born and R. Oppenheimer. *Zur Quantentheorie der Molekeln.* Annalen der Physik **389**, p. 457 (1927).

[23] G. Czychol. *Theoretische Festkörperphysik.* Springer Verlag, Berlin (2004).

[24] J. Frenkel. *On the Transformation of light into Heat in Solids. I.* Phys. Rev. **37**, 17 (1931).

[25] G. H. Wannier. *The Structure of Electronic Excitation Levels in Insulating Crystals.* Phys. Rev. **52** (3), 191 (1937).

[26] V. A. Shchukin, N. N. Ledentsov, and D. Bimberg. *Epitaxy of nanostructures.* Springer Verlag, Berlin (2004).

[27] G. F. Bassani and G. Pastori-Parravicini. *Electronic States and Optical transitions in Solids.* Pergamon Press, Oxford (1975).

[28] M. Sugawara. *Self-Assembled InGaAs/GaAs Quantum Dots.* Semiconductors and Semimetals, Academic Press Inc., vol. 60 (1999).

[29] S. Raymond, S. Studenikin, A. Sachrajda, Z. Wasilewski, S. J. Cheng, W. Sheng, P. Hawrylak, A. Babinski, M. Potemski, G. Ortner, and M. Bayer. Phys. Rev. Lett. **92**, 187402 (2004).

[30] P. Hawrylak. Phys. Rev B **60**, 5597 (1999).

[31] J. Venables. *Introduction to Surface and Thin Film Processes*. Cambridge University Press, Cambridge (2000).

[32] Y. G. Kusrayev. Semicond. Sci. Technol. **23**, 114013 (2008).

[33] L. E. Brus, Al. L. Efros, and T. Itoh. *Spectroscopy of Isolated and Assembled Semiconductor Nanocrystals*. J. Luminescence **70**, p.1-484 (1996).

[34] P. Y. Yu and M. Cardona. *Fundamentals of Semiconductors, Physics and Materials Properties*. Springer-Verlag, Heidelberg 4th Edition (2010).

[35] M. Bayer, G. Ortner, O. Stern, A. Kuther, A. A. Gorbunov, A. Forchel, P. Hawrylak, S. Fafard, K. Hinzer, T. L. Reinecke, S. N. Walck, J. P. Reithmaier, F. Klopf, and F. Schäfer. Phys. Rev. B **65**, 195315 (2002).

[36] I. A. Yugova, A. Greilich, D. R. Yakovlev, A. A. Kiselev, M. Bayer, V. V. Petrov, Yu. K. Dolgikh, D. Reuter, and A. D. Wieck. Phys. Rev. B **75**, 245302 (2007).

[37] E. L. Ivchenko and G. E. Pikus. *Superlattices and other Heterostructure. Symmetry and Optical Phenomena*. Spinger Verlag, Berlin (1995).

[38] M. Bayer, A. Kuther, A. Forchel, A. Gorbunov, V. B. Timofeev, F. Schäfer, J. P. Reithmaier, T. L. Reinecke, and S. N. Walck. Phys. Rev. Lett. **82**, 1748 (1999).

[39] J. Debus, D. Dunker, V. F. Sapega, D. R. Yakovlev, G. Karczewski, T. Wojtowicz, J. Kossut, and M. Bayer. Phys. Rev. B **87**, 205316 (2013).

[40] C. Kittel. *Introduction to Solid State Physics*. John Wiley & Sons, 8th Edition (2004).

[41] J. H. Davies. *The Physics of Low-Dimensional Semiconductors. An introduction*. Cambridge University Press, Cambridge (1997).

[42] M. I. D'yakonov. *Spin physics in semiconductors*. Springer-Verlag, Berlin (2008).

[43] M. W. Wu, J. H. Jiang, and M. Q. Weng. *Spin dynamics in semiconductors*. Physics Reports **493**, p.61-236 (2010).

[44] G. E. Pikus and A. N. Titkov. *Spin relaxation under optical orientation in semiconductors* in [56], p. 73-132.

[45] Y. Yafet. Solid State Physics, vol. **14**, p.1-98. Academic Press Inc., New York (1963).

[46] R. J. Elliott. *Theory of the effect of spin-orbit coupling on magnetic resonance in some semiconductors*. Phys. Rev. **96**, 266 (1954).

[47] F. Simon, B. Dóra, F. Murányi, A. Jánossy, S. Garaj, L. Forró, S. Bud'ko, C. Petrovic, and P. C. Canfield. Phys. Rev. Lett. **101**, 177003 (2008).

[48] J. Fabian and S. Das Sarma. *Spin relaxation of conduction electrons*. Journal of vacuum Science and Technology B: Microelectronics and nanometer structures **17** (4), 1708-1715 (1999).

[49] F. Beuneu and P. Monod. Phys. Rev. B **18**, 2422 (1978).

[50] P. Monod and F. Beuneu. Phys. Rev. B **19**, 911 (1979).

[51] M. I. D'yakonov, V. I. Perel. Zh. Eksp. Teor. Fiz. **60**, 1954 (1971).

[52] M. I. D'yakonov, V. I. Perel. Fiz. Tverd. Tela **13**, 3581 (1971).

[53] C. Grimaldi. Phys. Rev. B **72**, 075307 (2005).

[54] R. T. Harley. *Spin dynamics of free carriers in quantum wells*, in [42], pp. 29-52.

[55] W. J. H. Leyland, R. T. Harley, M. Henini, A. J. Shields, I. Farrer, and D. A. Ritchie. Phys. Rev. B **76**, 195305 (2007).

[56] F. Meier and B. P. Zakharchenya. *Optical Orientation*. North-Holland, Amsterdam (1984).

[57] L. M. Woods, T. L. Reinecke, and Y. Lyanda-Geller. Phys. Rev B **66**, 161318 (2002).

[58] A. V. Khaetskii and Y. V. Nazarov. Phys Rev B **64**, 125316 (2001).

[59] A. V. Khaetskii and Y. V. Nazarov. Phys Rev B **61**, 12639 (1999).

[60] V. K. Kalevich, K. V. Kavokin, and I. A. Merkulov. *Dynamic Nuclear Polarization and Nuclear Fields*, in [42], p.308-346.

[61] A. Abragam and B. Bleaney. *Electron Paramagnetic Resonance of Transition Ions*. Oxford University Press, Oxford (1970).

[62] Technical TriVista system manual, Version 1.A. Princeton Instruments, Trenton (2005).

[63] Technical Ramanor U1000 monochromator manual, Version 3. Jobin Yvon (1988).

[64] O. Svelto. *Principles of Lasers*. Plenum Press, New York and London (1989).

[65] S. Sanguinetti, M. Guzzi, and M. Gurioli. *Characterization of Semiconductor Heterostructures and Nanostructures*, p.175-208, edited by C. Lamberti and G. Agostini. Elsevier science, Amsterdam (2008).

[66] H. Lüth. *Solid Surfaces, Interfaces and Thin Films*. Springer-Verlag, Berlin (2001).

[67] M. R. Brozel and G. E. Stillman. *Properties of Gallium Arsenide* (3rd Edition). INSPEC, p. 291, London (1996).

[68] T. Obata, S. Fukushima, T. Araya, and N. Otsuk. *Photoluminescence of nearly stoichiometric LT-GaAs and LT-GaAs/AlAs MQW*. Journal of Crystal Growth vol. 227-228, p. 112-116 (2001).

[69] P. Hawrylak, G. A. Narvaez, M. Bayer and A. Forchel. Phys. Rev. Lett. **85**, 389 (2000).

[70] S. Spatzek, A. Greilich, S. E. Economou, S. Varwig, A. Schwan, D. R. Yakovlev, D. Reuter, A. D. Wieck, T. L. Reinecke, and M. Bayer. Phys. Rev. Lett. **107**, 137402 (2011).

[71] S. H. Wei and A. Zunger. Appl. Phys. Lett. **72**, 2011 (1998).

[72] I. Vurgaftman, J. R. Meyer, and L. R. Ram-Mohan. J. Appl. Phys. **89**, 5815 (2001).

[73] P. Lawaetz. Phys. Rev. B **4**, 3460 (1971).

[74] J.-Y. Marzin, J.-M. Gérard, A. Izraël, D. Barrier, and G. Bastard. Phys Rev. Lett. **73**, 716 (1994).

[75] Al. L. Efros, M. Rosen, M. Kuno, M. Nirmal, D. J. Norris, and M. Bawendi. Phys. Rev. B **54**, 4843 (1996).

[76] F. Liu, L. Biadala, A. V. Rodina, D. R. Yakovlev, D. Dunker, C. Javaux, J. -P. Hermier, A. L. Efros, B. Dubertret, and M. Bayer. Phys. Rev. B **88**, 035302 (2013).

[77] J. R. Chelikowsky and M. L. Cohen. Phys. Rev. B **14**, 556 (1976).

[78] L. M. Roth, B. Lax, and S. Zwerling. *Theory of Optical Magneto-Absorption Effects in Semiconductors*. Phys. Rev. **114**, 90 (1959).

[79] S. Emura, T. Nakagawa, S. Gonda, and S. Shimizu. J. Appl. Phys. **62**, 4632 (1987).

[80] M. Grundmann, O. Stier, and D. Bimberg. Phys. Rev. B **52**, 11969 (1995).

[81] R. Heitz, M. Veit, N. N. Ledentsov, A. Hoffmann, D. Bimberg, V. M. Ustinov, P. S. Kop'ev, and Zh. I. Alferov. Phys. Rev. B **56**, 10435 (1997).

[82] J.-W. Luo, A. Franceschetti, and A. Zunger. Phys. Rev. B **78**, 035306 (2008).

[83] N. N. Ledentsov, J. Böhrer, M. Beer, F. Heinrichsdorff, M. Grundmann, D. Bimberg, S. V. Ivanov, B. Ya. Meltser, S. V. Shaposhnikov, I. N. Yassievich, N. N. Faleev, P. S. Kop'ev, and Zh. I. Alferov. Phys. Rev. B **52**, 14058 (1995).

[84] N. G. Romanov and P. G. Baranov. Nanotechnology **12**, 585 (2001).

[85] C. R. Pidgeon, D. L.Mtchell, and R. N. Brown. Phys. Rev. **154**, 737 (1967).

[86] M.-Z. Hunag and W. Y. Ching. J. Phys. Chem. Solids **46**, 977 (1985).

[87] L. W. Molenkamp, R. Eppenga, G. W. 't Hooft, P. Dawson, C. T. Foxon, and K. J. Moore. Phys. Rev. B **38**, 4314 (1988).

[88] V. Troncale, K. F. Karlsson, E. Pelucchi, A. Rudra, and E. Kapon. Appl. Phys. Lett. **91**, 241909 (2007).

[89] V. Zwiller, M. -E. Pistol, D. Hessman, R. Cederström, W. Seifert, and L. Samuelson. Phys. Rev. B **59**, 5021 (1999).

[90] T. Berstermann, T. Auer, H. Kurtze, M. Schwab, D. R. Yakovlev, M. Bayer, J. Wiersig, C. Gies, F. Jahnke, D. Reuter, and A. D. Wieck. Phys. Rev. B **76**, 165318 (2007).

[91] J. C. Phillips. Rep. Prog. Phys. **59**, 1133 (1996).

[92] O. Guillois, N. Herlin-Boime, C. Reynaud, G. Ledoux, and F. Huisken. J. Appl. Phys. **95**, 3677 (2004).

[93] A. F. van Driel, I. S. Nikolaev, P. Vergeer, P. Lodahl, D. Vanmaekelbergh, and W. L. Vos. Phys. Rev. B **75**, 035329 (2007).

[94] A. Siemiarczuk, B. D. Wagner, and W. R. Ware. J. Phys. Chem. **94**, 1661 (1990).

[95] A. M. Kapitonov, A. P. Stupak, S. V. Gaponenko, E. P. Petrov, A. L. Rogach, and A. Eychmüller. J. Phys. Chem. B **103**, 10109 (1999).

[96] C. Delerue, G. Allan, C. Reynaud, O. Guillois, G. Ledoux, and F. Huisken. Phys. Rev. B **73**, 235318 (2006).

[97] I. S. Nikolaev, P. Lodahl, A. F. van Driel, A. F. Koenderink, and W. L. Vos. Phys. Rev. B **75**, 115302 (2007).

[98] L. D. Landau, and E. M. Lifshitz. *Statistical Physics*. Pergamon Press, New York, (1980).

[99] J. Debus. *Spin-flip Raman scattering in low-dimensional semiconductors*. Sierke Verlag, (2012).

[100] M. I. D'yakonov, X. Marie, T. Amand, P. Le Jeune, D. Robart, M. Brousseau, and J. Barrau. Phys. Rev. B **56**, 10412 (1997).

[101] C. F. Young, E. H. Poindexter, G. J. Gerardi, W. L. Warren, and D. J. Keeble. Phys. Rev. B **55**, 16245 (1997).

[102] E. E. Vdovin, Yu. N. Khanin, L. Eaves, M. Henini, and G. Hill. Phys. Rev. B **71**, 195320 (2005).

[103] I. Toft and R. T. Phillips. Phys. Rev B **76**, 033301 (2007).

[104] M. Trif, P. Simon, and D. Loss. Phys. Rev. Lett. **103**, 106601 (2009).

[105] D. Bimberg, M. Grundmann, and N. N. Ledentsov, *Quantum Dot Heterostructures*. John Wiley & Sons, New York (1999).

[106] M. Kroutvar, Y. Ducommun, D. Heiss, M. Bichler, D. Schuh, G. Abstreiter, and J. J. Finley. Nature **432**, 81 (2004).

[107] D. Heiss, S. Schaeck, H. Huebl, M. Bichler, G. Abstreiter, J. J. Finley, D. V. Bulaev, and D. Loss. Phys. Rev. B **76**, 241306(R) (2007).

[108] G. Bartsch, M. Gerbracht, D. R. Yakovlev, J. H. Blokland, P. C. M. Christianen, E. A. Zhukov, A. B. Dzyubenko, G. Karczewski, T. Wojtowicz, J. Kossut, J. C. Maan, and M. Bayer. Phys. Rev. B **83**, 235317 (2011).

[109] C. Lü, J. L. Cheng, and M. W. Wu. Phys. Rev. B **71**, 075308 (2005).

[110] T. Yokoi, S. Adachi, H. Sasakura, S. Muto, H. Z. Song, T. Usuki, and S. Hirose. Phys. Rev. B **71**, 041307 (2005).

[111] B. Eble, C. Testelin, P. Desfonds, F. Bernardot, A. Balocchi, T. Amand, A. Miard, A. Lemaître, X. Marie, and M. Chamarro. Phys. Rev. Lett. **102**, 146601 (2009).

[112] E. A. Chekhovich, A. B. Krysa, M. S. Skolnick, and A. I. Tartakovskii. Phys. Rev. Lett. **106**, 027402 (2011).

[113] F. Fras, B. Eble, P. Desfonds, F. Bernardot, C. Testelin, M. Chamarro, A. Miard, and A. Lemaître. Phys. Rev. B **86**, 045306 (2012).

[114] H. Wei, M. Gong, G.-C. Guo, and L. He. Phys. Rev. B **85**, 045317 (2012).

[115] A. Abragam. *Principles of Nuclear Magnetism*. Clarendon Press, Oxford (1961).

[116] E. I. Gryncharova and V. I. Perel. Sov. Phys. Semicond. **11**, 997 (1977).

[117] M. Syperek, D. R. Yakovlev, I. A. Yugova, J. Misiewicz, I. V. Sedova, S. V. Sorokin, A. A. Toropov, S. V. Ivanov, and M. Bayer. Phys. Rev. B **84**, 085304 (2011).

[118] C. G. Van de Walle. Phys. Rev. B **39**, 1871 (1989) .

[119] D. E. Gray. *American Instutute of Physics Handbook*, 3rd ed. McGraw-Hill Book Company, New York (1972).

[120] A. Nakamura, D. Paget, C. Hermann, C. Weisbuch, G. Lampel, and B. C. Cavenett. Solid State Commun. **30**, 411 (1979).

[121] D. Paget, G. Lampel, B. Sapoval, and V. I. Safarov. Phys. Rev. B **15**, 5780 (1977).

[122] J. R. Morton and K. F. Preston. Journ. of Magn. Res. **30**, 577 (1978).

[123] C. Gourdon and P. Lavallard. Phys. Rev. B **46**, 4644 (1992).

[124] W. Hanle. Z. Phys. **30**, 93 (1924).

[125] R. W. Wood and A. Ellett. Phys. Rev. **24**, 243 (1924).

[126] R. I. Dzhioev, H. M. Gibbs, E. L. Ivchenko, G. Khitrova, V. L. Korenev, M. N. Tkachuk, and B. P. Zakharchenya. Phys. Rev. B **56**, 13405 (1997).

List of publications

(i) J. Debus, A. A. Maksimov, D. Dunker, D. R. Yakovlev, I. I. Tartakovskii, A. Waag, and M. Bayer. *Dynamical control of Mn spin-system cooling by photogenerated carriers in a (Zn,Mn)Se/BeTe heterostructures.* Phys. Rev. B **82**, 085448 (2010).

(ii) A. Pawlis, T. Berstermann, C. Brüggemann, M. Bombeck, D. Dunker, D. R. Yakovlev, N. A. Gippius, K. Lischka, and M. Bayer. *Exciton states in shallow ZnSe/(Zn,Mg)Se quantum wells: Interaction of confined and continuum electron and hole states.* Phys. Rev. B **83**, 115302 (2011).

(iii) T. S. Shamirzaev, J. Debus, D. S. Abramkin, D. Dunker, D. R. Yakovlev, D. V. Dmitriev, A. K. Gutakovskii, L. S. Braginsky, K. S. Zhuravlev, and M. Bayer. *Exciton recombination dynamics in an ensemble of (In,Al)As/AlAs quantum dots with indirect band-gap and type-I band alignment.* Phys. Rev. B **84**, 155318 (2011).

(iv) J. Debus, and D. Dunker. *Raman studies on a heavily distorted polycarbonate sample - Raman Untersuchungen an einer stark deformierten Polycarbonat-Probe.* Condensed Matter - Materials Science, arXiv: 1203.0064 (2012).

(v) D. Dunker, T. S. Shamirzaev, J. Debus, D. R. Yakovlev, K. S. Zhuravlev, and M. Bayer. *Spin relaxation of negatively charged excitons in (In,Al)As/AlAs quantum dots with indirect band gap and type-I band alignment.* Appl. Phys. Lett. **101**, 142108 (2012).

(vi) J. Cullen, K. Johnston, E. McGlynn, M. O. Henry, D. Dunker, D. R. Yakovlev, and M. Bayer. *Uniaxial stress and Zeeman spectroscopy of the 3.324-eV Ge-related photoluminescence in ZnO.* Phys. Rev. B **87**, 165202 (2013).

(vii) J. Debus, D. Dunker, V. F. Sapega, D. R. Yakovlev, G. Karczewski, T. Wojtowicz, J. Kossut, and M. Bayer. *Spin-flip Raman scattering of the neutral and charged excitons confined in a CdTe/(Cd,Mg)Te quantum well.* Phys. Rev. B **87**, 205316 (2013).

(viii) F. Liu, L. Biadala, A. V. Rodina, D. R. Yakovlev, D. Dunker, C. Javaux, J. -P. Hermier, Al. L. Efros, B. Dubertret, and M. Bayer. *Spin dynamics of negatively charged excitons in CdSe/CdS colloidal nanocrystals.* Phys. Rev. B **88**, 035302 (2013).

(ix) J. Debus, A. A. Maksimov, D. Dunker, D. R. Yakovlev, E. V. Filatov, I. I. Tartakovskii, V. Yu. Ivanov, A. Waag, and M. Bayer. *Heating of the Mn spin system by photoexcited holes in type-II (Zn,Mn)Se/(Be,Mn)Te quantum wells.* Submitted to Phys. Rev. B.

(x) J. Cullen, K. Johnston, D. Dunker, E. McGlynn, D. Yakovlev, M. Bayer, and M. O. Henry. *The Hg isoelectronic defect in ZnO.* In preparation to submission to Phys. Rev. B.

(xi) J. Debus, T. S. Shamirzaev, D. Dunker, V. F. Sapega, E. L. Ivchenko, D. R. Yakovlev, K. S. Zhuravlev, and M. Bayer. *Fine structure of* $\Gamma - X$ *mixed exciton in indirect band-gap (In,Al)As/AlAs quantum dots determined by spin-flip Raman scattering.* In preparation to submission to Phys. Rev. B.

(xii) J. Debus, D. Dunker, V. F. Sapega, D. R. Yakovlev, D. Reuter, A. D. Wieck, and M. Bayer. *Optical resonance-excitation involved in the Raman-scattering induced electron spin-flip in singly charged (In,Ga)As/GaAs quantum dots* . In preparation to submission to Phys. Rev. B.

(xiii) T. S. Shamirzaev, D. Dunker, D. S. Abramkin, J. Debus D. R. Yakovlev, K. S. Zhuravlev, and M. Bayer. *Spin relaxation of bright and dark exciton in (In,Al)As/AlAs QDs.* In preparation.

(xiv) J. Debus, D. Dunker, V. L. Korenev, I. A. Akimov, A. Schwan, D. R. Yakovlev, and M. Bayer. *Polarization-dependent magneto-photoluminecence of negatively charged nitrogen-vacancy centers in diamond.* In preparation.

(xv) J. Debus, D. Dunker, V. F. Sapega, D. R. Yakovlev, D. Reuter, A. D. Wieck, and M. Bayer. *Otical resonance-excitation involved in the Raman-scattering induced electron spin-flip in singly charged (In,Ga)As/GaAs quantum dots.* In preparation.

Symbols and Abbreviations

A	Fitting parameter
α	PL decay parameter
a_{B}	Bohr radius
a_i, b_i	Quantum dot dimensions
Al	Aluminum
A_n or A_j	Hyperfine constant
AOM	Acousto-optical modulator
As	Arsenid
a_1, a_2, a_3	Reciprocal lattice vectors
$\mathbf{B}$	Magnetic field vector
B_{eff}	Effective magnetic field
B_{N}	Nuclear magnetic field
B_{NF}	Nuclear fluctuation field
CB	Conduction band
CCD	Charge-coupled device
Cd	Cadmium
$c_j^\dagger$, c_j	Electron generator and annihilator operators
d	Thickness of the intermixed layer surrounding the QD
D	Direct transition (chapter 1.3), QD Diameter
D_{AV}	Average QD diameter
$D(E)$	Density of states
δ_0	Bright-dark exciton splitting energy
δ_1	Bright-exciton spin state splitting
δ_2	Dark-exciton spin state splitting
ΔE	Energy difference
DFG	Digital function generator
Δg	Deviation from the free electron g-factor
D_S, D_L	Smaller and larger half-width values of the QD size distribution
Δ_{SO}	Splitting of the valence band ground state
$\overline{\Delta}$	Average value of $\Delta E_{\Gamma-X}$
$\tilde{\Delta}$	Variation value for $\Delta E_{\Gamma-X}$

e	Elementary charge
ϵ	Permittivity
E	Energy
$\tilde{E}$	Energy eigenvalue
η	Dimensionless electron density in proximity of nuclei
E_{ab}	Absorption energy
E_{Bo}	Bohr energy
E_{B}	Binding energy of the exciton complex
E_{em}	Emission energy
E_{F}	Fermi energy
E_{G}	Band gap energy
$E_j(\vec{k})$	Valence or conduction band dispersion
E_{SR}	Short-range interaction splitting
E_{X}	Energy dispersion of the exciton states
E_1,E_2	Orbital energies
f	Focal length
fcc	Face cubic centered
F_k	Envelope wave function
FM	Frank-van der Merwe
f_{Rep}	Repetition frequency
FWHM	Full width at half maximum
g	Landé g-factor
g	Grating
Ga	Gallium
Ge	Germanium
$G(\tau)$	Exciton lifetime distribution function
γ_1, γ_2	Surface energy from material 1 and 2
Γ	Center of the first Brillouin zone
$\gamma_{1,2}$	Heterointerface surface energy
h	QD height
$\hbar$	Reduced Planck constant
$\hat{H}$	Hamiltonian
$\hat{H}_{\mathrm{exch}}$	Exchange interaction matrix
hh	Heavy hole
$hatH_{SO}$	Effective Hamiltonian
$\hat{H}_Z$	Zeeman Hamiltonian
$\hat{H}_{\mathrm{ZN}}$	Zeeman Hamiltonian for nuclei
I^-,I^+	Circular-polarized PL intensities
ID	Indirect transition
$\mathbf{I}_n$	Single nuclear spin

In	Indium
InSb	Indiumantimonide
I_{sc}	Intensity of the SFRS signal
I_0	Intensity of the optical excitation
$\mathbf{I}_{\mathrm{n}}$	n-th nucleus spin operator
j_i	Heavy-hole spin operator
J_z	Angular momentum projection
$\vec{k}$	Wave vector
K	Kelvin
$k^{\parallel}$	Wave vector parallel to the quantum well
κ_{KL}, q_{KL}	Kohn-Luttinger parameters
L	Symmetry point at a edge of the Brillouin zone
L_i	Structure size along kartesian axis i
lh	Light hole
LO	Longitudinal optic
λ	Wavelength
Λ	Radio frequency wavelength
M	Angular momentum projection
MBE	Molecular beam epitaxy
Mg	Magnesium
m^*	Electron effective mass
m_{R}	Reduced mass of the electron-hole pair
ms	Millisecond
mT	Millitesla
m_v, m_c	Effective masses of the valence and conduction band
μ	Exciton effective mass
μ_{B}	Bohr magneton
μ_j	Nuclear magnetic moment
μ_n	Nuclear magneton
μeV	Microsecond
μs	Microsecond
μT	Microtesla
N	numerical aperture (in chapter 2), Atomic nucleus
n	Orbital numbers
$1N_{\mathrm{D}}$	Volume QD density
Nd:YVO_4	Neodym-doped yttriumorthovanadate
n_{h}	Hole density
n_y, n_z, n_x	Quantization number
∇	Nabla-operator

$N^{\uparrow,\downarrow}$	Spin state occupation
ω	Frequency
Ω	Frequency difference ranging from zero at the Γ-state to unity at the X-state
$\Omega(k)$	Spin precession or Lamor frequency
$\Omega_{,\mathrm{LO}}$	Frequency of LO phonon
P	Power density
PMT	Photomultiplier tube
PL	Photoluminescence
Ψ	Wave function
QD	Quantum dot
QW	Quantum well
$\vec{r}_1$, $\vec{r}_2$	Position of the electron and hole
$\vec{R}$	Relative coordinate for the center of mass
rms	Root mean square
R_{Ryd}	Rydberg energy
ρ_c	Circular polarization degree
ρ_c^o	Optically induced spin polarization
$\rho_{\mathrm{c},B}$	Magnetic-field induced circular polarization degree
$\rho_{\mathrm{c,o}}$	Optical orientation degree
s	Spin
S_D	Size dispersion
SFRS	Spin-flip Raman scattering
Si	Silicon
s_i	Electron spin operator
σ	Pauli matrix
SK	Stranki-Krastanov
S_z	Average spin along z-axis
T	Temperature
T	Tesla
T_{an}	Annealing temperature
τ_c	Correlation time
Te	Tellurid
TEM	Transmission electron microscopy
T_g	Temperature of the substrate during the growth process
t_{gi}	Interuption time
T_{He}	Liquid helium temperature
τ_p	Average time between two momentum scattering processes
τ_s	Spin relaxation time
τ_0	Exciton lifetime distribution maximum

T_{Rep}	Repetition periode
T^{-}	Trion complex
u_0	Unit cell normalized Bloch function
VB	Valence band
V	Potential
$\langle v_k \rangle$	Average electron velocity
VTI	Variable temperature inset
VW	Volmer-Weber
V_0	Unit cell volume
V_L	Localization volume
W_{ab}	Probabilities of absorbtion
W_{em}	Probabilities of emission
W_{sf}	Probabilities of spin-flip
X	Symmetry point at the edge of the Brillouin zone
X	Exciton
x_j	Fraction of alloy substitution

List of Figures

List of Tables

Acknowledgements

First of all, I would like to thank everyone, who accompanied me in the last couple of years and supported me in the scientific work.
I would like to thank Prof. Dr. Manfred Bayer, who enabled me to work at one of the best equipped educational chair possible and who further to that provided a never-ending support of ideas and humor. My thanks go further to Prof. Dr. Dmitri R. Yakovlev for his invaluable help, education, and for enabling to work in a friendly and still productive atmosphere. Prof. Dr. Dietmar Fröhlich, I thank especially for the many discussions about the very fundamental properties of my research and for the many insights he is always willing to give.
I am thankful to Prof. Dr. Timur S. Shamirzaev for providing both ideas and samples for our collaborative work and for the fruitful discussions that followed each of his visits. Prof. Dr. Victor F. Sapega for the very nice collaboration and explanations making even the most complex processes easy to understand. I am grateful to Dr. Jörg Debus, with whom I spent so much time in the laboratory and office in the last years. We have been working like a machine, but could still laugh at the end of each day; for that I am very grateful.
Dr. Ilya A. Akimov, Dr. Alex Greilich and Prof. Dr. Evgeny Zhukov I thank for all their aid and advice they have provided over the years. I further appreciate the theoretical work from Prof. Dr. Eougenious L. Ivchenko and Prof. Dr. Volodya L. Korenev and thank for all the explanations given.
Klaus Wiegers and Michaela Wäscher I owe my deepest gratitude for being the good faith in our department and for helping on the one hand keeping the laboratory in one piece and on the other for helping to find the way in the administrative labyrinth. Lars Wieschollek and Thomas Stöhr, I thank for solving so many technical problems and being congenial colleagues. Many thanks to Fabian Heisterkamp and Liu Biadala for their proofreading.
Dennis Kudlacik and Dion Braukmann, I am grateful for their help in the laboratory and for the nice talks in the office. Dr. Feng Liu and Dr. Hannes Kurtze, I would like to thank for comfortable atmosphere in the office and the interesting discussions.
To all the E2-members present or past who have not been mentioned so far, I owe apologies, as everyone deserves to be mentioned by name. The time spent at E2 has been a very nice one for me and I thank every one of you, as all of you have been responsible for that.
My deepest gratitude goes to my lovely girlfriend Claudia, who supported me,

when I needed help and even stronger pushed me, when I needed that too.
Finally, I would like to thank my parents Bärbel and Klaus, my sister Stefanie, and my brother Jan-Hendrik for their support and just for being the wonderful family they have been over all those years.